Cross-Sectional Stability of Double Inlet Systems

Cross-Sectional Stability of Double Inlet Systems

Proefschrift

ter verkrijging van de graad van doctor
aan de Technische Universiteit Delft,
op gezag van de Rector Magnificus prof.ir. K.C.A.M. Luyben,
voorzitter van het College voor Promoties,
in het openbaar te verdedigen op maandag 30 september 2013 om 12:30 uur
Delft, Nederland

door

Ronald Leendert Brouwer
civiel ingenieur
geboren te Hellevoetsluis, Nederland

Dit manuscript is goedgekeurd door de promotor:
Prof.dr.dr.h.c.ir. M.J.F. Stive

Copromotor:
Dr. H.M. Schuttelaars

Samenstelling promotiecommissie:

Rector Magnificus	voorzitter
Prof.dr.dr.h.c.ir. M.J.F. Stive	Delft University of Technology, promotor
Dr. H.M. Schuttelaars	Delft University of Technology, copromotor
Prof.dr.ir. J. van de Kreeke	University of Miami
Prof.dr.ir. Z.B. Wang	Delft University of Technology
Prof.dr.ir. W.S.J. Uijttewaal	Delft University of Technology
Prof.dr. L.R.M. Maas	NIOZ/Utrecht University
Dr.ir. P.C. Roos	University of Twente

This research has been financially supported by Delft University of Technology and the Delft Cluster Project: Sustainable development of the North Sea and Coast.

Keywords: barrier coast, tidal inlet system, cross-sectional stability, equilibrium, morphodynamics, entrance/exit losses.

ISBN 978-94-6186-178-8

Printed by GVO drukkers & vormgevers B.V., the Netherlands.

Cover image: Author's impression of the Dutch, German and Danish Wadden Sea coast

Advice from the ocean:

Be shore of yourself
Come out of your shell
Take time to coast
Avoid pier pressure
Sea life's beauty
Don't get tide down
Make waves!

- Ilan Shamir

Summary

Barrier coasts and their associated tidal inlet systems are a common feature in many parts of the world. They constitute dynamic environments that are in a continuous stage of adapting to the prevailing tide and wave conditions. Commonly, these coastal areas are densely populated and (partly) as a result there often exists a strong conflict of interests between issues related to coastal safety, economic activities and ecology. To manage these different interests, it is important to gain more understanding of the long-term morphological evolution of tidal inlet systems and their adaptation to natural changes and human intervention. In this thesis the focus is on double inlet systems, where two tidal inlets connect a back-barrier basin to an ocean or a coastal sea.

To investigate the morphological evolution of double inlet systems and their adaptation to internal or external change, the equilibrium configuration and stability properties of the cross-sectional areas of the two tidal inlets are studied in detail. To that extent, a widely used empirical relationship for cross-sectional inlet stability is combined with (i) a lumped-parameter (L-P) model (Chapters 2 and 3) and (ii) a two-dimensional, depth-averaged hydrodynamic (2DH) model for the water motion (Chapter 4). The Marsdiep-Vlie inlet system in the western Dutch Wadden Sea and the Faro-Armona inlet system in the Portuguese Ría Formosa serve as case studies throughout this thesis.

With the assumptions of a cross-sectionally averaged, uniform inlet flow velocity and a uniformly fluctuating basin surface elevation, model results of the L-P model show that stable equilibrium configurations where both inlets are open exist. It is necessary, however, to account for the important processes either explicitly, e.g. including a topographic high in the back-barrier basin as observed in the Wadden Sea (Chapter 2), or parametrically, e.g. allowing for inlet entrance/exit losses for relatively short inlets such as in the Ría Formosa (Chapter 3).

By solving the depth-averaged, linear shallow water equations on the f-plane with linearised bottom friction, the 2DH model explicitly accounts for spatial variations in surface elevation in the ocean, inlets and basin. Model results show that these spatial variations, induced by e.g. basin bottom friction, radiation damp-

ing, and Coriolis effects, are crucial to simulate and explain the long-term evolution of double inlet systems. This approach further allows the identification of a stabilising and destabilising mechanism associated with the persistence or closure of one (or both) of the inlets in a double inlet system and hence with its long-term evolution.

Samenvatting

Barrièrekusten en hun bijbehorende zeegat systemen zijn een veelvoorkomende kustvorm over de hele wereld. Het zijn dynamische omgevingen die zich continu aanpassen aan de heersende getij- en golfcondities. Deze kustgebieden zijn over het algemeen dichtbevolkt en (mede) daardoor ontstaan er vaak sterke conflicten tussen problemen die gerelateerd zijn aan kustveiligheid, economische activiteiten en ecologie. Om deze conflicten te beheersen is het van groot belang om meer kennis te vergaren over de morfologische, lange termijn ontwikkeling van deze systemen en hun reactie op natuurlijke veranderingen en menselijke ingrepen. In deze dissertatie ligt de focus op dubbel zeegat systemen, waarbij twee zeegaten het achterliggende bekken verbinden met een oceaan of kustzee.

Om de morfologische ontwikkeling van dubbel zeegat systemen en hun aanpassing aan interne en externe veranderingen te onderzoeken, worden in deze dissertatie de evenwichtsconfiguraties en stabiliteitskenmerken van de dwarsdoorsneden van de twee zeegaten gedetailleerd bestudeerd. Daarvoor wordt er een veelgebruikte empirische relatie voor de stabiliteit van de dwarsdoorsnede van een zeegat gecombineerd met (i) een 'lumped-parameter' (L-P) model (Hoofdstuk 2 en 3) en (ii) een twee-dimensionaal, diepte-gemiddeld hydrodynamisch (2DH) model voor de waterbeweging (Hoofdstuk 4). Het Marsdiep-Vlie systeem in de westelijke Nederlandse Waddenzee en het Faro-Armona systeem in de Portugese Ría Formosa worden gebruikt als casus.

Met de aanname van een dwarsdoorsnede-gemiddelde, uniforme stroomsnelheid door het zeegat en een uniform fluctuerend waterniveau in het bekken, laten resultaten van het L-P model zien dat stabiele evenwichtsconfiguraties, waarbij beide zeegaten open zijn, kunnen bestaan. Het is daarbij wel van belang om de belangrijke processes expliciet, bv. door het implementeren van een wantij in het bekken zoals geobserveerd wordt in de Waddenzee (Hoofdstuk 2), of impliciet, bv. door het toestaan van in- en uittreeverliezen voor korte zeegaten zoals in de Ría Formosa (Hoofdstuk 3), mee te nemen.

Door de diepte-gemiddelde, ondiep water vergelijkingen met lineaire bodemwrijving op te lossen, neemt het 2DH model ruimtelijke variaties van het waterniveau in de oceaan, zeegaten en bekken expliciet mee. Modelresultaten laten zien

dat deze ruimtelijke variaties, opgewekt door bv. bodemwrijving in het bekken, radiale demping in de oceaan en Coriolis effecten, cruciaal zijn om de ontwikkeling van dubbel zeegat systemen te simuleren en te verklaren. Deze modelbenadering staat bovendien de identificatie van een stabiliserend en destabiliserend mechanism toe, die gerelateerd zijn aan het open blijven of het sluiten van één van de (of beide) zeegaten in een dubbel zeegat systeem en dus met zijn morfologische ontwikkeling.

Acknowledgements

While writing these acknowledgements, a lot of thoughts fly around in my head. One of the main thoughts that keeps flying by is:"I can't believe this chapter has come to an end". I have been combining a (semi-)professional field hockey career and a scientific education for a long period and I've enjoyed every minute of it. During this period I've had the privilege to meet a number of amazing people and this thesis would not have been possible without their contribution. Therefore, I devote these acknowledgements to them.

First of all, I'd like to thank Marcel Stive for providing me with the opportunity to start a Ph.D. study and giving me the freedom to combine it with a successful (semi-)professional field hockey career. Your support, kindness, human interest and availability (even in hectic times) have made a big impact on me.

Embracing the opportunity to understand a problem even better when a result is totally not what you expect, is one of the insights my daily supervisor, Henk Schuttelaars, taught me. Henk, I cannot express my gratitude enough. Your sense of humour, ability to simplify even the most difficult problems, search for perfection and patience with my desire for discussion, made me enjoy every second of our cooperation during my Ph.D. study.

Next, I would like to thank Co van de Kreeke for passing on his interest in and passion for (multiple) tidal inlet systems. Together with Henk, you have guided me since the start of my M.Sc. thesis to where I am today. Thank you very much for introducing me to the scientific community and for your sharp and critical comments on every document I sent you. I will always remember our sailing trip out on Biscayne Bay.

In search for a relatively fast, two-dimensional model for the water motion in a double inlet system, Henk introduced me to Pieter Roos. In my opinion a perfect match. Our mutual fascination for fundamental science, spotting the tiniest and sometimes useless style errors, sports and of course LEGO has led to a good friendship and made our collaboration very fruitful. Working together with you and Henk really made me feel part of a team.

A special thanks goes out to Tjerk Zitman and Howard Southgate. Tjerk for

helping me out when I had modelling and Matlab issues, discussing model results and humorous meetings; and Howard for his curiosity, his interest and proofreading my thesis.

Furthermore, I want to thank my colleagues of the Section of Hydraulic Engineering, realising that the list is far from complete. My room-mates (in consecutive order): Tomo, thank you for your warm character, the Japanese classes, diner at your place and of course Nam-myoho-renge-kyo (I remembered); Vana, I really liked our discussions about non-scientific topics; and Marriëte, thank you for taking care of me during the last period of finalising my thesis. Martijn, Matthieu, Sierd, Chu, Meagan: somehow the road to my office always passed your office, no matter from which direction I was coming. Thanks for listening, discussions, lunch and making coming to the office enjoyable every single time. My Coastal Dynamics II examination buddies Menno and Sierd (and even earlier Jakob and Jasper): It was actually really nice to be able to broaden your knowledge in such a way. Marije: thanks for sharing your thoughts and listening to mine. Wim: the conversations about snowboard and mountain bike trips always made me wander off and forget about finishing my Ph.D. thesis. The support staff: Chantal, Agnes, Judith and Inge, thank you for all those years of helping me with all kinds of issues.

Besides colleagues at the university, a lot of people outside the university community have contributed in one way or the other. I want to thank my family, family-in-law, friends, my HC Bloemendaal team-mates and staff and other friends from the hockey community for their interest, support, layman's questions and fun times.

At the time of writing these acknowledgements, I know that during my defence I will be supported by Marc and Joris as my paranimphs. I'm already looking forward to it.

And last, but certainly not least: Birgit, Kalle, Ronja and Lotta. Where would I be without you?

Ronald Brouwer

Hamilton, New Zealand
August 2013

Contents

1 Introduction

Double inlet systems, often found along barrier coasts, are coastal systems in which two tidal inlets connect a single back-barrier basin to an ocean or a coastal sea. In this thesis the cross-sectional equilibrium configurations of the tidal inlets and their stability properties are investigated, in order to obtain more insight into the long-term evolution of double inlet systems.

In Section 1.1 a description of barrier coasts and tidal inlet systems is given. With this general background information in mind, the focus of this thesis is motivated in Section 1.2. Subsequently, in Section 1.3 the Faro-Armona and Marsdiep-Vlie inlet systems are introduced. These systems are used throughout this thesis as typical examples of a double inlet system where the two inlets are directly connected by a channel in the basin and one in which this connection is hindered, but not entirely obstructed, by the presence of a topographic high[1] (also known as tidal watershed or tidal divide). A detailed description of the present-day knowledge of cross-sectional stability of tidal inlets is given in Section 1.4. Based on this information, in Section 1.5 the research questions are formulated. Finally, in Section 1.6 the methodology and approach that are used in this thesis are addressed.

1.1 Barrier coasts and tidal inlet systems

Nowadays, approximately ten percent of the world's continental coastline consists of barrier coasts (Glaeser, 1978). These coasts are a concatenation of tidal

[1] a topographic high is formed where the tidal waves travelling through two adjacent inlets meet and sedimentation due to low velocities results in tidal flat formation. They act as semi-permeable barriers that allow a certain degree of water exchange.

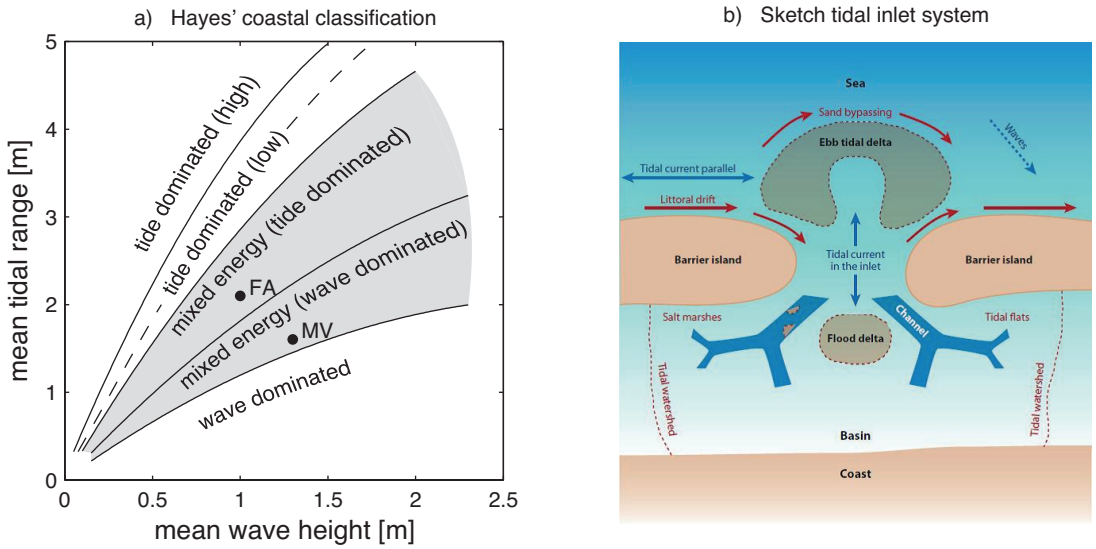

Figure 1.1: (a) Relationship between tidal range, wave height and coastal morphology modified from Hayes (1975, 1979). The black dotted curve represents the approximate limit of barrier islands formation. The dots desginated FA and MV indicate the position of the Faro-Armona and Marsdiep-Vlie double inlet systems in this coastal classification (see text Section 1.3) and (b) Sketch of a single tidal inlet system, showing the different geomorphologic elements and the dominant physical processes and phenomena. From: de Swart & Zimmerman (2009).

inlet systems, in which a tidal basin or back-barrier area is connected to an ocean or a coastal sea by one or more tidal inlets. Many of the barrier coasts found around the world formed during the Holocene[2] when continental shelves were flooded owing to sea level rise (e.g. Beets & van der Spek, 2000).

Apart from the geological setting, barrier coasts and the associated tidal inlet systems are primarily shaped under the influence of tides and waves. Astronomical tides induce both variations in water elevation and currents, with tidal currents in the inlet in the order of 1 m s^{-1}. Wind-induced surface waves break in shallow areas inducing wave-driven currents of approximately 1 m s^{-1}. Finally, riverine outflow (when present) will also affect the current in the inlet.

Since waves and tides are important, barrier coasts have been classified using wave height and tidal range. Hayes (1975, 1979) extended the classification introduced by Davies (1964) from three to five categories ranging from tide-dominated to wave-dominated coasts; see Fig. 1.1a. Later, Davis Jr. & Hayes (1984) emphasised that it is the *relative* effect of tides and waves that determines the coastal morphotype, not the absolute values of the two. Other factors that

[2]the Holocene is the present interglacial period, starting at approximately 10,000 years B.P.

need to be taken into consideration when dealing with tidal inlets are: coastal physiography, tidal prism, availability of sediment and influence of riverine input. Consequently, barrier coasts that belong to a certain category based on wave height and tidal range alone can display coastal features of another category because of the influence of the aforementioned factors. In this thesis, mixed-energy coasts are considered where the coastal morphotype displays tide-dominated characteristics, such as short, drumstick-shaped barriers with well-developed ebb deltas (see grey area in Fig. 1.1a).

Now focussing on tidal inlet systems in sandy environments, several morphological elements can be discerned; see Fig. 1.1b. On the seaward side of the inlet a shallow ebb-tidal delta is often found that usually folds around a deep channel. On the landward side of the inlet sometimes a flood delta is observed. Inside the basin, the main channels become shallower when moving away from the inlet. Typically, they undergo a sequence of bifurcations resulting in a complex pattern of channels and tidal flats. Salt marshes are commonly found near the coastlines of the mainland and the barrier islands (de Swart & Zimmerman, 2009).

Conceptually, waves and tides can also explain the morphodynamics of tidal inlet systems (see Fig. 1.1b). Obliquely incident waves generate alongshore currents thus triggering alongshore transport of sediment, the so-called *littoral drift*. When this sediment reaches the downdrift side of a barrier island adjacent to an inlet, part of it is transported past the inlet to the updrift part of the next barrier island by bar bypassing. This process moves sediment along the seaward portion of the ebb-tidal delta towards the downdrift shore. Another part is transported past the inlet by tidal flow bypassing, in which the sediment enters the inlet on flood tide, deposits there and is exported seaward on the ebb tide to the downdrift side of the inlet (see Bruun et al., 1978). A fraction of the littoral drift that is not bypassed to the next island can also be imported into the basin by various mechanisms, such as tidal asymmetry (Pingree & Griffiths, 1979; Friedrichs & Aubrey, 1988), spatial and temporal settling lag and scour lag effects (Postma, 1954; van Straaten & Kuenen, 1957; Groen, 1967; Dronkers, 1986) and topographic effects (e.g. Friedrichs et al., 1998; Pritchard & Hogg, 2003).

In this thesis the focus is on *double inlet systems*, i.e. a part of a barrier coast where two tidal inlets connect a single back-barrier basin to the ocean or a coastal sea. Examples include the Marsdiep-Vlie system as part of the Dutch Wadden Sea coast (Ehlers, 1988), the Faro-Armona system located in the Ría Formosa lagoon in southern Portugal (Salles et al., 2005), the Pass Cavallo-Matagorda Inlet system on the Gulf coast of the United States (van de Kreeke, 1985; Davis Jr., 1997) and the Katikati-Tauranga system on New Zealand's North Island (Heath, 1976; Hicks et al., 1999).

1.2 Focus of this study

Tidal inlet systems are important areas from a point of view of coastal zone management. They are morphologically very active, i.e. they are in a continuous stage of adapting to the prevailing tide and wave conditions. There often exists a strong conflict of interests between issues related to coastal safety, economic activities and ecology. Coastal safety is of paramount importance for coastal areas that are often densely populated. The safety of these areas, and their inhabitants, may be endangered by natural changes (e.g. sea level rise, storm-induced barrier island breaching), but also by human interventions (e.g. inlet relocation, basin reduction, gas mining). Economic activities related to these systems include navigation, fisheries, tourism and mining of natural resources. From an ecological point of view, shallow tidal basins are among the richest food supplying marine ecosystems, supporting a rich flora and fauna. These shallow tidal areas provide important nursery grounds for marine animals during their juvenile stages (Oost & de Boer, 1994).

To manage these systems in an optimal way, it is important to gain more understanding of the long-term evolution and stability properties of tidal inlet systems, which can be inferred from the evolution of the cross-sectional area of the tidal inlets. Up to now, most studies (e.g. Escoffier, 1940) investigating the cross-sectional stability of tidal inlets focused on *single inlet systems*: a single tidal inlet channel that connects a single back-barrier basin to the ocean. However, many tidal inlet systems consist of two (or more) tidal inlets connecting ocean and basin. Even though some studies exist that investigate the stability of double inlet systems (e.g. van de Kreeke, 1985, 1990a,b), their long-term existence has not been studied in a systematic way. Moreover, observations suggest that the results of these studies may only be valid for specific situations and are, thus, not generic. Therefore, the general aim of this thesis is formulated as:

> *To obtain fundamental knowledge of the cross-sectional stability of tidal inlets in double inlet systems, identifying stabilising and destabilising mechanisms.*

1.3 Study sites

Throughout this study two examples of double inlet systems will be used: the Marsdiep-Vlie inlet system in the western Dutch Wadden Sea and the Faro-Armona inlet system in southern Portugal. The first one is an example of a double inlet system where water exchange between two inlets through the basin is limited by the presence of a topographic high. The latter is an example where water in the basin can freely flow from one inlet to the other. The reason to discuss both is that due to these different characteristics, different physical processes may dominate

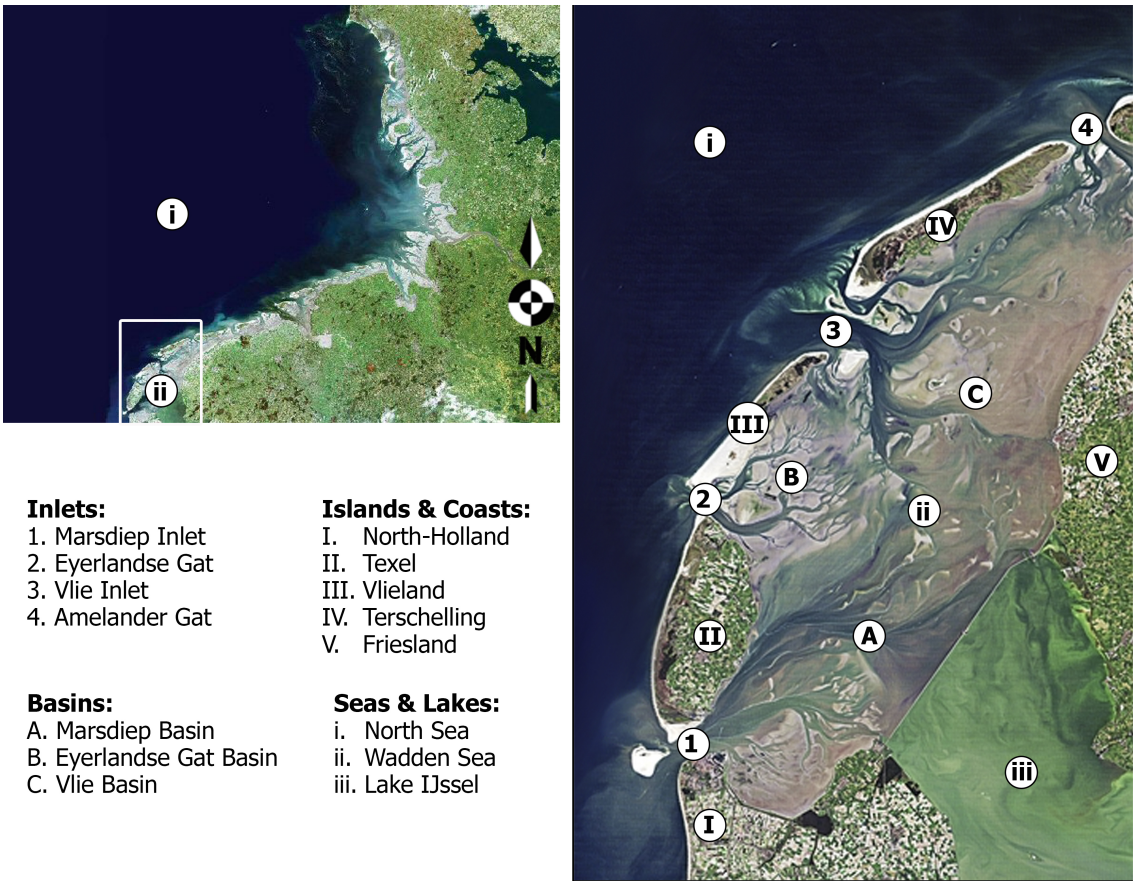

Inlets:
1. Marsdiep Inlet
2. Eyerlandse Gat
3. Vlie Inlet
4. Amelander Gat

Islands & Coasts:
I. North-Holland
II. Texel
III. Vlieland
IV. Terschelling
V. Friesland

Basins:
A. Marsdiep Basin
B. Eyerlandse Gat Basin
C. Vlie Basin

Seas & Lakes:
i. North Sea
ii. Wadden Sea
iii. Lake IJssel

Figure 1.2: Left: Satellite photo of the Dutch, German and Danish Wadden Sea coast (Copyright: Common Wadden Sea Secretariat). Right: the western Dutch Wadden Sea coast and associated tidal inlet systems (Copyright: USGS/ESA).

their stability.

1.3.1 Marsdiep - Vlie inlet system, the Netherlands

The Marsdiep-Vlie system is located in the western part of the Dutch Wadden Sea (left panel Fig. 1.2). This part of the Dutch Wadden Sea is drained by the tidal inlets Marsdiep, Eyerlandse Gat and Vlie (right panel Fig. 1.2). A reconstruction since the Holocene (Vos et al., 2011) indicates that this system established around 1500 AD and adapted to natural and/or man-made changes (see also Beets & van der Spek, 2000; Oost & de Boer, 1994). In the north-east a typical topographic high separates the back-barrier basin from the tidal basin of the Amelander Gat Inlet. To the east the coast of Friesland forms a natural boundary. In 1932 the Zuiderzee (now called Lake IJssel) was separated from the Wadden Sea by a long barrier (see e.g. Elias et al., 2003, for a re-analysis of this human intervention on the tidal inlet dynamics). The basin drained by the Eyerlandse Gat Inlet is small

and is separated from the Marsdiep and Vlie basins by a very long and shallow tidal watershed. It can be considered as an independent inlet system, which hardly influences the water motion in the Marsdiep-Vlie system (Zimmerman, 1976). The spacing of the Marsdiep and Vlie Inlets is approximately 30 km. The horizontal area of their basins with respect to mean sea level (MSL) is approximately 7.55×10^8 m^2 and 6.25×10^8 m^2, respectively (see e.g. Maas, 1997).

Along the Dutch Wadden Sea coast the tide is dominated by the semi-diurnal lunar constituent (M2)[3]. The tidal wave travels from west to east, arriving first at the Marsdiep Inlet with a mean tidal range off the inlet of approximately 1.4 m and arrives approximately 30-40 minutes later at the Vlie inlet with a mean tidal range of approximately 1.8 m. During spring and neap tide, the tidal ranges at the Marsdiep Inlet are 2.0 m and 1.0 m, respectively (Elias et al., 2003), and at the Vlie Inlet are 2.8 m and 1.2 m, respectively (Grunnet & Hoekstra, 2004). Ferry measurements at the Marsdiep Inlet show maximum ebb and flood tidal velocities ranging between 2.0 and 1.0 m s^{-1} for spring and neap tide, respectively (Buijsman & Ridderinkhof, 2007). At the Vlie inlet similar tidal currents are expected (Ridderinkhof, 1988). The mean offshore significant wave height is approximately 1.3 m from the west-southwest, with a corresponding mean wave period of 5 s (e.g. Roskam, 1988; Wijnberg, 1995). During storms, wind-generated waves can be higher than 6 m and water level surges of more than 2 m have been measured. Wave induced longshore sediment transport rates vary from 0.5-0.6 Mm^3 year^{-1} (Tànczos et al., 2001) to 1 Mm^3 year^{-1} (Spanhoff et al., 1997) and have an eastward direction. Following the classification of Hayes (1979), the Marsdiep-Vlie system qualifies as a mixed-energy coast that is wave-dominated; denoted by MV in Fig. 1.1a. However, the morphology of the inlets show tide-dominated characteristics such as large ebb-tidal deltas. This is caused by the large tidal prisms and the relatively low wave energy (Davis Jr. & Hayes, 1984; Sha, 1989; Elias, 2006).

The sediment found along the North Sea coasts consists of fine to medium sand (usually greater than 200 μm) and is somewhat coarser than observed in the Wadden Sea (170-190 μm). The grain size distribution decreases towards the mainland, where median grain sizes vary around 120 μm. Of the sediment that settles within the Wadden Sea, some 70 to 80% consists of sand while the remainder is silt and clay (Oost, 1995).

1.3.2 Faro-Armona inlet system, Portugal

The Faro-Armona inlet system is a sub-system of the Ría Formosa: a lagoon in the southern part of Portugal separated from the Atlantic Ocean by a multiple-

[3]accurate tidal data can be acquired through the Rijkswaterstaat website: `http://www.rijkswaterstaat.nl`

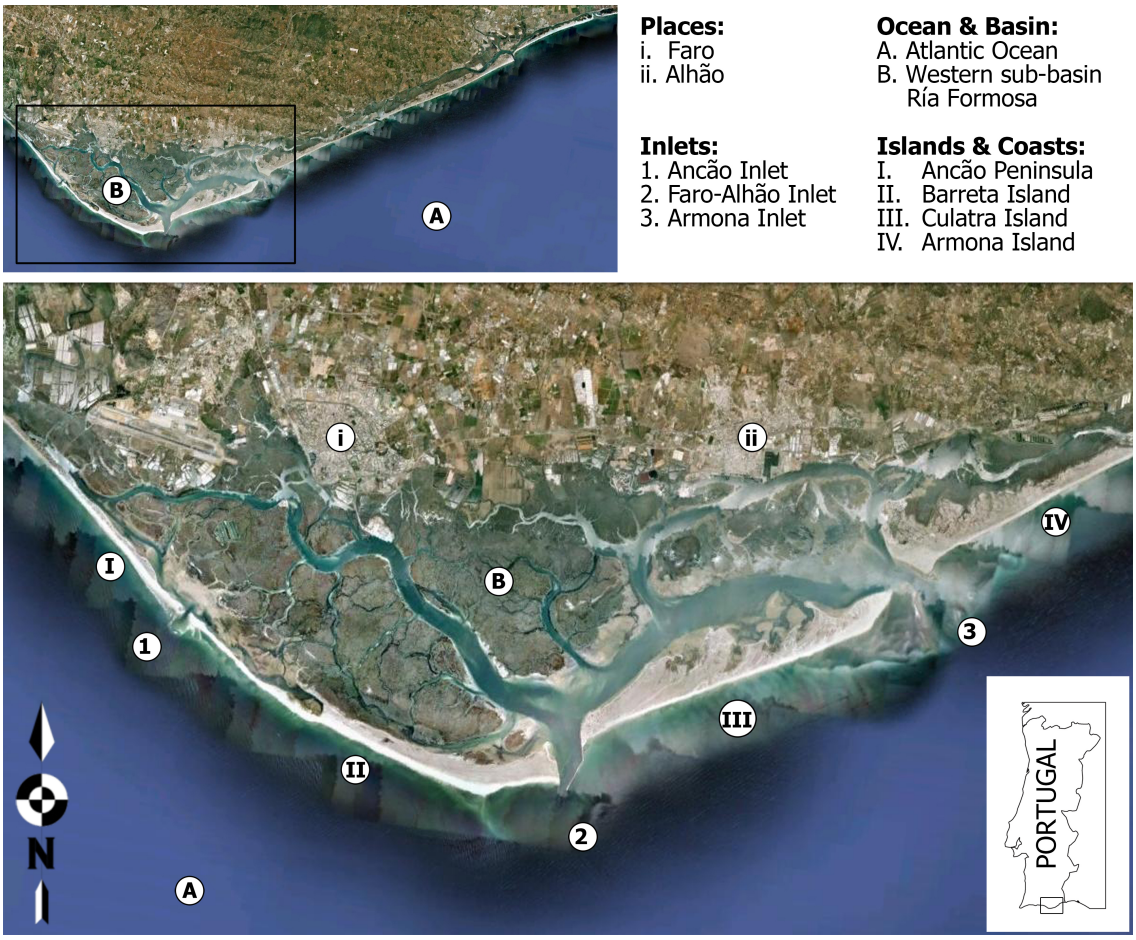

Figure 1.3: Top: The Ría Formosa on the southern coast of Portugal. Bottom: Western sub-basin of the Ría Formosa. Source: Google Earth

inlet barrier island system, see top panel Fig. 1.3. Analysis of the area's evolution since the 14th century shows that, although the system has responded to natural and artificial disturbances, it has always maintained between four to seven inlets (Salles, 2001). The western sub-basin consists of the Armona, Faro and Ancão Inlets, and covers approximately 3.4×10^7 m^2 (bottom panel Fig. 1.3). As a first approximation, the Faro and Armona Inlets can be treated as a double inlet system, since they capture 90% of the tidal prism of the western subsystem. Furthermore, there exists a relatively long winding connection between the Faro/Armona Inlets and Ancão Inlet suggesting that Faro/Armona are little influenced by Ancão Inlet (Salles et al., 2005, and references therein).

The tide in Ría Formosa is predominantly semi-diurnal. The mean tidal range is approximately 2.1 m and the spring and neap tidal ranges are 3.1 and 1.3 m, respectively (the equinoctial spring tides can reach up to 3.8 m) (Salles et al., 2005, and references therein). Differences between tidal amplitudes and phases off the

Faro and Armona Inlets can range from 0.01-0.1 m and 0-4 degrees (Dias et al., 2009). Maximum tidal currents measured in the Faro and Armona Inlets are in the order of 1 m s^{-1} (Salles et al., 2005). The wind is on average moderate (3 m s^{-1}) and predominantly from the west (Andrade, 1990). Salles et al. (2005) performed a variance analysis of the tidal and non-tidal signals, which showed that the meteorological and long-term water level variability explained less than 1% of the total recorded variance. The authors concluded, that the influence of wind on water circulation in the area is minimal. The wave climate in the area is moderate to high, with offshore annual wave heights and periods of 1 m and 8.2 s, respectively. The waves predominantly approach from the southwest, which results in an alongshore sediment transport from west to east with net values ranging from approximately 0.6×10^5 to 3.0×10^5 m^3 yr^{-1} (Vila-Concejo et al., 2006, and references therein). From the oceanographic data above it follows that according to the coastal classification of Hayes (1979) the Faro-Armona system qualifies as a mixed-energy coast that is dominated by tides; denoted by FA in Fig 1.1a.

The sediment near the inlets mainly consist of coarse sand (0.5-1 mm) (Pacheco et al., 2011b) and the salt marshes at the end of the basin are composed of silt (3.9-62.5 μm) and fine sand (125-250 μm) (Bettencourt, 1988).

From this description, it is clear that the Faro-Armona system is considerably smaller than the Marsdiep-Vlie system.

1.4 Cross-sectional stability of tidal inlets

To study the morphodynamic equilibrium of tidal inlets and their stability properties, empirical relationships and various types of models have been used (see e.g. de Vriend, 1996; de Vriend & Ribberink, 1996; Murray, 2003).

Empirical relationships describe the relation between different state variables for inlets in equilibrium. These relationships are derived from field data. They only describe macro-scale properties of the inlets. LeConte (1905) and later O'Brien (1931) proposed a relationship between the cross-sectional area of the tidal channel and the tidal prism[4] for inlets in equilibrium (AP-relationship) located along the sandy part of the Pacific coast of the United States. In its general form the AP-relationship reads

$$A = CP^q, \tag{1.1}$$

where A is the cross-sectional area of the inlet channel below MSL (m^2), P is the representative tidal prism (m^3) and C and q are empirical proportionality coef-

[4]the tidal prism is the volume of water flowing into the tidal inlet during flood and leaving the inlet during ebb, not accounting for freshwater discharge.

ficients. A and P are considered annually averaged values. Eysink (1990) illustrated the approximate empirical validity of this relation for the Dutch Wadden Sea; values of $q = 1$ and $C = 7.0 \cdot 10^{-5}$ m^{-1} were suggested. Several investigators evaluated these coefficients for other sandy coasts around the world (e.g. Bruun & Gerritsen, 1960; O'Brien, 1969; Jarrett, 1976; Hume & Herdendorf, 1988). The AP-relationship was originally purely empirical, however recently this relationship was given a physical footing (e.g. van de Kreeke, 1998, 2004; Kraus, 1998; Suprijo & Mano, 2004). Among other things, these studies suggest that in Eq. (1.1) $q \simeq 1$ and that the value of C decreases with increasing values of littoral drift.

To evaluate the cross-sectional stability of tidal inlets, two types of models are used: (1) *process-based morphodynamic models* and (2) *empirical morphodynamic models*. The first type of models are designed to reproduce the behaviour of a natural system as accurately as possible. They describe the morphologic evolution of a system based on first physical principles, i.e. they calculate bed level changes through a set of mathematical equations describing waves, currents and sediment transport. Examples are Wang et al. (1991, 1995) who used a two-dimensional, depth-averaged (2DH) morphodynamic model to study the long-term evolution of the tidal inlet channels and, consequently, the back-barrier basin of the Frisian Inlet after closure of the Lauwers Sea; Cayocca (2001) who used a two-dimensional horizontal morphodynamic model to study several stages of the evolution of the Arcachon Inlet in France; and Salles et al. (2005) who studied the contribution of non-linear mechanisms to the persistence of a multiple tidal inlet system in the Ría Formosa using a two-dimensional vertically averaged finite element model. The conclusion of the latter study is that the natural stable state of this system comprises three inlets. The authors attribute the possibility of a stable equilibrium configuration, with more than two inlets open, to the complex flow field in the basin that is produced by the interaction of tidal flow and topography. However, a clear elucidation as to which physical mechanisms are responsible for this stable configuration is not given. This might have something to do with some of the drawbacks of process-based models (see e.g. Hibma et al., 2003). One of them is that due to their complexity it is difficult to determine cause and effect. Other drawbacks are that they are not reliable to make morphodynamic predictions for time scales longer than decades and they are computationally expensive. Although progress has been made (e.g. Tung et al., 2012), at this stage process-based models are not developed sufficiently to study the cross-sectional stability of double inlet systems.

The second type of models combine field data, empirical equilibrium-state relationships, and large-scale balance equations. Wherever needed, parametrised results of more detailed simulation models are included. Since much of the information included in the semi-empirical models is not available at a very detailed scale, these models tend to describe the important physical processes of large-

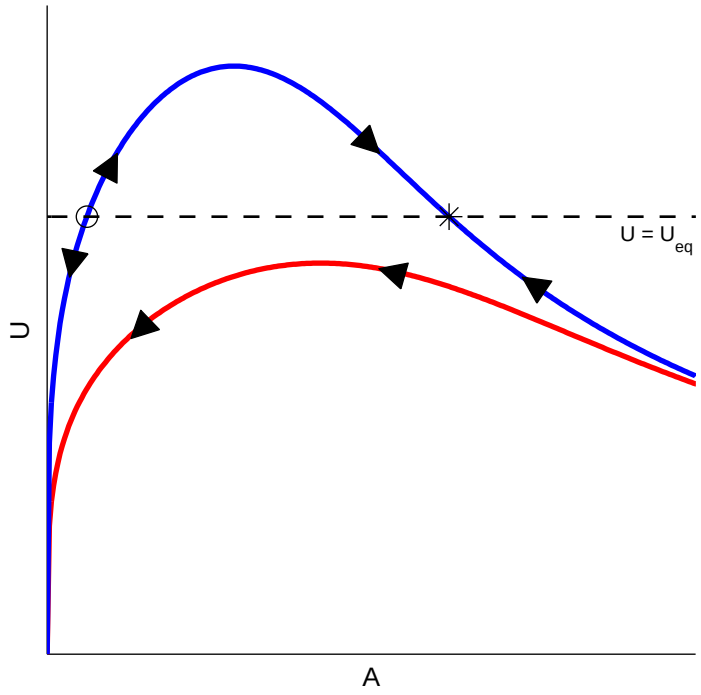

Figure 1.4: Schematisation of Escoffier's stability concept, where the amplitude of the tidal current U is plotted against the cross-sectional area of the inlet A for two arbitrary cases (blue and red line). The black dashed line represents the constant equilibrium velocity U_{eq}, the black circle and the black asterisk represent an unstable and a stable equilibrium, respectively, and the black arrows indicate the tendency of the system in time.

scale system elements.

An example of an empirical model is that presented by Escoffier (1940) to describe the cross-sectional stability of a single inlet system. In this approach the amplitude of the tidal current in the inlet channel U was compared with a critical or equilibrium velocity U_{eq} at which no sediment erodes or deposits in the inlet channel over a tidal cycle. If U is smaller than U_{eq}, sediment deposits in the channel because the wave driven alongshore sediment transport going into the inlet channel is larger than the capacity of the tidal current to erode the channel bottom. Conversely, if U is larger than U_{eq}, the tide dominates over waves and the channel bottom will be eroded. The value of the equilibrium velocity was suggested to be of the order of 1 m s^{-1}, its value somewhat dependent on grain size and volume of littoral drift. U is amongst others a function of the cross-sectional area of the inlet channel A. The curve $U(A)$ is referred to as the *Escoffier curve* or *closure curve* and can be calculated by solving the governing hydrodynamic equations.

In calculating the closure curves Escoffier (1940), after Brown (1928), simplified the continuity equation by assuming a uniformly fluctuating sea surface el-

evation in the basin, also referred to as *pumping mode* or *Helmholtz mode*. Furthermore, the dynamics of the flow in the inlet constituted a balance between bottom friction and pressure gradient. Later, many other studies proposed hydrodynamic models using the pumping mode approach (Keulegan, 1951; van de Kreeke, 1967; Mehta & Özsoy, 1978; Walton Jr. & Escoffier, 1981; DiLorenzo, 1988). One such model that is used in this thesis is the *lumped-parameter model* (L-P model) introduced by Mehta & Özsoy (1978). In this model the dynamics of the flow are governed by inertia, entrance/exit losses and bottom friction on the one hand and the pressure gradient across the inlet on the other hand. Note that the selection of a particular model is not essential to the stability concept as proposed by Escoffier (1940).

For two arbitrary cases (the blue and red curve) a typical shape of the closure curve together with the equilibrium velocity U_{eq} is presented in Fig. 1.4. This figure shows that the tidal current amplitude has a maximum for a certain cross-sectional area. For smaller A, tidal currents decrease because of increasing frictional forces. For larger A, tidal currents decrease as well because the difference between the ocean tide and basin tide becomes smaller, resulting in a smaller water level gradient (for an explanation, see Appendix 1.A and de Swart & Zimmerman (2009)). Once the maximum value of the closure curve is larger than the equilibrium velocity (blue closure curve), there are two intersections referred to as *equilibriums*. Such an equilibrium is stable when after a perturbation the cross-sectional area returns to its original equilibrium value. Recalling that if $U > U_{eq}$, erosion prevails over deposition and A increases, whereas the opposite occurs if $U < U_{eq}$ (see black arrows for the tendency of the system). It follows that the equilibrium with the largest cross-sectional area represents a stable (black asterisk) and the other an unstable (black circle) equilibrium. For a cross-sectional area that is too small, or if the equilibrium velocity exceeds the maximum value of the closure curve (red line), the inlet closes.

Even though Escoffier presented his stability concept in 1940, it was not until the early seventies that engineers started to use it (O'Brien & Dean, 1972; van de Kreeke, 1985, 1992, 2004). This is probably related with some of the problems encountered when applying the concept to actual inlets (van de Kreeke, 2004). One such problem is that, assuming the same inlet geometry and forcing, the choice of the hydrodynamic model to calculate the closure curves may lead to large differences in equilibrium cross-sectional areas and, in some cases, even lead to different conclusions regarding inlet stability (Walton Jr., 2004).

van de Kreeke (1985, 1990a,b) and later Jain et al. (2004) studied the cross-sectional stability of double inlet systems along the Gulf coast of the United States. They extended the classical stability concept of Escoffier (1940) to account for two tidal inlets draining a single back-barrier basin. In the case of two inlets, tidal currents through these inlets are a function of both cross-sectional areas, $U_1(A_1, A_2)$ and $U_2(A_1, A_2)$, where the subscripts denote a specific inlet. To determine the values of the cross-sectional areas A_1 and A_2 for which both inlets

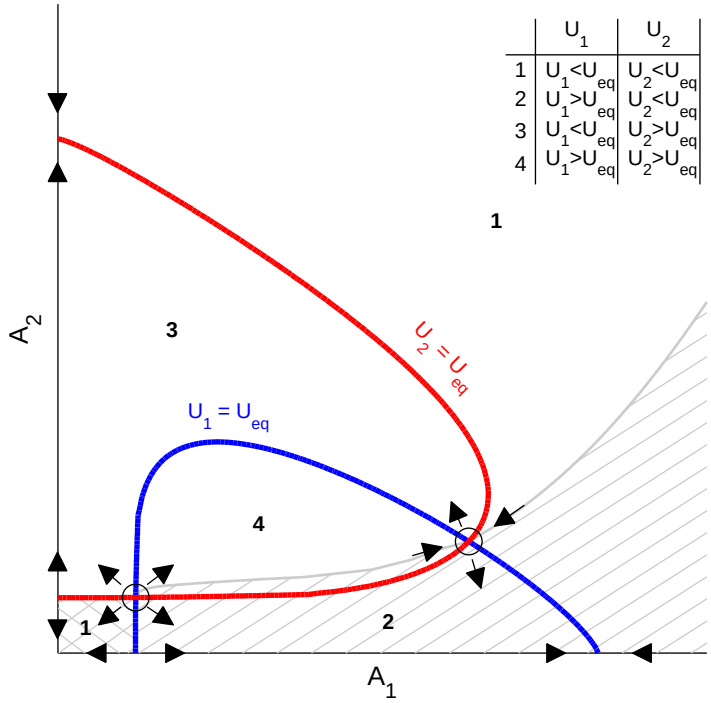

Figure 1.5: The equilibrium velocity curves $U_1(A_1, A_2) = U_{eq}$ (blue) and $U_2(A_1, A_2) = U_{eq}$ (red) for a double inlet system. The black circles represent an unstable equilibrium, the black arrows indicate the tendency of the system in time, the bold numbers refer to the magnitude of U_1 and U_2 relative to U_{eq} and the cross-, single- and non-hatched areas refer to a specific system tendency area (see main text for an explanation). Figure adapted from van de Kreeke (1990a).

are in equilibrium, use was made of the so-called *equilibrium flow curves*. The equilibrium flow curve of Inlet 1 represents the locus of the values (A_1, A_2) for which $U_1 = U_{eq}$. A similar definition holds for the equilibrium flow curve of Inlet 2. The intersections of the equilibrium flow curves represent combinations of (A_1, A_2) for which both inlets are in equilibrium. In Fig. 1.5 the equilibrium flow curve of Inlet 1 and Inlet 2 (blue and red curve, respectively), the corresponding equilibrium points (black circles), and the tendency of the system (black arrows) are sketched for an arbitrary case. The tendency of the system and therefore the stability of the equilibriums can be assessed in a similar fashion as was done by Escoffier (1940): if $U_k > U_{eq}$ $(k = 1, 2)$, erosion prevails over deposition and A_i increases, whereas the opposite occurs if $U_k < U_{eq}$. In Fig. 1.5, $U_1 > U_{eq}$ in the area enclosed by the blue equilibrium velocity curve and the x-axis and $U_2 > U_{eq}$ in the area enclosed by the red equilibrium velocity curve and the y-axis. Consequently, three different system tendency areas can be distinguished. If the system has initial values in the cross-hatched area, both inlets close. If the initial state is in the single-hatched area, then Inlet 2 closes and Inlet 1 remains open. Conversely, when starting in the non-hatched area, the first inlet closes

and the second inlet remains open. The general conclusion of these studies was that there is no stable equilibrium for which both inlets are open, i.e. the two equilibriums in Fig. 1.5 are both unstable. Ultimately, one of the inlets will close and only one inlet will connect the back-barrier area and the ocean.

Although not investigated in detail, van de Kreeke (1990a) reasoned that it is highly unlikely that a set of stable equilibrium cross-sectional areas can exist for a system with more than two inlets. Tambroni & Seminara (2006) applied the van de Kreeke (1990a) model to quantify the cross-sectional stability of the triple inlet system of Venice Lagoon. Unlike the observations, the results suggest that two inlets tend to close. They argued that actually the triple inlet system may be considered as three separate single inlet systems, which consequently all have a stable equilibrium.

1.5 Research questions

From the previous sections the following overarching problem can be formulated:

> *From previous model studies of cross-sectional stability of double inlet systems it was concluded that these systems cannot be stable, even though observations suggest that they can persist over a long period of time.*

To clarify this apparent contradiction, there is a need to enhance our knowledge of the underlying physical mechanisms that cause these systems to be cross-sectionally stable or unstable. To this end, the model proposed by van de Kreeke (1990a) will be extended to include additional physical processes that were neglected in the original modelling effort. Therefore, in this thesis the following research questions will be addressed:

Q1: *What is the effect of a topographic high on the cross-sectional stability of double inlet systems? Are sets of stable inlets possible?*

Q2: *Can the cross-sectional stability of a double inlet system be determined and explained using a lumped-parameter model including the assumption of a uniformly fluctuating basin level? In particular, what is the role of the different terms in the dynamic equation and the boundary conditions in determining the cross-sectional stability of the inlets?*

Q3: *How do spatial variations in surface elevation and basin geometry influence the cross-sectional stability of a double inlet system? Can the stabilising and destabilising mechanisms associated with cross-sectional stability be identified?*

1.6 Thesis structure and research approach

To answer the research questions formulated in the previous section, use is made of a modelling approach. The foundation of this approach is the stability concept for tidal inlets proposed by Escoffier (1940). To calculate the equilibrium flow curves, in Chapters 2 and 3 the equations underlying the empirical morphodynamic model or L-P model (see also Section 1.4) are solved numerically. Subsequently, in Chapter 4 a new two-dimensional, depth-averaged (2DH) modelling approach (after Roos & Schuttelaars, 2011) is used to explicitly account for spatial variations in surface elevation.

In Chapter 2, the influence of a topographic high on the cross-sectional stability of double inlet systems is investigated. These topographic highs are often observed in the back-barrier basins of barrier coasts. In this chapter the Marsdiep-Vlie system, which is part of the Dutch Wadden Sea, is taken as an example. As mentioned in Section 1.4 an inlet is in equilibrium when the amplitude of the inlet velocity equals the equilibrium velocity. This equilibrium is stable when after a perturbation the cross-sections of both inlets return to their original equilibrium value. The amplitudes of the inlet velocities are obtained using the L-P model. In this model, the basin surface elevation fluctuates uniformly and the inlets are schematised to prismatic channels with diverging entrance and exit sections. The dynamics of the flow in the prismatic sections of the tidal channels constitute a balance among longitudinal pressure gradient, inertia and bottom friction. In the diverging sections the balance is governed by the advective acceleration and the longitudinal pressure gradient, which leads to an entrance/exit loss term in the overall momentum balance. In the example of the Marsdiep-Vlie system the inlets are relatively long and entrance/exit losses are neglected because they are small compared to bottom frictional losses. To account for the topographic high, the basin is divided into two sub-basins. The surface elevation of each sub-basin is assumed to fluctuate uniformly. The dynamics of the flow across the topographic high is described analogous to that of the two inlets.

In Chapter 3, the effect of the different terms in the dynamic equation of the L-P model on the cross-sectional stability of double inlet systems is investigated. Of particular interest is the role of the entrance/exit loss term that has been neglected in previous studies on cross-sectional stability (e.g. van de Kreeke, 1990a) as well as in Chapter 2. The amplitudes of the inlet velocities are obtained using the L-P model mentioned in the previous paragraph, including entrance/exit losses and a uniformly fluctuating surface elevation. For relatively short inlets, e.g. in the Ría Formosa, southern Portugal, used as an example in this chapter, the entrance/exit loss term is the largest term in the momentum balance. As a result, entrance/exit losses might have an impact on the equilibrium configuration and stability properties of the double inlet system.

To investigate the influence of spatial variations in surface elevation in the basin, inlet and ocean on the cross-sectional stability of double inlet systems in more detail, Chapter 4 presents a newly developed 2DH hydrodynamic model. The water motion is described by the depth-averaged shallow water wave equations including linearised bottom friction and Coriolis effects. This new modelling approach explicitly allows for amplitude and phase differences within the basin. Furthermore, the tidal wave travelling past the inlet system is part of the solution, implying that the amplitude and phase differences are automatically calculated and need not be imposed externally. It is believed that modelling the double inlet system in this manner allows for a more thorough investigation of the system's stabilising and destabilising mechanisms.

In the final chapter the conclusions from the previous chapters are summarized and the research questions are answered. Furthermore, recommendations are given for further research.

1.A Shape of the Escoffier curve

In this appendix the shape of the Escoffier curve or closure curve for single inlet systems is discussed. This curve represents the relation between the amplitude of the inlet velocity U and the inlet cross-sectional area A. For the analysis below reference is made to Fig. 1.4.

Consider a tidal basin with surface area B that is connected to the ocean by a prismatic channel with length L and hydraulic radius R. The basin is assumed to be relatively small and deep and its surface elevation ζ_b is assumed to fluctuate uniformly. As a result, continuity is described by

$$B\frac{d\zeta_b}{dt} = Au, \tag{1.A.1}$$

Additionally, the momentum equation constitutes a balance among inertia, bottom friction and pressure gradient over the inlet:

$$\frac{du}{dt} = -\frac{g}{L}(\zeta_b - \zeta_0) - \frac{F}{R}u|u|. \tag{1.A.2}$$

Here, B is basin surface area (m^2), ζ_b is basin surface elevation (m), t is time (s), A is inlet cross-sectional area (m^2), u is cross-sectional averaged inlet velocity (m s^{-1}), g is gravitational acceleration (m s^{-2}), L is inlet length (m^2), ζ_0 is ocean surface elevation (m), F is a bottom friction coefficient (-) and R is inlet hydraulic radius (m). In Eq. (1.A.2) the term on the left-hand side is inertia, the first term on the right-hand side represents the pressure gradient over the inlet and the second term on the right-hand side represents inlet bottom friction.

To explain the shape of the Escoffier curve depicted in Fig. 1.4, an expression for $U(A)$ is sought. Linearising the non-linear bottom friction term in Eq. (1.A.2) according to Lorentz' linearisation (Lorentz, 1926; Zimmerman, 1982), $u|u| = (8/3\pi)Uu$, assuming $R = \gamma\sqrt{A}$, with γ being an inlet shape factor, and taking the derivative with respect to t leads to

$$\frac{d^2u}{dt^2} = -\frac{g}{L}\left(\frac{d\zeta_b}{dt} - \frac{\zeta_0}{dt}\right) - \frac{F'}{\gamma\sqrt{A}}\frac{du}{dt}, \tag{1.A.3}$$

where $F' = 8FU/3\pi$ is the modified bottom friction coefficient. Substituting Eq. (1.A.1) into Eq. (1.A.3) yields

$$\frac{d^2u}{dt^2} = -\frac{g}{L}\left(\frac{A}{B}u - \frac{d\zeta_0}{dt}\right) - \frac{F'}{\gamma\sqrt{A}}\frac{du}{dt}, \tag{1.A.4}$$

Now, a trial solution is introduced for u and ζ_0 of the form

$$u \sim \Re\left\{\hat{u}e^{i\omega t}\right\}, \qquad \zeta_0 \sim \Re\left\{Z_0 e^{i\omega t}\right\}, \tag{1.A.5}$$

where $\Re$ is the real part, $\hat{u}$ is the complex amplitude of the inlet velocity, ω is the radial frequency (s^{-1}) and Z_0 is the real-valued amplitude of the ocean tide (m). Substituting these trial solutions in Eq. (1.A.4) leads to

$$-\omega^2\hat{u} = -\frac{g}{L}\left(\frac{A}{B}\hat{u} - i\omega Z_0\right) - \frac{i\omega F'}{\gamma\sqrt{A}}\hat{u}. \tag{1.A.6}$$

Rearranging terms and taking the absolute value of Eq. (1.A.6) yields an expression for the amplitude of the inlet velocity U as a function of the inlet's cross-sectional area A

$$U(A) = |\hat{u}| = \frac{Z_0}{\sqrt{\left(\frac{A}{\omega B} - \frac{\omega L}{g}\right)^2 + \left(\frac{F'L}{g\gamma\sqrt{A}}\right)^2}}. \tag{1.A.7}$$

In Eq. (1.A.7) the first term between brackets in the denominator can be associated with the pressure gradient ($A/\omega B$) and inertia ($\omega L/g$). The second term between the brackets in the denominator ($F'L/\omega\gamma\sqrt{A}$) is bottom friction.

To explain the shape of the Escoffier curve depicted in Fig. 1.4, it is reasonable to assume that inertia is small compared to the pressure gradient. Hence, $A/\omega B \gg \omega L/g$ or $\omega_0^2/\omega^2 \gg 1$, where $\omega_0 = \sqrt{gA/LB}$ is the Helmholtz frequency or eigenfrequency of the single inlet system. As a result, Eq. (1.A.7) can be recast to

$$U(A) = \frac{Z_0}{\sqrt{aA^2 + \frac{b}{A}}}, \tag{1.A.8}$$

where $C_{pg} = 1/(\omega B)^2$ and $C_{bf} = (F'L/g\gamma)^2$ are bulk coefficients for pressure gradient and bottom friction, respectively. It follows that for $A \downarrow 0$, $U(A)$ is dominated by bottom friction and $U(A) \to 0$. On the other hand, for $A \to \infty$, $U(A)$ is dominated by the pressure gradient and $U(A) \to 0$. In between the limits of $A \downarrow 0$ and $A \to \infty$ a cross-sectional area A_{cr} exists where $U = U_{max}$. A_{cr} can be determined by solving $dU(A)/dA = 0$ for A. Still neglecting inertia and taking the derivative of Eq. (1.A.7) with respect to A leads to

$$\frac{dU}{dA} = \frac{Z_0(C_{bf} - 2C_{pg}A^3)}{2A^2\left(\frac{C_{pg}A^3 + C_{bf}}{A}\right)^{3/2}}, \tag{1.A.9}$$

For dU/dA to be zero, the numerator in Eq. (1.A.9) needs to be zero. Hence, when neglecting inertia, the critical cross-sectional area U_{cr} where $U = U_{max}$ is:

$$A_{cr}^3 = \frac{C_{\text{bf}}}{2C_{\text{pg}}}. \tag{1.A.10}$$

Substituting the expression for A_{cr} into Eq. (1.A.7) results in the corresponding maximum inlet velocity U_{max}

$$U_{max} = Z_0 \left(\frac{4}{27} \frac{1}{C_{\text{pg}} C_{\text{bf}}^2} \right)^{1/6}. \tag{1.A.11}$$

The value of U_{max} in relation to the equilibrium velocity U_{eq} determines the number of equilibriums found: if $U_{eq} < U_{max}$, two equilibriums exist; if $U_{eq} = U_{max}$, one equilibrium exists; and if $U_{eq} > U_{max}$, no equilibriums exist.

For systems where $\omega_0^2/\omega^2 \sim 1$, inertia cannot be neglected and finding an expression for A_{cr}, and hence U_{max}, is not so straightforward.

2

Influence of a topographic high on cross-sectional inlet stability*

Abstract The cross-sectional stability of two tidal inlets connecting the same back-barrier basin to the ocean is investigated. The condition for equilibrium is that the amplitude of the inlet velocities simultaneously equal the equilibrium velocity. The equilibrium is stable when after a perturbation the cross-sectional areas return to their original equilibrium values. In an earlier study, using the same equilibrium condition, it was concluded that where two inlets connect the same basin to the ocean ultimately one inlet will close. One of the major assumptions in that study was that the water level in the basin fluctuated uniformly. However, in the Dutch Wadden Sea the back-barrier basin consists of a series of basins, rather than one single basin, separated by topographic highs. These topographic highs limit but do not exclude the exchange of water between the sub-basins. Therefore, in the model schematisation the water level in the sub-basins, rather than in the back-barrier as a whole, is assumed to fluctuate uniformly. Furthermore, the system is forced by a simple sinusoidal tide where amplitudes and phases may differ between the two inlets. Due to non-linear bottom friction, the hydrodynamic equations are solved using a finite difference

*This chapter is based on the papers *"The effect of a topographic high on the morphological stability of a two-inlet bay system"* by J. van de Kreeke, R.L. Brouwer, T.J. Zitman and H.M. Schuttelaars (2008), Coast. Eng. 55, pp. 319-332; and *"Effects of amplitude differences on equilibrium and stability of a two-inlet bay system"* by R.L. Brouwer, J. van de Kreeke, H.M. Schuttelaars and T.J. Zitman (2008), Conference Proceedings RCEM 2007, Enschede, The Netherlands, Vol. 1, pp. 33-39.

method. The results, together with the equilibrium condition, yield the equilibrium flow curve for each of the inlets. The intersections of the two equilibrium flow curves represent combinations of cross-sectional areas for which both inlets are in equilibrium. The stability of the equilibriums are assessed by means of a so-called flow diagram in which the equilibrium flow curves together with vectors that indicate the system's tendency are displayed. Calculations were carried out for different openings over the topographic high and forcing conditions. The results show that for relatively large openings, approaching the situation of a single basin, there are no combinations of inlet cross-sectional areas for which both inlets are in a stable equilibrium. This supports the conclusion in the earlier study mentioned above. For relatively small openings there is one set of stable equilibriums. In that case the double inlet system approaches that of two single inlet systems. In between relatively small and large openings, one or two sets of stable equilibriums are found depending on the cross-sectional area of the topographic high and the forcing conditions.

2.1 Introduction

A considerable part of the world's coasts consists of barrier islands. These islands are separated by tidal inlets, relatively short and narrow channels that connect the back-barrier basins to the ocean. Restricting attention to inlets that are scoured in loose-granular material, the cross-sectional area of these inlets takes on a value where on an averaged annual basis the sand transport into the inlet equals the sand transport out of the inlet. The actual cross-sectional area oscillates about this equilibrium value. When the oscillations become too large, the inlet cross-section could become unstable and the inlet might close.

It was Escoffier (1940) who first proposed a method to determine the equilibrium and stability of a tidal inlet. He reasoned that the equilibrium values of the inlet cross-sectional areas are the intersections of the closure curve (the relationship of the amplitude of the inlet velocity and the inlet cross-sectional area) and an empirical quantity, the equilibrium velocity (see Section 1.4). In general there will be two intersections, one representing a stable and the other an unstable equilibrium.

Until recently, most studies on cross-sectional stability of tidal inlet systems concentrated on single inlet systems (e.g. Escoffier, 1940; O'Brien & Dean, 1972; van de Kreeke, 2004), even though the majority of back-barrier basins are connected to the ocean by more than one inlet. An exception is the study by van de Kreeke (1990a), who specifically addressed the stability of multiple-inlet bay systems thereby taking into account the interaction of the inlets. In this study it was concluded that, where more than one inlet connects a tidal basin to the ocean, inlets cannot be in a stable equilibrium simultaneously. Ultimately only one in-

let will remain open and the others will close. In arriving at this conclusion a number of assumptions were made with regards to morphometry and boundary conditions. The tidal inlet system was schematised as a basin and two prismatic inlet channels. Inlet channels were assumed to be relatively long making entrance/exit losses small compared to bottom friction losses. Furthermore, in describing the inlet dynamics inertia was neglected. The basin dimensions were assumed to be small compared to tidal wave length, justifying the assumption of a uniformly fluctuating water level (pumping mode). The ocean tides off the two inlets were assumed to be the same and simple harmonic. This simplified model was believed to represent sufficiently the relevant hydrodynamic processes affecting stability.

In hindsight, some of the assumptions in van de Kreeke (1990a) might be too restrictive as there are examples of inlets connecting the same basin to the ocean that have been in a stable equilibrium for centuries (see also Section 1.3 on page 4). Examples are the inlets of the Venice Lagoon (Tambroni & Seminara, 2006), the Ría Formosa (Salles et al., 2005) and the Wadden Sea (Louters & Gerritsen, 1994). A closer look at, for example, the Wadden Sea system shows that the back-barrier basin consists of a series of basins as opposed to a single basin (Fig. 1.2 on page 5). These basins are separated by topographic highs. The topographic highs are roughly located at places where the tides entering the inlets meet. They act as semi-permeable barriers that allow a certain degree of exchange of water between the two sub-basins. Hence, the assumption of a uniformly fluctuating basin surface elevation might be valid for the sub-basins but not for the basin as a whole.

The main aim of this chapter is to extend the model in van de Kreeke (1990a) by including the effects of topographic highs and to use this model to study the existence and stability of double inlet systems. Hence the basin is divided in two sub-basins by a topographic high. Based on observations in the Wadden Sea the topographic high extends across the basin and has a uniform elevation somewhat below the mean water level to allow for exchange between the sub-basins. The schematisation for the double inlet system with topographic high is presented in Fig. 2.1. In addition to including a topographic high, inertia has been added to the dynamic equations for the inlet flow. The system is forced by sinusoidal tides off the inlets that can differ in amplitude as well as in phase.

The aforementioned relatively simple schematisation and model has the advantage that it can be used as a diagnostic tool to gain further insight into the mechanisms causing or hampering stability of multiple inlet systems. Unfortunately, the addition of a topographic high and the inclusion of inertia in the dynamic equations for the inlet flow do not allow an analytical solution to the stability problem as used in van de Kreeke (1990a). Instead, recourse has to be taken to a numerical approach.

This chapter is organised as follows. In Section 2.2, the definitions for equilibrium and stability of a double inlet system are given. In addition, a visual tool to

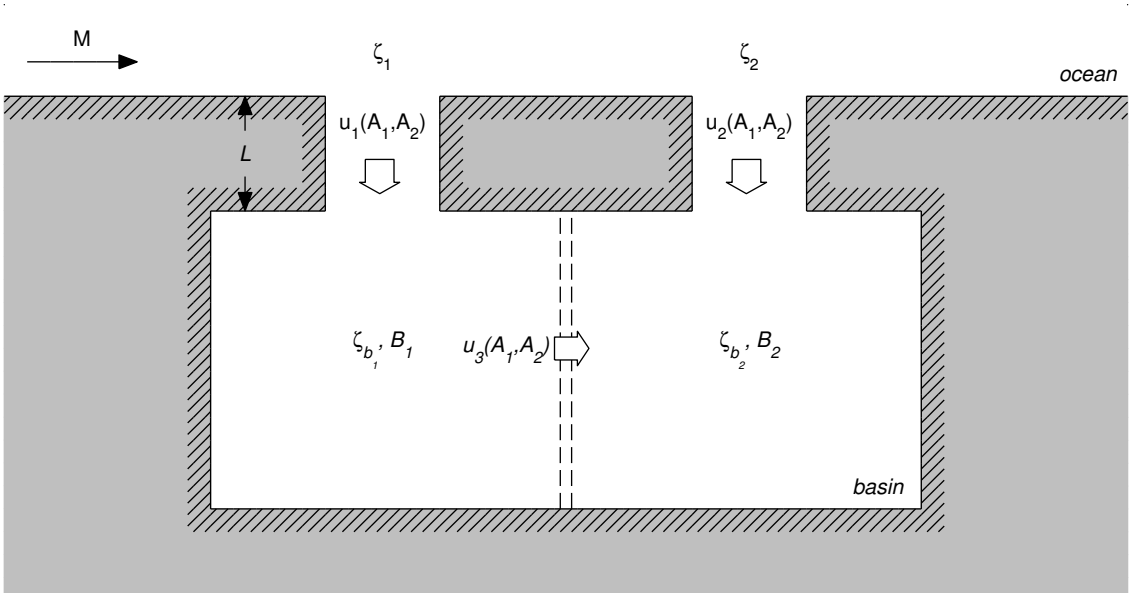

Figure 2.1: Schematisation of a double inlet system with topographic high.

rapidly assess this equilibrium and stability is introduced. This tool is referred to as a *flow diagram*. In Section 2.3, the hydrodynamic model, necessary to construct the flow diagram, is presented. Section 2.4 contains the numerical experiments to investigate the influence of a topographic high and differences in the forcing on the equilibrium configuration and stability properties of double inlet systems. Finally, Sections 2.5 and 2.6 present the discussion and conclusions, respectively .

2.2 Equilibrium and stability

2.2.1 General

The focus of this chapter is on conditions for which both inlets are in a stable equilibrium. In determining the equilibrium value of the cross-sectional area of an inlet, the basic premise is that on an annual averaged basis the volume of sand transported into the inlet is constant, its value depending on the littoral drift. This influx of sand is balanced by the transport of sand out of the inlet by the ebb tidal currents. In principle, when the flow field is known, the sand transported out of the inlet can be calculated using relationships between velocity and transport. However, in using this procedure there are several difficulties in arriving at reliable estimates of the transport. These include:

- Sand transport, in addition to tidal flow, is a function of waves. The relation

between sediment transport and velocity field induced by tide and waves is not well known.

- Sand transport is largely in the form of suspended load; accurate modelling is difficult as the suspended transport, in addition to the velocity field in the inlet, depends on the velocity field and sediment transport processes in the back-barrier basin including erosion and deposition.
- Residual (tidally averaged) transport depends on non-linearities in the flow which require a highly accurate hydrodynamic model.

In view of these difficulties, in this study a more pragmatic approach is taken. Instead of calculating sand transport, the well-known empirical relationship between inlet cross-sectional area and ebb tidal prism for inlets at equilibrium is used. The approach is described in detail in Sections 2.2.2 and 2.2.3.

2.2.2 Equilibrium velocity

For inlets at equilibrium the following relationship between cross-sectional area and tidal prism exists (O'Brien, 1931)

$$A_k = CP_k^q, \tag{2.1}$$

where A is cross-sectional area of inlet k (m^2) and P_k its ebb tidal prism (m^3). A_k and P_k are considered annually averaged values. C and q are constants that among other things are functions of volume of littoral drift and grain size. Eq. (2.1) was initially introduced as an empirical relationship and only recently attempts have been made to give this relationship a physical footing (van de Kreeke, 1998, 2004; Kraus, 1998; Suprijo & Mano, 2004).

For purposes of this study it is convenient to express the equilibrium condition, Eq. (2.1), in terms of velocity. For this the characteristic velocity U_k is introduced, where k is the number of the inlet. Approximating the inlet velocity by a sine with amplitude U_k and period T, the tidal prism P_k is defined as the volume of water that is exiting the tidal inlet during the ebb phase

$$P_k = A_k \int_0^{\frac{T}{2}} U_k \sin(\tfrac{2\pi}{T}t)dt. \tag{2.2}$$

Consequently, the characteristic velocity U_k reads

$$U_k = \frac{\pi P_k}{A_k T}, \tag{2.3}$$

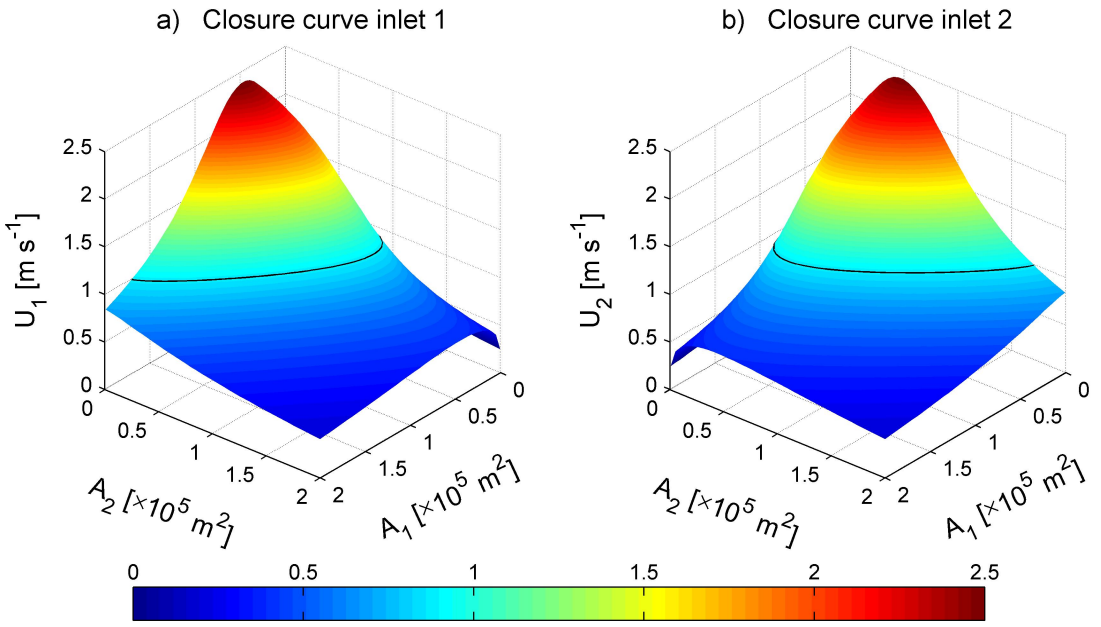

Figure 2.2: Closure surfaces for (a) Inlet 1 and (b) Inlet 2. The black contours are the equilibrium flow curves. Calculations carried out using the hydrodynamic model described in Section 2.3 and parameter values denoted in Table 2.1.

where k refers to Inlet 1 and 2. Because the tidal prism is a function of both A_1 and A_2, the characteristic velocity U_k is a function of A_1 and A_2:

$$U_k = f(A_1, A_2). \tag{2.4}$$

Eq. (2.4) represents a surface referred to as the *closure surface*, which is equivalent to the closure curve for single inlet systems. A typical shape of the closure surface for the inlets is presented in Figs. 2.2a and 2.2b. Referring to the closure surface for Inlet 1 in Fig. 2.2a, for constant A_2 values of U_1 increase with increasing values of A_1, reaching a maximum and subsequently decreases gradually to a zero value for large A_1. For constant values of A_1, U_1 monotonically decreases with increasing values of A_2. Using Fig. 2.2b, a similar description holds for the closure surface of Inlet 2.

It follows from Eqs. (2.1) and (2.3) that for inlets that are in equilibrium

$$U_k = U_{eq} = \frac{\pi}{TC^{1/q}} A_k^{(1/q)-1} \tag{2.5}$$

Values of q, C and T are assumed to be the same for both inlets. For the Dutch Wadden Sea, and using the metric system, to a good approximation $q = 1$, $C = 6.8 \cdot 10^{-5}$ m^{-1} and $T = 44,712$ s (van de Kreeke, 1998). With $q = 1$, it follows

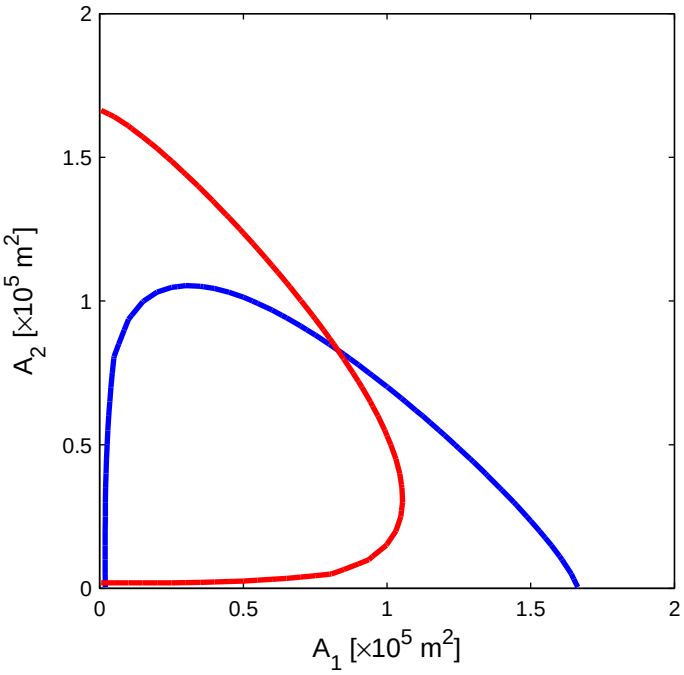

Figure 2.3: Equilibrium flow curves for Inlet 1 (blue) and Inlet 2 (red). Calculated using the hydrodynamic model described in Section 2.3 and parameter values denoted in Table 2.1.

from Eq. (2.5) that U_{eq} is independent of A_k. Therefore, for identical C and T, U_{eq} is the same for both inlets and equal to $U_{eq} = 1.03 \sim 1\ \mathrm{m\ s^{-1}}$. U_{eq} will be referred to as the *equilibrium velocity*.

To determine the values of (A_1, A_2) for which both inlets are in equilibrium, use is made of the so-called *equilibrium flow curves*. The equilibrium flow curve of Inlet 1 represents the locus of the values (A_1, A_2) for which for that inlet $U_k = U_{eq}$ and similarly for Inlet 2. Geometrically, the equilibrium flow curve for Inlet 1 is the intersection of the plane $U_1 = U_{eq}$ with the closure surface of Inlet 1 and similar for Inlet 2 (see also Fig 2.2). A typical example of equilibrium flow curves for a two-inlet bay system is presented in Fig. 2.3. The intersections of the equilibrium flow curves represent combinations of (A_1, A_2) for which both inlets are in equilibrium.

2.2.3 Stability and flow diagram

An inlet is in a stable equilibrium, when after having been perturbed, it will return to that equilibrium. In the case of the double inlet system the stability of the equilibrium can be determined by visual inspection of the configuration of the equilibrium flow curves in the neighbourhood of the equilibrium. The

criterion is that when $U_k > U_{eq}$ the inlet cross-sectional area will increase and when $U_k < U_{eq}$ the cross-sectional area will decrease. An example of determining the stability in this fashion can be found in Jain et al. (2004).

A more unambiguous approach would be to apply a linear stability analysis. However, the results of this analysis would be limited to the (A_1, A_2) space in close proximity of the equilibrium. Instead, in this study a *flow diagram* is used. A flow diagram consists of the equilibrium flow curves together with a vector plot. The vectors represent the adaptation, or more precisely the rate of change of the cross-sectional areas, dA_1/dt and dA_2/dt, after both cross-sections have been removed from equilibrium. The vectors are defined as

$$\frac{d\vec{A}}{dt} = \frac{dA_1}{dt}\vec{e}_1 + \frac{dA_2}{dt}\vec{e}_2, \tag{2.6}$$

where $\vec{e}_1$ and $\vec{e}_2$ are the unit vectors in respectively the direction of the A_1-axis and A_2-axis. The rate of change of the cross-sectional areas of the inlets can be related to the characteristic velocity as follows. The value of $q = 1$ for the Wadden Sea inlets corresponds to an annually averaged transport of sand during the ebb period (export) that is proportional to a power n of the characteristic velocity (van de Kreeke, 2004),

$$TR_k = sU_k^n. \tag{2.7}$$

TR_k is a volume transport in inlet k ($m^3\ s^{-1}$) and s is a dimensional constant, its value dependent on sand characteristics. n is a constant with a value between 3 and 5. On an annually averaged basis the volume of sand entering the inlet, M, is taken to be a fraction of the volume of littoral drift. When the inlet is in equilibrium, and assuming no exchange of sediment between inlet channel and back-barrier basin, sediment import M equals sediment export TR_k^{eq}:

$$M = TR_k^{eq} = sU_{eq}^n. \tag{2.8}$$

M is assumed to be independent of the cross-sectional area of the inlet. Furthermore, the rate of change of cross-sectional area A_k is

$$L_k\frac{dA_k}{dt} = sU_k^n - sU_{eq}^n, \qquad A_k > 0. \tag{2.9}$$

L_k is the length of the inlet channel (m). The assumption here is that the entire length of the channel is involved in the shoaling process. Applying the foregoing

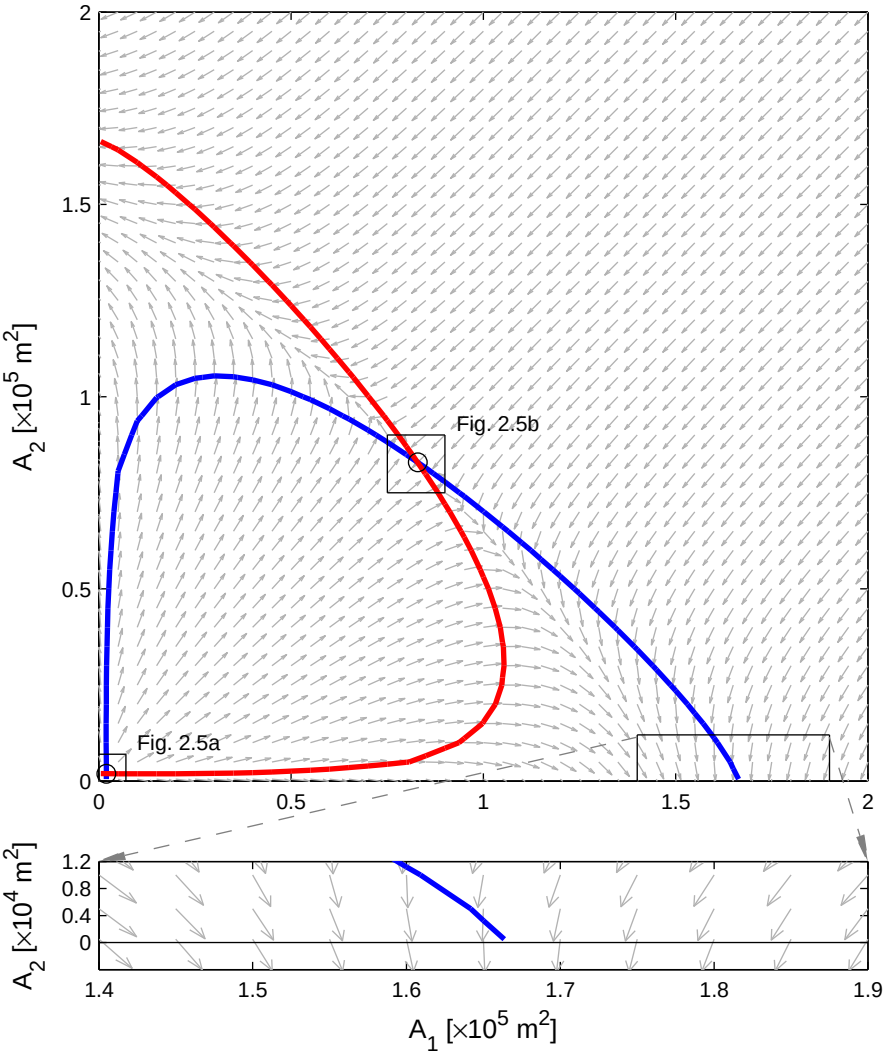

Figure 2.4: Flow diagram for a double inlet system with a relatively large cross-sectional area of the topographic high ($A_3 = 1 \times 10^6$ m^2). The blue and red line correspond to the equilibrium flow curve of Inlet 1 and Inlet 2, respectively. The grey arrows indicate the system's tendency.

to a double inlet system and assuming M to be the same for both inlets (van de Kreeke, 2004),

$$\frac{dA_k}{dt} = \frac{M}{L_k}\left[\left(\frac{U_k}{U_{eq}}\right)^n - 1\right], \qquad k = 1, 2, \qquad A_k > 0. \tag{2.10}$$

Making use of Eqs. (2.6), (2.10) and (2.11)-(2.15) (to be discussed in the next section), an example of a flow diagram is presented in Fig. 2.4. For the parameter values used to construct the diagram reference is made to Table 2.1. (note: the equilibrium flow curves in this figure are the same as those presented in Fig. 2.3).

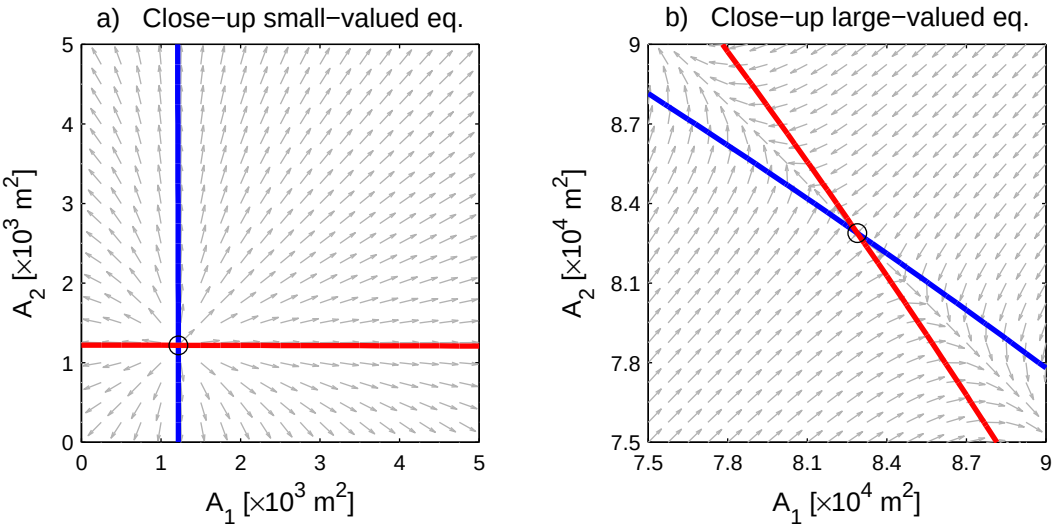

Figure 2.5: (a) Close-up around the small-valued equilibrium in Fig. 2.4 and (b) close-up around the large-valued equilibrium in Fig. 2.4. The blue and red line correspond to the equilibrium flow curve of Inlet 1 and Inlet 2, respectively. The grey arrows indicate the system's tendency.

Because here the direction rather than the magnitude of the vector is of interest, vectors dA_k/dt in the flow diagram are given a unit length. There are two intersections of the equilibrium flow curves and therefore there are two equilibriums for which both inlets are open. Directions of the vectors in the vicinity of the equilibriums show whether after a perturbation the system will respond by returning to the equilibrium or moving further away from it. For this the flow diagrams in the vicinity of the equilibriums are enlarged in Fig. 2.5. From the direction of the vectors it follows that both equilibriums are unstable.

For the interpretation of the vectors near the axis of the flow diagram it should be realised that for $A_k = 0$ there exists a discontinuity in the value of dA_k/dt. In the neighbourhood of $A_k = 0$, U_k is a monotonously increasing function of A_k (van de Kreeke, 2004). With $U_k < U_{eq}$ it then follows from Eq. (2.10) that dA_k/dt is negative with a magnitude that monotonously increases with decreasing value of A_k. The cross-sectional area decreases faster as A_k becomes smaller, which from a physics point of view seems reasonable. Furthermore, from Eq. (2.10) when $A_k \downarrow 0$ the rate of change of dA_k/dt approaches a constant value $dA_k/dt = -M/L_k$. Since the model does not allow for $A_k \leq 0$ (physically unrealistic), $dA_k/dt = 0$ for $A_k = 0$, corresponding to a closed inlet. At first sight this discontinuity in dA_k/dt might seem strange but there is a simple explanation by comparing with the velocity of a falling stone. The velocity of the falling stone increases to reach a maximum just before reaching the bottom. When touching the bottom the velocity abruptly goes to zero.

The discontinuity in dA_k/dt for values of A_k approaching zero leads to some peculiarities in the flow diagram near the axis. In particular, vectors do not point

to the intercept of equilibrium flow curve and axis. To further explain this an enlarged figure of the area in the neighbourhood of the intercept of the equilibrium flow curve for Inlet 1 and the A_1 axis is presented as an inset in Fig. 2.4. Near this intercept, Inlet 2 is relatively small and it is closing rapidly. This process ends abruptly as soon as Inlet 2 is closed. Simultaneously, Inlet 1 evolves asymptotically and at a far smaller rate towards its equilibrium. This is reflected by the direction of the vectors in the figure. Their vertical components (dA_2/dt) are much larger than their horizontal ones (dA_1/dt). However, these horizontal components do point towards the equilibrium flow curve, indicating that the intercept corresponds to a stable equilibrium for Inlet 1 when Inlet 2 is closed. Although not shown in the figure, a similar close look at the other intercept of the equilibrium flow curve for Inlet 1 with the A_1 axis reveals that horizontal components of nearby vectors point away from that intercept. This corresponds to an unstable equilibrium for Inlet 1 when Inlet 2 is closed. Hence, in the limiting case where $A_2 \downarrow 0$, our model converges to the type of behaviour that is expected for a single inlet system: one stable and one unstable equilibrium, in conformity with the theory of Escoffier (1940).

2.3 Hydrodynamic model

The response of the inlet's cross-sectional area and the equilibrium state (see Eq. (2.10) on page 29) is governed by the amplitude of the inlet velocities U_k (k=1,2). These velocities are calculated using a L-P model. For the schematisation of the double inlet system with topographic high reference is made to Fig. 2.1. The basin surface area is assumed to fluctuate uniformly, i.e. the water surface in the bay remains horizontal throughout the tidal cycle. The inlet channels of the Dutch Wadden Sea are short compared to the length of the tidal wave, so that gradients of the cross-sectionally averaged velocity in the direction of the channel axis can be neglected. However, channels are long enough for bottom friction losses to dominate over entrance/exit losses. The inlet channels are relatively deep and as a result tidal variations in water level can be neglected. The shape of the inlets are assumed to be triangular. The resulting momentum equations for the two tidal inlets are

$$\frac{L_k}{g}\frac{du_k}{dt} + \frac{F_k L_k}{g R_k}|u_k|u_k = \zeta_k - \zeta_{b_k}, \qquad k = 1,2. \tag{2.11}$$

The topographic high is introduced as a barrier with a uniform elevation and extending across the basin (see Fig. 2.1). The associated momentum equation is

$$\frac{L_3}{g}\frac{du_3}{dt} + \frac{F_3 L_3 W_{\text{th}}}{g A_3}|u_3|u_3 = \zeta_{b_1} - \zeta_{b_2}. \tag{2.12}$$

In Eqs. 2.11 and 2.12, L_k denotes the length of the two inlets (k=1,2) or the topographic high (k=3) (m); $g \approx 9.81$ m s^{-2} the gravitational acceleration; u_k the tidal current in the two inlets (k=1,2) or over the topographic high (k=3) (m s^{-1}); t time (s); F_k the dimensionless bottom friction factor of the two inlets (k=1,2) or the topographic high (k=3) (-); R_k the hydraulic radius of the two inlets (k=1,2); W_{th} the cross-basin width of the topographic high (m); ζ_k the sea surface elevation off inlet k (k=1,2) (m); and ζ_{b_k} the surface level elevation of sub-basin k (k=1,2) (m).

Because the sub-basins are assumed to be relatively small and deep the water level to a good approximation fluctuates uniformly in each sub-basin, however not for the basin as a whole. The continuity equations for both sub-basins read

$$B_k \frac{d\zeta_{b_k}}{dt} = A_k u_k + (-1)^k A_3 u_3, \qquad k = 1, 2, \tag{2.13}$$

where B_k is the surface area of sub-basin k (m^2); A_k is the cross-sectional area of the two inlets (k=1,2); and A_3 is the cross-sectional area of the topographic high (m^2).

To relate the hydraulic radius R_k of the two inlets to the cross-sectional area, the cross-sections are assumed to be geometrically similar for all values of the cross-sectional area (following O'Brien & Dean, 1972). Hence, the ratio of all corresponding lengths for two cross-sections are the same. This allows writing

$$R_k = \gamma \sqrt{A_k}, \qquad k = 1, 2, \tag{2.14}$$

where γ is a shape factor (-), which is assumed to be constant.

The tidal motion in the inlets is forced by a semi-diurnal harmonic constituent, where amplitudes and phases may differ between the two inlets,

$$\zeta_k = \Re \left\{ \hat{\zeta}_k e^{i\omega t} \right\}, \quad \text{with} \quad \hat{\zeta}_k = Z_k e^{i\theta_k}, \tag{2.15}$$

where $\Re$ denotes the real part, $\omega = 1.4 \times 10^{-4}$ s^{-1} is the angular frequency of the M2-tide, $\hat{\zeta}_k$ is the complex amplitude of the ocean tide at inlet k, Z_k is the real-valued amplitude of the ocean tide at inlet k (m) and θ_k the phase of the ocean tide at inlet k (rad).

The solution method for the non-linear system introduced in this subsection can be found in Appendix 2.A.

2.4 Numerical experiments

In the following section results will be shown of numerical experiments that are aimed at elucidating the influence of a topographic high on the equilibrium

Table 2.1: Parameter Values Representative for The Marsdiep-Vlie System in the western Dutch Wadden Sea

Parameter	Symbol	Dimension	Value
Topographic high width	W_{th}	m	25×10^3
Inlet length[a]	L_k	m	5×10^3
Shape factor[a]	γ_k	-	0.066
Bottom friction factor[a]	F_k	-	4×10^{-3}
Equilibrium velocity	U_{eq}	m s^{-1}	1.03
Basin area	B_k	m^2	7×10^8
Radian frequency	ω	s^{-1}	$1.4\cdot10^{-4}$
Forcing amplitude[b]	Z_k	m	0.80
Forcing phase[b]	θ_k	rad	0
Littoral drift	M	m^3 year^{-1}	$5\cdot10^5$

[a] identical for both inlets, however they are allowed to differ.
[b] default value.

configuration and stability properties of a double inlet system. In particular, the effect of the wetted cross-sectional area of the topographic high, A_3, on the number of equilibriums and their stability is investigated under the influence of symmetrical forcing (Section 2.4.1), forcing with amplitude differences only (Section 2.4.2) and forcing with phase differences only. The results are presented for a double inlet system with parameter values representative for the Marsdiep-Vlie system in the western Dutch Wadden Sea (Table 2.1; see also Section 1.3, page 4). For clarity, in the numerical experiments situations are sought that indicate for what conditions one or more sets of stable inlets are present.

2.4.1 Equilibrium configuration under symmetrical forcing

In the case of symmetrical forcing, flow diagrams for wetted cross-sectional areas of 25×10^3 m^2, 50×10^3 m^2 and 75×10^3 m^2 are presented in Fig. 2.6. For the remaining parameter values reference is made to Table 2.1. Cross-sections of the inlet channel are assumed triangular with slopes that make a 1° angle with the horizontal, resulting in a shape factor $\gamma = 0.066$ denoted in Table 2.1 (see also van de Kreeke, 1990a). For the smallest cross-section of the topographic high the flow diagram is presented in Fig. 2.6a. There are four equilibriums, only one of these is stable (indicated with the black cross). Note that when the cross-section of the topographic high goes to zero, the equilibrium flow curves for inlets 1 and 2 reduce to two sets of lines that are parallel to respectively the A_2- and the A_1-axis. This situation corresponds to two *separate* single inlet systems that have no interaction with each other. For the largest opening, Fig. 2.6c, two equilibriums

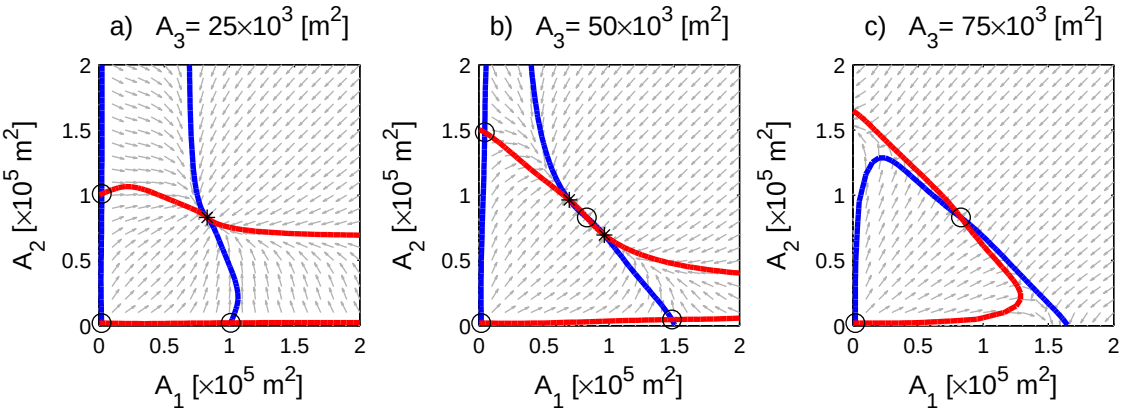

Figure 2.6: Flow diagrams for a double inlet system with a cross-sectional area of the topographic high of (a) $A_3 = 25 \times 10^3$ m^2, (b) $A_3 = 50 \times 10^3$ m^2, and (c) $A_3 = 75 \times 10^3$ m^2, respectively. The blue and red line correspond to the equilibrium flow curve of Inlet 1 and Inlet 2, respectively. The grey arrows indicate the system's tendency. The black circles indicate unstable and the black asterisks indicate stable equilibriums.

exist that are both unstable. The system is reduced to a double inlet system without a topographic high. For the flow diagram of the intermediate cross-section, Fig. 2.6b shows that six equilibriums are present, two of which are stable. To aid the interpretation of this figure, a detailed flow diagram covering the region including the two stable equilibriums in Fig. 2.6b is presented in Fig. 2.7.

The foregoing suggests that depending on the size of the cross-sectional area of the topographic high there can be one or more stable equilibriums. To precisely investigate the dependency of the number of equilibriums and their stability on the size of the topographic high, additional calculations were carried out for values of A_3 ranging from 20×10^3 m^2 to 80×10^3 m^2 as shown in Fig. 2.8. In this figure the cross-sectional area of Inlet 1, A_1, is plotted against the cross-sectional area of the topographic high, A_3. Notice, that a similar figure can be constructed for the cross-sectional area of Inlet 2. This, however, would not yield additional information because a symmetric double inlet system is assumed, i.e. parameter values of both inlets are identical. Furthermore, because the interest here is in the evolution of the stable equilibriums, the unstable equilibrium found in Fig. 2.6 close to $(A_1, A_2) = (0, 0)$ is omitted from this figure. Fig. 2.8 indicates that for values of A_3 smaller than approximately 30×10^3 m^2 one stable equilibrium exists (denoted by the blue diamonds). As an example, the black dotted line represents the equilibrium configuration of the flow diagram in Fig. 2.6a. Subsequently, for A_3 ranging between approximately 30×10^3 and 68×10^3 m^2 the number of stable equilibriums increases to two (indicated by the green diamonds). The black dash-dotted line corresponds to the equilibrium configuration found in Fig. 2.6b. Finally, there are only unstable equilibriums (red diamonds) for val-

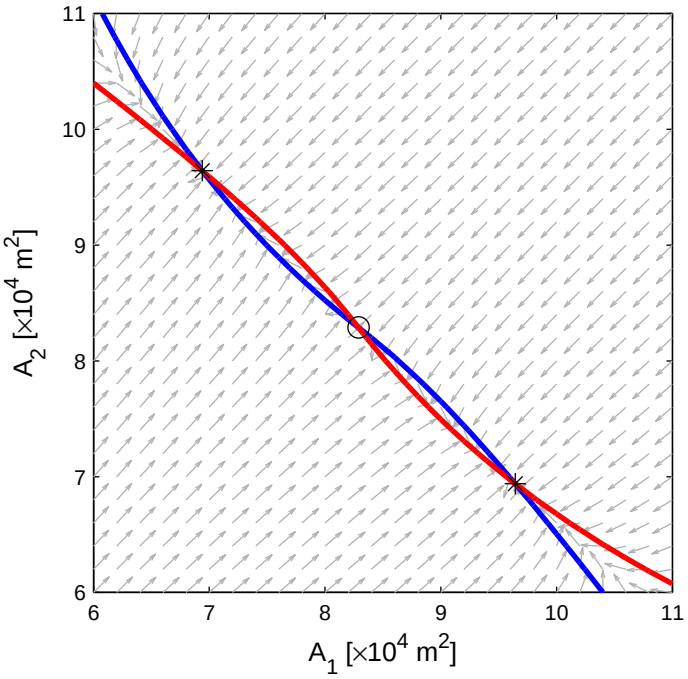

Figure 2.7: Close-up around the multiple stable equilibriums in Fig. 2.6b. The blue and red line correspond to the equilibrium flow curve of Inlet 1 and Inlet 2, respectively. The grey arrows indicate the system's tendency. The black circles indicate unstable and the black asterisks indicate stable equilibriums.

ues of A_3 larger than 68×10^3 m^2. This situation is exemplified by Fig. 2.6c, which corresponds with the black dashed line in Fig. 2.8.

The transition from the situation with two stable equilibriums to the one without a stable equilibriums involves the merger of a stable and an unstable equilibrium. The value of A_3 associated with this merger is referred to as limit point (LP).

In conclusion, for symmetrical forcing the number of stable equilibriums for a double inlet system with topographic high depends on the size of the wetted cross-sectional area of the topographic high.

2.4.2 Amplitude differences only

To investigate the influence of amplitude differences between the forcing off both inlets, $\Delta Z = Z_1 - Z_2$, on the number and stability of equilibriums, Fig. 2.8 has been constructed for amplitude differences ranging between -0.10 m and 0.10 m. The result is displayed in Fig. 2.9. In the calculations, Z_2 is kept fixed at 0.80 m, while Z_1 is varied. Other parameter values can be found in Table 2.1.

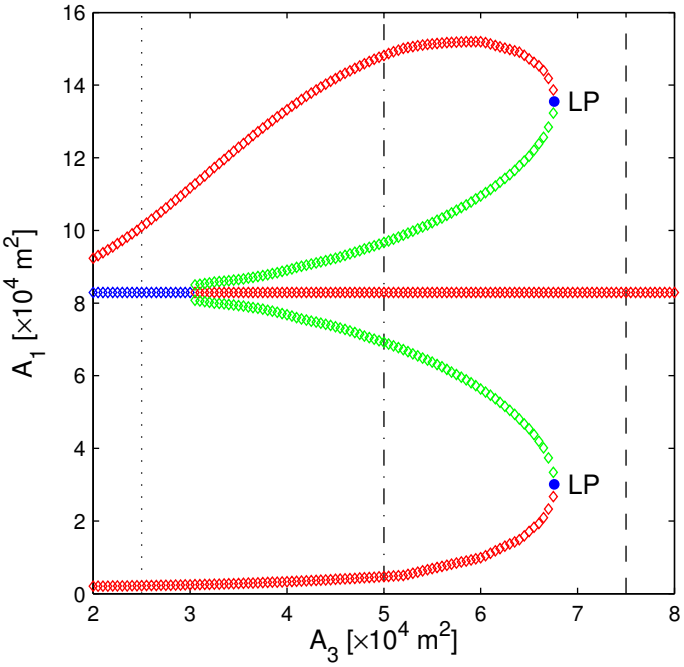

Figure 2.8: Number of equilibrium cross-sectional areas of Inlet 1 and their stability as a function of the cross-sectional area of the topographic high for symmetrical forcing. Red diamonds indicate unstable equilibriums, blue diamonds indicate the presence of one set of stable inlets for a certain A_3 and green diamonds indicate the presence of two sets of stable inlets for a certain A_3. The blue solid circles denote a limit point, LP, in which a stable and unstable equilibrium merge.

Similarly to the previous section the unstable equilibrium close to $(A_1, A_2) = (0, 0)$ found in a typical flow diagram is omitted. Notice, when taking a slice of Fig. 2.9 through $\Delta Z = 0$, one would obtain Fig. 2.8. As Fig. 2.9 shows, the number of stable equilibriums and their stability is, besides the size of the topographic high, clearly sensitive to the amplitude difference between the forcing off both inlets.

To enhance the visualisation of Fig. 2.9, sections have been made at $A_3 = 25 \times 10^3$ m^2 (solid black line), $A_3 = 50 \times 10^3$ m^2 (dash-dotted black line) and $A_3 = 75 \times 10^3$ m^2 (dashed black line). These sections correspond to Figs. 2.10a, 2.10b and 2.10c, respectively (see also Fig. 2.6). It follows from Fig.2.10a that for the smallest value of the opening over the topographic high (corresponding to two separate sub-basins), amplitude differences do not affect the number, nor the stability of the equilibriums. The size of the stable cross-sectional area of Inlet 1 generally increases for increasingly larger forcing amplitude off that inlet compared to that off Inlet 2 and vice versa. For the intermediate opening, Fig. 2.10b, the number of sets of stable inlets are sensitive to amplitude differences. In particular, for relatively small values of ΔZ, in this case between

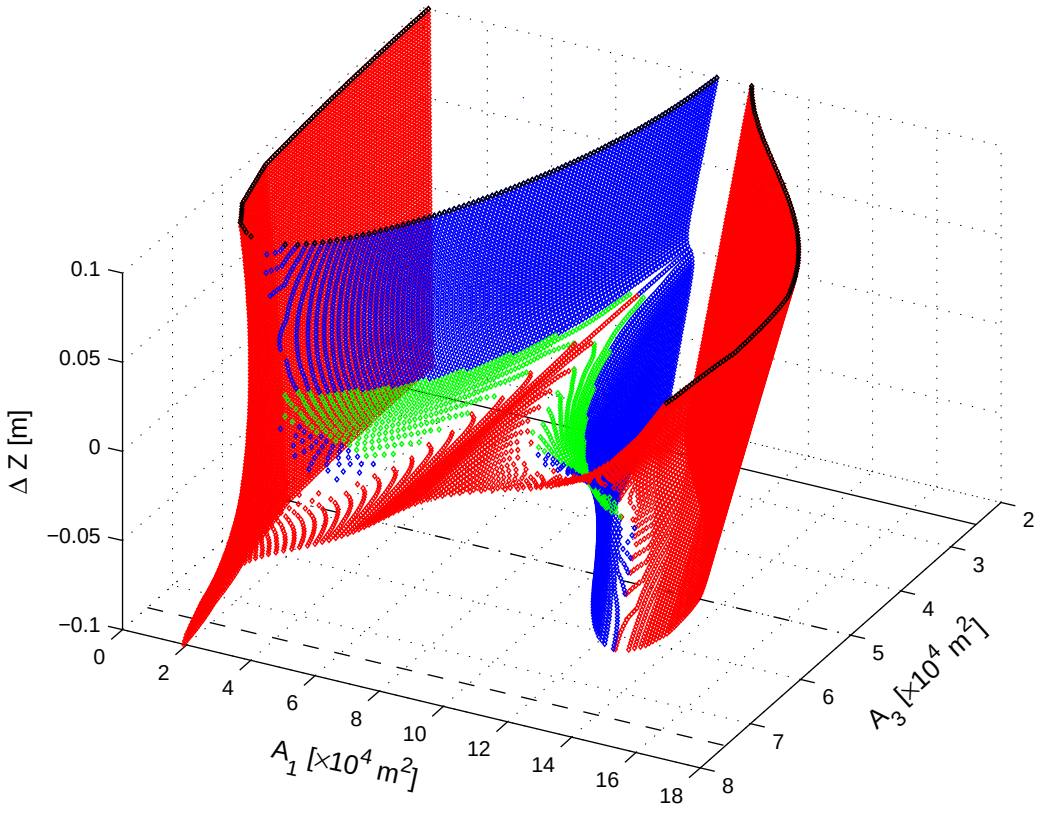

Figure 2.9: Three-dimensional visualisation of the number of equilibriums and their stability, expressed in terms of A_1, as a function of cross-sectional area of the topographic high, A_3, and the amplitude difference between the inlet forcings, ΔZ. Red diamonds indicate unstable equilibriums, blue diamonds indicate the presence of one set of stable inlets and green diamonds indicate the presence of two sets of stable inlets for a certain A_3-value. The black diamonds indicate the edge of the amplitude difference range at $\Delta Z = 0.10$ m. The black solid, dash-dotted and dashed cross-sections correspond to Figs. 2.10a, 2.10b and 2.10c, respectively.

-0.005 and 0.005 m, two sets of stable inlets exist (indicated by the green diamonds). For amplitude difference outside this range, the number of sets of stable inlets reduces to one (indicated by the blue diamonds). The maximum range $\Delta Z = [-0.014\,\text{m}, 0.014\,\text{m}]$ was found in Fig. 2.9 at $A_3 \approx 65 \times 10^3$ m^2. Finally, Fig. 2.10c indicates that regardless of the amplitude difference, only unstable equilibriums exist for the parameter space investigated here.

To conclude, the results above suggest that the number of sets of stable inlets are only sensitive to amplitude differences for intermediate openings. However, the size of the sets of stable inlets reacts to any change in amplitude difference.

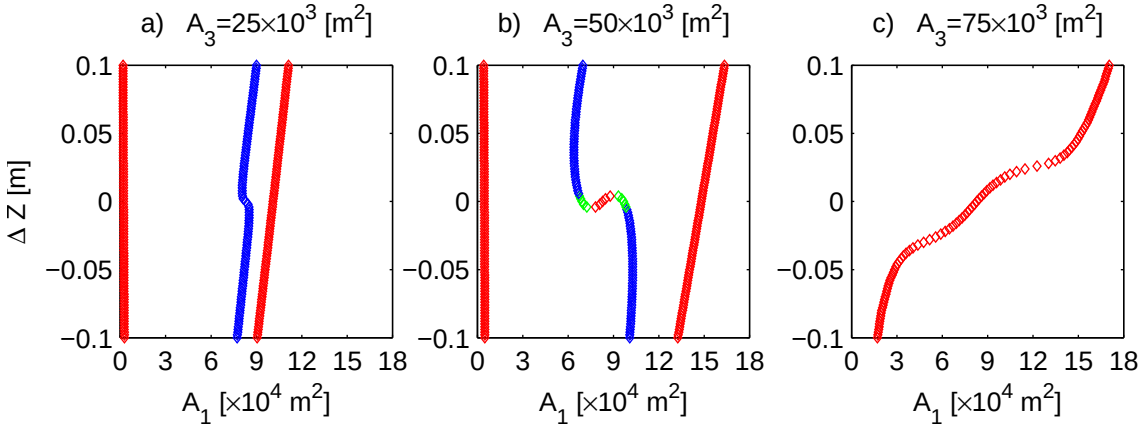

Figure 2.10: Cross-sections corresponding to the black solid, dash-dotted and dashed line in Fig. 2.9 for (a) $A_3 = 25 \times 10^3$ m^2, (b) $A_3 = 50 \times 10^3$ m^2, and (c) $A_3 = 75 \times 10^3$ m^2. For reference of the coloured diamonds, see Fig. 2.9.

2.4.3 Phase differences only

Similarly to the previous section, the number of sets of stable inlets is investigated for phase difference only, $\Delta\theta = \theta_1 - \theta_2$, between the forcing off the two inlets. Figs. 2.11 and 2.12 are similarly constructed as Figs. 2.9 and 2.10, respectively. In these figures the value of θ_2 is kept fixed at zero and θ_1 varies between -0.8 and 0.8 rad.

The effect of phase difference on the number of sets of stable inlets is similar to that of amplitude differences. Like amplitude differences, phase differences only influence the number of sets of stable inlets for intermediate sizes of the opening over the topographic high. For the case displayed in Fig. 2.12b multiple stable equilibriums (indicated by the green diamonds) exist for a range of $\Delta\theta$ between approximately -0.2 and 0.2 rad. The maximum range $\Delta\theta = [-0.55 \text{ rad}, 0.55 \text{ rad}]$, where two sets of stable inlets exist for a certain value of A_3, was found in Fig. 2.11 at $A_3 \approx 65 \times 10^3$ m^2. For small openings over the topographic high one set of stable inlets exists (indicated by the blue diamonds). This number is not affected by phase differences. This also holds for large openings over the topographic high where no set of stable inlets exists.

To sum up, phase difference affect the number of sets of stable inlets in a similar manner as amplitude differences: only at intermediate sizes of the opening over the topographic high do they have a significant influence.

2.5 Discussion

For double inlet systems that include a topographic high and are forced by the same prescribed sea surface elevation off the inlets, results of numerical com-

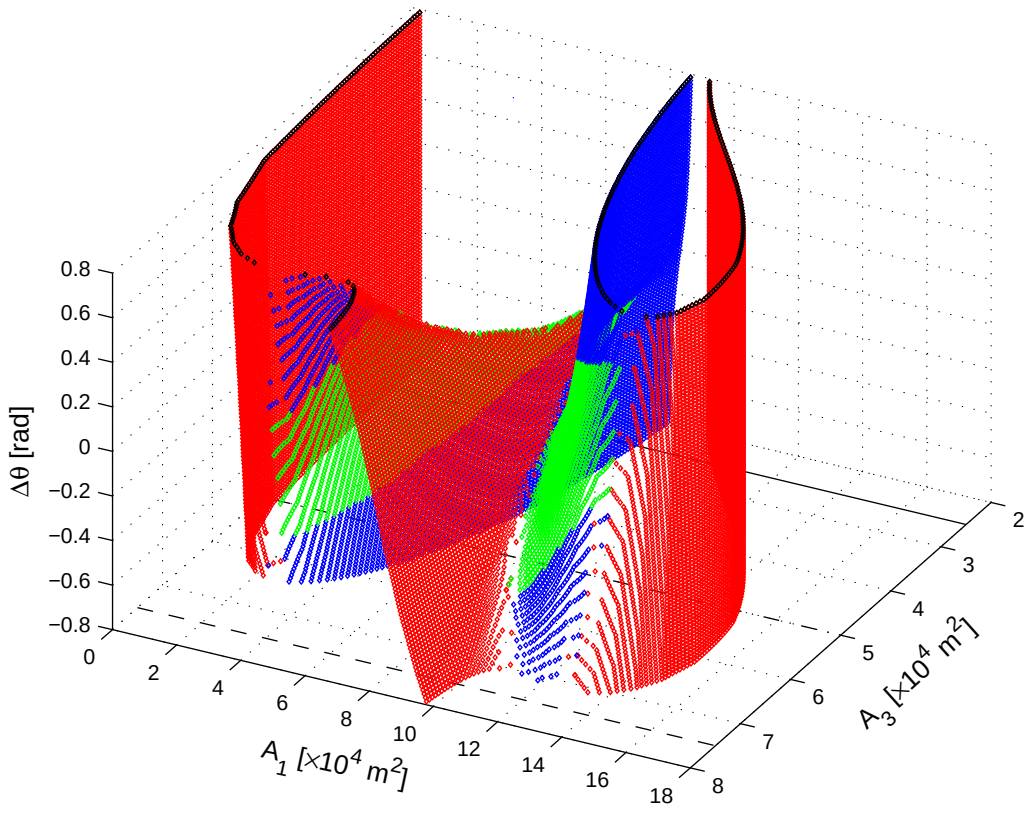

Figure 2.11: Three-dimensional visualisation of the number of sets of stable inlets, expressed in terms of A_1, as a function of the opening over the topographic high, A_3, and the phase difference between the forcing off the inlets, $\Delta\theta$. Red diamonds indicate the presence of sets of unstable inlets, blue diamonds indicate the presence of one set of stable inlets and green diamonds indicate the presence of two sets of stable inlets. The black diamonds indicate the edge of the amplitude difference range at $\Delta\theta = 0.8$ rad. The black solid, dash-dotted and dashed cross-sections correspond to Figs. 2.10a, 2.10b and 2.10c, respectively.

putations suggest that there can be more than two equilibriums some of which are stable. The exact number of equilibriums and their stability, in addition to the length and friction factor of the inlet channels, strongly depends on the wetted cross-sectional area over the topographic high. For a relatively small cross-sectional area, the inlet-bay system behaves as two separate single inlet systems. In that case the two sub-basins act independently and the equilibrium flow curve for each inlet degenerates to two parallel lines. There are four equilibriums only one of which is stable. This result is similar to a two-dimensional representation of the closure curves for single inlet systems introduced by Escoffier (1940) and further investigated and applied to specific sites by O'Brien & Dean (1972);

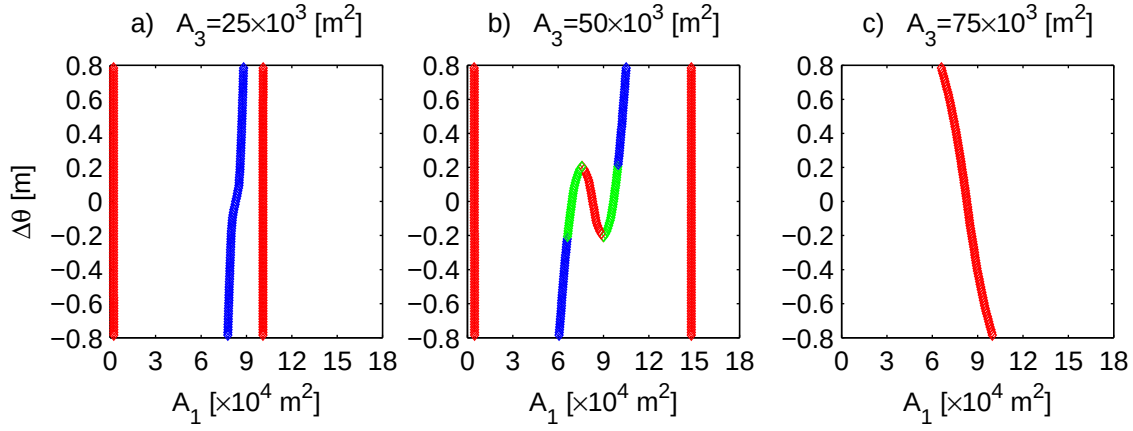

Figure 2.12: Cross-sections corresponding to the black solid, dash-dotted and dashed line in Fig. 2.11 for (a) $A_3 = 25 \times 10^3$ m^2, (b) $A_3 = 50 \times 10^3$ m^2, and (c) $A_3 = 75 \times 10^3$ m^2. For reference of the coloured diamonds, see Fig. 2.11.

van de Kreeke (1998, 2004). For a large wetted cross-sectional area the inlet bay system approaches that of the double inlet system without a topographic high. There are at best two equilibriums that both are unstable. This result is in line with earlier conclusions by van de Kreeke (1985, 1990a,b), who studied the stability of a double inlet system without a topographic high. For the intermediate wetted cross-sectional areas the results become more complex. Depending on the length, bottom friction factor and shape factor of the inlet channels, there can be as many as six equilibriums, two of which are stable. The exact causes and conditions that determine the number of stable equilibriums in the case of an intermediate size wetted cross-section are not clear and are the subject of an ongoing study.

As often seen in nature, however, the tides off the various inlets along a barrier coast display differences in amplitude as well as in phase. The numerical experiments in this chapter suggest that amplitude or phase differences influence the equilibrium configuration depending on the size of the topographic high. For large wetted cross-sectional areas they have no influence: there are still no stable equilibriums where both inlets are open. Similarly, for small wetted cross-sectional areas they do not alter the equilibrium configuration and one stable equilibrium exists. The equilibrium cross-sectional area associated with the previous two cases, however, does change depending on the amplitude or phase difference. In the case of intermediate wetted cross-sectional areas, either one or two stable equilibriums exist. Generally, for relatively small amplitude or phase differences two stable equilibriums exist and they reduce to one for relatively large differences. Unfortunately, exact conditions related to the *critical* amplitude or phase difference that indicates the transition between one and two stable equilibriums have not yet been derived and are beyond the scope of this

chapter.

In general, it follows that topographic highs can play an important role in the stability of double inlet systems. A particularly important aspect is that the water level in the sub-basins, rather than the basin as a whole, fluctuates uniformly. Escoffier (1977) already pointed out that the assumption of the basin surface elevation remaining horizontal throughout the tidal cycle is not satisfactory. Based on observations of seemingly stable multiple inlet systems he further hypothesised that spatial variations in the basin could play an important role. This was also recognized by Tambroni & Seminara (2006) in their study on the stability of the three inlets connecting the Venice Lagoon to the Adriatic Sea. However, they then proceed in evaluating the stability of the inlets and associated sub-basins separately, essentially eliminating the effects of the topographic highs on the stability of the inlets.

A limitation of the modelling approach taken in this chapter is that the forcing off the inlets has a fixed nature, i.e. they are not influenced by the water motion in the basin nor by interactions between the inlets through the ocean. In reality, however, these mechanism modify the surface elevation off the inlets and therefore the forcing of the double inlet system. The influence of a dynamical forcing on the cross-sectional stability of double inlet systems will be discussed in more detail in Chapter 4.

2.6 Conclusions

The equilibrium configurations and stability properties of double inlet systems with a topographic high in the basin are investigated using the results of numerical experiments. In addition, the sensitivity of the number and stability of equilibrium cross-sections is investigated with respect to amplitude or phase differences between the forcing off the two inlets.

The suggestion in the Introduction of this chapter that a topographic high dividing the basin in two sub-basins plays a role in the stability of the inlets is confirmed by the numerical experiments. In the presence of a topographic high the water level in the sub-basins, rather than in the basin as a whole, fluctuates uniformly.

For a small cross-sectional area of the topographic high the system is reduced to two separate single inlet systems. There are four equilibriums, one of which is stable with two inlets open. Amplitude or phase differences do not affect the number nor the stability of the equilibriums within the investigated parameter space.

For a large cross-sectional area the system approaches a double inlet system without a topographic high. Assuming entrance/exit losses can be neglected, at best there are two equilibriums neither of which is stable. Similar to small cross-sectional areas amplitude or phase differences do not affect the stability

configuration.

In the transition region between small and large cross-sectional areas of the topographic high as many as six equilibriums can exist. The number of stable equilibriums is sensitive to the amplitude or phase difference between the forcing off the two inlets. For relatively small amplitude or phase differences, two stable equilibriums are present with two inlets open. It was found in this chapter that, for the parameter space investigated, the maximum amplitude and phase range where two stable equilibriums are present, is $\Delta Z \approx [-0.014\ \text{m}, 0.014\ \text{m}]$ and $\Delta\theta \approx [-0.55\ \text{rad}, 0.55\ \text{rad}]$, respectively. The exact range depends, amongst others, on the size of the topographic high. Outside those ranges the number of stable equilibriums with two inlets open is reduced to one.

2.A Solution method double inlet system with topographic high

To solve the non-linear system of equations (2.11)-(2.13) introduced in section 2.3, use is made of the Newton-Raphson method. As a first step, the system of equations is written in matrix notation. For convenience, the governing equations (2.11)-(2.13) are rearranged and repeated here. Continuity gives:

$$B_k \frac{d\zeta_{b_k}}{dt} = A_k u_k + (-1)^k A_3 u_3, \qquad k = 1, 2, \tag{2.A.1}$$

and momentum conservation gives:

$$\frac{R_k}{F_k}\frac{du_k}{dt} + |u_k|u_k = \Gamma_k \left(\zeta_k - \zeta_{b_k}\right), \qquad k = 1, 2, \tag{2.A.2}$$

$$\frac{R_3}{F_3}\frac{du_3}{dt} + |u_3|u_3 = \Gamma_3 \left(\zeta_{b_1} - \zeta_{b_2}\right), \tag{2.A.3}$$

where $R_k = \gamma\sqrt{A_k}$ $(k = 1, 2)$, $R_3 = A_3/W_{\text{th}}$ and

$$\begin{cases} \Gamma_k &= \dfrac{gR_k}{F_k L_k}, \qquad k = 1, 2, \\ \Gamma_3 &= \dfrac{gA_3}{F_3 L_3 W_{\text{th}}}. \end{cases} \tag{2.A.4}$$

An explanation of the symbols throughout this appendix is given in section 2.3. The external forcing is defined as

$$\zeta_k = \Re\left\{\hat{\zeta}_k e^{i\omega t}\right\}, \text{with} \quad \hat{\zeta}_k = Z_k e^{i\theta_k} \quad \text{and} \quad k = 1, 2, \tag{2.A.5}$$

where $\hat{\zeta}_k$ is the complex amplitude of the water elevation. Consequently, approximate periodic solutions are sought, whereby a trial solution is assumed of the form

$$u_k = \Re\left\{\hat{u}_k e^{i\omega t}\right\}, \qquad k = 1, 2, 3, \tag{2.A.6}$$

where $\hat{u}_k$ is the complex amplitude of the inlet velocities and the velocity over the topographic high. The Galerkin technique (see e.g. Boyd, 2001) is used to

make an estimation of the amplitudes that correspond to the trial solution (2.A.6). Substitution of Eq. (2.A.6) into the continuity equation yields

$$\hat{\zeta}_{b_k} = \frac{1}{i\omega}\left(\frac{A_k}{B_k}\hat{u}_k + (-1)^k \frac{A_3}{B_k}\hat{u}_3\right). \tag{2.A.7}$$

Combining (2.A.5)-(2.A.7) with momentum conservation (2.A.2) and (2.A.3) yields for the tidal inlets

$$\left(-\beta_k + i|u_k|\right)\hat{u}_k + (-1)^k \eta_k \hat{u}_3 = i\Gamma_k \hat{\zeta}_k, \tag{2.A.8}$$

and for the topographic high

$$-\tau_1 \hat{u}_1 + \tau_2 \hat{u}_2 + \beta_3 \hat{u}_3 + i|u_3|\hat{u}_3 = 0, \tag{2.A.9}$$

Here,

$$\begin{cases} \beta_k &= \omega\dfrac{R_k}{F_k} - \dfrac{1}{\omega}\Gamma_k\dfrac{A_k}{B_k}, \qquad k = 1,2, \\ \beta_3 &= \omega\dfrac{R_3}{F_3} - \dfrac{1}{\omega}\Gamma_3\left(\dfrac{A_3}{B_1} + \dfrac{A_3}{B_2}\right), \end{cases} \tag{2.A.10}$$

and

$$\eta_k = \frac{1}{\omega}\Gamma_k\frac{A_3}{B_k}, \tag{2.A.11}$$

$$\tau_k = \frac{1}{\omega}\Gamma_3\frac{A_k}{B_k} \tag{2.A.12}$$

Separating Eqs. (2.A.8) and (2.A.9) into real and imaginary parts and defining $\hat{\zeta}_k = \zeta_{c,k} + i\zeta_{s,k}$ and $\hat{u}_k = u_{c,k} + iu_{s,k}$ yields for the inlets

$$\begin{cases} \Re: -\beta_k u_{c,k} - |u_k|u_{s,k} + (-1)^k \eta_k u_{c,3} &= -\Gamma_k \zeta_{s,k}, \\ \Im: -\beta_k u_{s,k} + |u_k|u_{c,k} + (-1)^k \eta_k u_{s,3} &= \Gamma_k \zeta_{c,k}, \end{cases} \tag{2.A.13}$$

and for the topographic high

$$\begin{cases} \Re: -\tau_1 u_{c,1} + \tau_2 u_{c,2} - \beta_3 u_{c,3} - |u_3|u_{s,3} &= 0, \\ \Im: -\tau_1 u_{s,1} + \tau_2 u_{s,2} - \beta_3 u_{s,3} + |u_3|u_{c,3} &= 0. \end{cases} \tag{2.A.14}$$

In these equations $|u_k| = \frac{2}{\pi}\sqrt{u_{c,k}^2 + u_{s,k}^2}$, in accordance with the Galerkin method. For convenience, the system above is written in matrix notation

$$\begin{bmatrix} |u_1| & -\beta_1 & 0 & 0 & 0 & -\eta_1 \\ -\beta_1 & -|u_1| & 0 & 0 & -\eta_1 & 0 \\ 0 & 0 & |u_2| & -\beta_2 & 0 & -\eta_2 \\ 0 & 0 & -\beta_2 & -|u_2| & -\eta_2 & 0 \\ 0 & -\tau_1 & 0 & \tau_2 & |u_3| & -\beta_3 \\ -\tau_1 & 0 & \tau_2 & 0 & -\beta_3 & -|u_3| \end{bmatrix} \begin{bmatrix} u_{c,1} \\ u_{s,1} \\ u_{c,2} \\ u_{s,2} \\ u_{c,3} \\ u_{s,3} \end{bmatrix} = \begin{bmatrix} \Gamma_1\zeta_{c,1} \\ -\Gamma_1\zeta_{s,1} \\ \Gamma_2\zeta_{c,2} \\ -\Gamma_2\zeta_{s,2} \\ 0 \\ 0 \end{bmatrix}, \tag{2.A.15}$$

or in short form

$$\mathbf{M} \cdot \underline{x} = \underline{b} \tag{2.A.16}$$

This system can be solved numerically using the Newton-Raphson method (see e.g. Abramowitz & Stegun, 1972), which holds the following. Eq. (2.A.16) can be written as

$$\underline{f}(\underline{x}) = \underline{b}. \tag{2.A.17}$$

Defining a new function $\underline{g}(\underline{x})$,

$$\underline{g}(\underline{x}) = \underline{f}(\underline{x}) - \underline{b} = 0, \tag{2.A.18}$$

a solution $\underline{x}^*$ is sought for the above equations $\underline{g}$. With the Newton-Raphson method $\underline{g}$ is approximated with a first order Taylor polynomial, according to

$$\underline{g}(\underline{x}^* + \Delta\underline{x}) = \underline{g}(\underline{x}^*) + \sum_{j=1}^{n} \Delta x_j \left.\frac{\partial g_j(\underline{x})}{\partial x_j}\right|_{\underline{x}^*}, \tag{2.A.19}$$

where $n = 6$ for this particular case. Assume that $\underline{x} + \Delta\underline{x} = \underline{x}^*$. In that case

$$\underline{g}(\underline{x}) + \sum_{j=1}^{n} \Delta x_j \left.\frac{\partial g_j(\underline{x})}{\partial x_j}\right|_{\underline{x}^*} = 0, \tag{2.A.20}$$

or

$$\sum_{j=1}^{n} \Delta x_j \left.\frac{\partial g_j(\underline{x})}{\partial x_j}\right|_{\underline{x}^*} = -\underline{g}(\underline{x}^*). \tag{2.A.21}$$

This latter system is linear in $\Delta\underline{x}$. In short matrix notation this can be written as $\mathbf{Y}\cdot\Delta\underline{x} = -\underline{g}(\underline{x}^*)$, or

$$\begin{bmatrix} \frac{\partial g_1}{\partial x_1}\Big|_{\underline{x}^*} & \cdots & \frac{\partial g_1}{\partial x_n}\Big|_{\underline{x}^*} \\ \vdots & \ddots & \vdots \\ \frac{\partial g_n}{\partial x_1}\Big|_{\underline{x}^*} & \cdots & \frac{\partial g_n}{\partial x_n}\Big|_{\underline{x}^*} \end{bmatrix} \begin{bmatrix} \Delta x_1 \\ \vdots \\ \Delta x_n \end{bmatrix} = - \begin{bmatrix} g_1(\underline{x}^*) \\ \vdots \\ g_n(\underline{x}^*) \end{bmatrix}. \tag{2.A.22}$$

From this the $\Delta\underline{x}$ can be determined. Consequently, they are used to obtain the $\underline{x}^*$ via iteration. An approximated $\underline{x}$ is adjusted to a new (better) approximation $\underline{x} + \Delta\underline{x} = \underline{x}^*$, using $\Delta\underline{x}$ derived from matrix (2.A.22). It turns out that with a reasonable first estimate of $\underline{x}$ this method converges relatively fast. From the converged solution $\underline{x}$ the amplitude of the inlet velocities can be calculated according to $U_k = \sqrt{u_{c,k}^2 + u_{s_k}^2}$. In turn, U_k is used to construct the flow diagram from which the cross-sectional stability can be assessed.

3

Entrance/exit losses and cross-sectional inlet stability*

Abstract In this chapter the effect of entrance/exit losses on the cross-sectional stability of double inlet systems is investigated. The inlet is in equilibrium when the sand transport into the inlet equals the sand transport out of the inlet. The velocity amplitude corresponding with the equilibrium cross-sectional area is referred to as the equilibrium velocity ($\sim$1 m s^{-1}). This equilibrium is stable when after a perturbation the cross-sections of both inlets return to their original equilibrium values. The amplitudes of the inlet velocities are obtained using a lumped-parameter model in which the basin water level fluctuates uniformly (pumping mode) and where the inlets are schematised to prismatic channels. The system is forced by a semi-diurnal tide, where amplitude and phase may differ between the two inlets. Previous studies concluded that for double inlet systems no stable equilibriums can be found. However, in these studies entrance/exit losses were neglected. In the present study entrance/exit losses are included in the dynamic equation of the inlets.

Using an analytical model it is shown that entrance/exit losses and a difference in the two ocean tidal amplitudes are a prerequisite for the existence of stable equilibriums. Furthermore, the effects of the addition of bottom friction and inertia to the dynamic equation are investigated using a mathematical *continu-*

*This chapter has appeared as *"Entrance/exit losses and cross-sectional stability of double inlet systems"* by R.L. Brouwer, J. van de Kreeke and H.M. Schuttelaars (2012), Est. Coast. Shelf Sci. 107, pp. 69-80.

ation method. The results show that, provided entrance/exit losses are considerably larger than bottom friction and inertia, stable equilibriums are possible. These conclusions are supported by observations in the Ria Formosa, southern Portugal. Care should be taken in using the stability model described in this paper as a predictive tool due to simplifications in the model and the uncertainty in determining certain parameter values including inlet length, entrance/exit loss coefficient, bottom friction factor and equilibrium velocity. To alleviate these shortcomings suggestions are made for future research.

3.1 Introduction

Barrier island coasts are highly dynamical systems that serve as a first defence for the hinterlying mainland. Examples are the Wadden Sea coast of the Netherlands, Germany and Denmark (Ehlers, 1988), the U.S. part of the Gulf of Mexico, the U.S. East Coast and Ria Formosa in Southern Portugal. These barrier island coasts are a concatenation of tidal inlet systems, in which a tidal basin or back-barrier area is connected to the ocean or sea by one or more tidal inlets.

Tidal inlet systems in sandy environments consist of different elements including ebb tidal delta, inlet channel and basin. Restricting attention to inlets where river flow has a minor impact, the dimensions of the various elements are a result of primarily tide and waves. The interest here is in the equilibrium and stability of the cross-sectional area of the inlet channel; the channel connecting ocean and basin. Referring to Escoffier (1940) the cross-sectional area of a tidal inlet takes on a value such that the wave-driven sediment import equals the tide-driven sediment export. The velocity amplitude corresponding with the equilibrium cross-sectional area is referred to as the equilibrium velocity. Based on observations Escoffier suggested an approximate value of 1 m s^{-1}, the exact value depending somewhat on the volume of littoral drift. The actual cross-sectional area oscillates around this equilibrium value. By opening a new inlet or as a result of land reclamation the deviation from the equilibrium value can become so large that the cross-sectional stability is challenged and one of the inlets may close. It is therefore of importance to assess if and under what conditions stable equilibrium configurations of multiple tidal inlet systems are expected to exist.

As a first step to investigate multiple tidal inlet stability, van de Kreeke (1985, 1990a) studied the stability of a double inlet system. He used a L-P model to describe the hydrodynamics of the system. Similar to Keulegan (1951), van de Kreeke simplified the dynamic equation of the L-P model by only retaining the quadratic bottom friction and pressure gradient while neglecting inertia and entrance/exit losses. The double inlet system was assumed to be in equilibrium if the velocity amplitude in the inlets equals the equilibrium velocity taken as 1 m s^{-1}. The forcing off the two inlets consisted of a simple harmonic tide with

equal amplitude and phase. The main conclusion was that for these conditions no stable equilibrium(s) exist, i.e. ultimately one of the inlets would close. Furthermore, he suggested that a similar conclusion holds for multiple inlet systems.

Several observations, however, have shown that multiple inlet systems are potentially stable for over several centuries. Examples are Gasparilla Sound in western Florida (Escoffier, 1977), the Dutch Wadden Sea (Louters & Gerritsen, 1994) and Ría Formosa in southern Portugal (Salles et al., 2005; Pacheco et al., 2010, 2011a). These observations suggest that the assumptions of the hydrodynamic model used by van de Kreeke (1985, 1990a) might be too restrictive and do not take into account important (non-linear) processes, such as tidal distortion in the basin (e.g. Boon & Byrne, 1981). To overcome these restrictions, one approach is to use state of the art process-based models describing the complex flow field (e.g. Salles et al., 2005; Dias & Sousa, 2009) and resulting sediment transport and bottom changes (e.g Dastgheib et al., 2008). As discussed in the introduction of this thesis, one of the drawbacks of these models is that due to their complexity it is difficult to determine cause and effect. Consequently, insight into the physical mechanisms responsible for the existence of stable tidal inlet systems with more than one inlet open is difficult to ascertain.

Another approach is to parameterise the important processes into the L-P model. An advantage of this approach is that it facilitates analytical solution methods to determine which underlying mechanisms are important for the stability of tidal inlet systems. Support for the use of this type of model has been provided by Herman (2007), who compared the results of a 2D finite difference hydrodynamic model and a L-P model. The results show that the L-P model captures the important dynamics of the inlet flow.

In this chapter, the latter L-P model is used to investigate recent observations in the multiple inlet system of Ría Formosa (Pacheco et al., 2010, 2011a), which has persisted on a historical time scale (see also Section 1.3 on page 4). In particular the sub-system consisting of the two inlets Faro and Armona and connecting a single basin to the ocean can be considered in stable equilibrium. A characteristic for this double inlet system is that the inlets are relatively short and therefore entrance/exit losses are not necessarily small compared to bottom friction losses. This loss-term was neglected in the study by van de Kreeke (1990a). The objective of this chapter is to investigate the role of the different terms in the L-P model on cross-sectional stability of double inlet systems with special reference to the entrance/exit loss term.

This chapter is organised as follows. In Section 3.2, the governing equations of a double inlet system are presented. In addition, a new visualisation method to analyse the influence of the different terms in the dynamic equation on the equilibrium and stability of double inlet systems is introduced. Section 3.3 contains the derivation of the necessary conditions for stable double inlet systems to exist when only entrance/exit losses balance the pressure gradient over the inlets. Subsequently, in Section 3.4 the addition of bottom friction and inertia

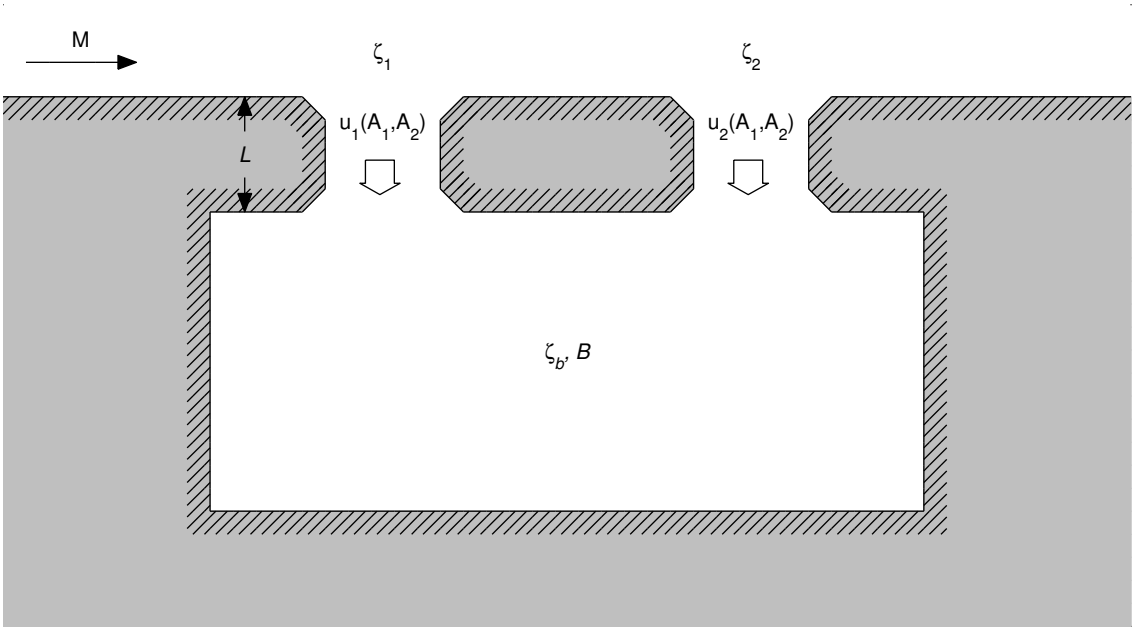

Figure 3.1: Schematisation of a double inlet system draining a single basin. For an explanation of the symbols, see Subsection 3.2.1.

on the equilibrium and stability is investigated. In Section 3.5, the effect of forcing on stable equilibriums is looked into. The results and insights obtained from the previous section are then applied to the Faro-Armona double inlet system in Section 3.6. Finally, Sections 3.7 and 3.8 present the discussion and conclusions, respectively.

3.2 Governing equations and method

3.2.1 Governing Equations

In this chapter the double inlet system is schematised to a single basin connected to the sea or ocean by two tidal inlets (Fig. 3.1). The basin is relatively small and deep and the tidal inlets are prismatic channels with diverging sections on either end. The focus is on cross-sectional stability. Following Escoffier (1940) an inlet is in equilibrium if the amplitude of the inlet velocity equals the so-called equilibrium velocity U_{eq}. Escoffier suggested this velocity to be of the order of

1 m s^{-1}. The equilibrium is stable when after a perturbation of the equilibrium, the cross-sectional areas return to their original equilibrium values.

For inlets that are in equilibrium and assuming average weather conditions (as opposed to storm conditions) there is a balance between the volume of sediment entering and leaving the inlet. The volume entering the inlet is taken as a constant fraction of the littoral drift and the volume leaving the inlet is taken proportional to a power of the ebb tidal velocity amplitude (van de Kreeke, 1998). The sediment is uniformly distributed over the inlet length and sediment exchange between inlet and basin is assumed to be negligible. Under these assumptions, the rate of change of the cross-sectional area can be written as (van de Kreeke, 1998)

$$\frac{dA_k}{dt} = \frac{M}{L}\left[\left(\frac{U_k}{U_{eq}}\right)^n - 1\right], \qquad k = 1, 2. \tag{3.1}$$

Here, A_k is the cross-sectional area of inlet k (m^2); t is time (s); L is the inlet length (m); M is a constant fraction of the littoral drift (m^3 s^{-1}); U_k is the cross-sectionally averaged velocity amplitude in inlet k (m s^{-1}), calculated using the L-P model; U_{eq} is the equilibrium velocity (m s^{-1}). If the inlet velocity U_k equals U_{eq}, $dA_k/dt = 0$. This implies that the inlet system is in equilibrium. n is a power whose value depends on the adopted sand transport law. Values of n range between 3 and 6 (van Rijn, 1993). The value of n influences the direction of the unit vectors in the flow diagram, Fig. 3.2 (see also Section 2.2 on page 24). The direction of these vectors in the neighbourhood of the equilibrium determines whether the equilibrium is stable or unstable. However, linearising Eq. (3.1) it can be shown that in the neighbourhood of the equilibrium the direction of these unit vectors become independent of n. Therefore, the value of n does not play a role in the stability of the equilibrium. In the calculations n was somewhat arbitrarily given a value of 3.

The response of the inlet cross-sectional area and the equilibrium state is governed by the amplitude of the inlet velocities U_k. These velocities are calculated using a L-P model. In this model the dynamics of the flow in the diverging sections is governed by the advective acceleration and the longitudinal pressure gradient (see Vennell, 2006, for support of this governing balance by ADCP measurements in a tidal inlet connecting Tauranga Harbour to the Pacific Ocean, New Zealand). Energy losses in these sections are taken as a fraction of the velocity head. The dynamics of the flow in the prismatic section constitutes a balance between longitudinal pressure gradient, inertia and bottom friction. The resulting equation is

$$\frac{L}{g}\frac{du_k}{dt} + \frac{8}{3\pi}\left(\frac{m}{2g} + \frac{FL}{gR_k}\right)U_k u_k = \zeta_k - \zeta_b, \qquad k = 1, 2. \tag{3.2}$$

Here $g \approx 9.81$ m s^{-2} the gravitational acceleration; u_k denotes the cross-sectionally averaged velocity in inlet k (m s^{-1}); m the entrance/exit loss coefficient (-); F the dimensionless bottom friction factor (-); R_k the hydraulic radius of inlet k (m); ζ_k the sea surface elevation off inlet k (m); and ζ_b the basin surface level elevation (m) (where $\zeta_b = 0$ corresponds to mean sea level). The quadratic term $|u_k|u_k$ in Eq. (3.2) is linearised and replaced by $(8/(3\pi))U_k u_k$, with $U_k = U_{eq}$ (see Lorentz, 1926; Zimmerman, 1982). The reason to do so is that this linearisation is necessary for the solution method described in Section 3.2.2. Moreover, the results in the neighbourhood of the equilibrium are not affected by this linearisation.

Because the basin is assumed to be relatively small and deep the water level to a good approximation fluctuates uniformly (pumping mode) and the continuity equation reads

$$B\frac{d\zeta_b}{dt} = A_1 u_1 + A_2 u_2, \tag{3.3}$$

in which B is the basin surface area (m^2).

Eqs. (3.2) and (3.3) constitute a L-P model. For a single inlet system the first order analytical solution for u and ζ_b are functions of two dimensionless parameters involving ζ_0, L, A, F, m and B, hence the designation lumped-parameter (L-P) model. For a detailed derivation of Eqs. (3.2) and (3.3) reference is made to Mehta & Özsoy (1978) and van de Kreeke (1988). Another approach that leads to a similar momentum equation as Eq. (3.2) is presented by Maas (1997).

In most studies the entrance/exit loss coefficient m is assumed to be 1 (e.g. O'Brien & Clark, 1974; Escoffier, 1977; Tambroni & Seminara, 2006). Other studies give a specific range for m: e.g. van de Kreeke (1988) suggests a range between 0.3 and 1.4 and Seabergh (2002) adopts a range of m between 1 and 1.25. Theoretically the value of m cannot be larger than 2. In the literature values of F range between $2 \cdot 10^{-3}$ and $4 \cdot 10^{-3}$. With $m = \mathcal{O}(1)$ and $F = \mathcal{O}(10^{-3})$ it follows that the entrance/exit loss term and bottom friction term in Eq. (3.2) are of the same order for $L/R = 500$. With a typical value $R = 5$ m for tidal inlets, $L = 2500$ m. For values of $L < 2500$ m the entrance/exit loss term is more important than the bottom friction term and for $L > 2500$ m the entrance/exit loss term is less important than the bottom friction term. For $L = 2500$ m and a semi-diurnal tide, with $\omega = 1.4 \cdot 10^{-4}$ s^{-1}, the inertia term is approximately half of the entrance/exit loss term. This suggests that for relatively short tidal inlets, entrance/exit losses cannot be neglected.

In addition, from Eq. (3.1) a time scale for coastal evolution can be deduced. Assuming the term between square brackets on the right-hand side is $\mathcal{O}(1)$, the time scale $T = AL/M$. For relatively short inlets, with $L = \mathcal{O}(10^3)$, $A = \mathcal{O}(10^3)$ and $M = \mathcal{O}(10^5)$, the time scale is in the order of decades. For relatively long inlets, with $L = \mathcal{O}(10^3)$, $A = \mathcal{O}(10^5)$ and $M = \mathcal{O}(10^6)$, the time scale is in the order of centuries. It follows that the time scale for coastal evolution for tidal

inlet systems is in the order from decades to centuries.

To relate the hydraulic radius R_k to the cross-sectional area, the cross-sections are assumed to be geometrically similar for all values of the cross-sectional area (following O'Brien & Dean, 1972). Hence, the ratio of all corresponding lengths for two cross-sections are the same. This allows writing

$$R_k = \gamma\sqrt{A_k}, \tag{3.4}$$

where γ is a shape factor (-), which is assumed to be constant.

The tidal motion in the inlets is forced by a semi-diurnal harmonic constituent, where amplitudes and phases may differ between the two inlets,

$$\zeta_k = \Re\left\{Z_k e^{i[\omega t+\theta_k]}\right\}. \tag{3.5}$$

Here $\Re$ denotes the real part, Z_k is the real-valued amplitude of the ocean tide at inlet k (m) and θ_k the phase of the ocean tide at inlet k (rad). Note that the amplitude and phase of the forcing off the inlets are fixed and not dynamic, i.e. they are not influenced by dynamic interactions with the basin.

3.2.2 Methods

Flow Diagram

To determine the equilibrium cross-sectional areas and their stability use is made of a so-called *flow diagram*. For a detailed description on how to construct such a flow diagram, the reader is referred to Section 2.2 on page 24. An example of a flow diagram, using the parameter values of Table 3.1, is presented in Fig. 3.2. These parameter values pertain to a symmetric double inlet system, i.e. L, F, m and γ for both inlets are the same, resembling the Faro-Armona system, where Inlet 1 refers to Armona and Inlet 2 refers to Faro. The reason a symmetric inlet system is selected is to facilitate a physical explanation for the role of the entrance/exit losses in the cross-sectional stability of a double inlet system. The real Faro-Armona system is not symmetric and a detailed description including parameter values for this system is presented in Section 3.6. In constructing the flow diagram use is made of a numerical solution to Eqs. (3.2)-(3.5). From this, equilibrium velocity curves are constructed for both inlets. The equilibrium velocity curves represent the locus of (A_1, A_2)-values for which $U_1 = U_{eq}$ and $U_2 = U_{eq}$. The intersections of the two curves represent sets of equilibrium cross-sectional areas. To determine the stability of the equilibrium, vectors are added to the flow diagram. These vectors are the unit vectors in the direction of $d\vec{A}/dt$ calculated from Eq. (3.1). The unit vectors indicate the direction in which the values of cross-sectional areas change when they are not in equilibrium. Using this

Table 3.1: Parameter Values for a symmetric double inlet system resembling the Faro-Armona system

Parameter	**Symbol**	**Dimension**	**Value Inlet 1 (Armona)**	**Value Inlet 2 (Faro)**
Inlets				
Inlet cross-section	A_k	m^2	variable	variable
Inlet length	L_k	km	1	1
Entrance/exit coefficient	m_k	-	1	1
Inlet shape factor	γ_k	-	0.2	0.2
Friction factor	F_k	-	2×10^{-3}	2×10^{-3}
Equilibrium velocity	U_{eq}	$m\ s^{-1}$	1	1
Forcing				
Radian frequency	ω^*	s^{-1}	1.4×10^{-4}	
Sea surface amplitude	Z_k	m	1.43	1.36
Sea surface phase	θ_k	rad	0	0
General				
Basin surface area	B^*	m^2	3.4×10^7	
Sediment import	M^*	$m^3\ year^{-1}$	1×10^5	

* pertaining to the entire system

information, the black circles represent unstable equilibriums and the black cross represents a stable one.

Continuation Method

Even though a flow diagram is a useful tool to assess cross-sectional stability, it does not provide direct insight in the effect of individual terms on the dynamic equation and the various parameters, e.g. L, m, F, γ, Z_k and θ_k ($k = 1, 2$), on the presence of equilibriums. To investigate these effects a mathematical *continuation method* (CL_MATCONT; Dhooge et al., 2003) is used.

As an example of the use of this method and the presentation of the results, the influence of the inlet length L on the stable equilibrium in Fig. 3.2 is shown in Fig. 3.3. Starting with a known equilibrium solution (A_1^{eq}, A_2^{eq}), e.g. the stable equilibrium denoted with the black cross in Fig. 3.2, the parameter value L is slightly decreased or increased by CL_MATCONT and a new equilibrium solution is calculated. The continuation method assesses the local stability of this equilibrium by conducting a linear stability analysis. Repeating the procedure, a curve with equilibrium values (A_1^{eq}, A_2^{eq}) as a function of L is found depicted in Fig. 3.3a. For reference the flow diagram of Fig. 3.2 pertaining to $L = 1$ km is added to Fig. 3.3a to show how the cyan curve in this figure is related to the equilibrium velocity curves in the flow diagram. This clearly shows that the unstable branch of the cyan curve passes through the flow diagram at an unstable equilib-

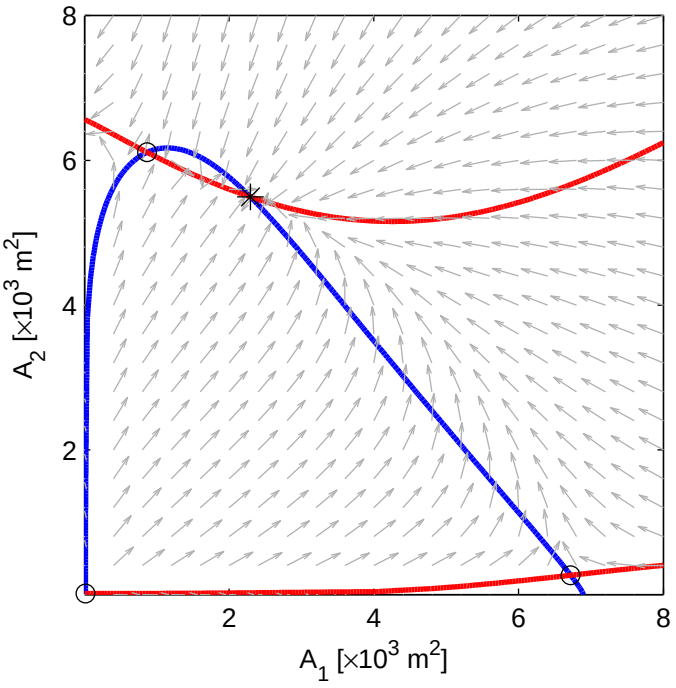

Figure 3.2: Flow diagram with parameters resembling the Faro-Armona system. The blue and red solid line correspond to the equilibrium flow curves of Inlet 1 and 2, respectively, the grey vectors indicate the direction in which the values of the cross-sectional areas change when they are not in equilibrium, the black circles indicate an unstable equilibrium and the black cross indicates a stable equilibrium. Calculations carried out using Eq. (3.2)*;* $m = 1$*,* $\gamma = 0.2$*,* $F = 2 \cdot 10^{-3}$*,* $L = 1\ km$*,* $Z_1 = 1.43\ m$*,* $Z_2 = 1.36\ m$*,* $\theta_k = 0$ *(*$k = 1, 2$*).*

rium (indicated by a black circle) and the stable branch passes through the flow diagram at a stable equilibrium (indicated by a black cross). Inspection with the continuation method of the other two unstable equilibriums found in the flow diagram showed that they remain unstable for the parameter space inspected here. Because the interest is in stable equilibriums, their dependence on L is not shown. The maximum inlet length for which a stable equilibrium exists is found at the point indicated by the black dot denoted as LP. Here, LP stands for Limit Point, which means that the stability of the equilibrium changes from stable to unstable, or vice versa, when crossing this point on the cyan curve. Furthermore, the cyan curve and the black markers are projected on the (A_1, A_2)-plane in grey to help visualize the path of the cyan curve and the location of the markers.

When projecting the curve on the (L, A_k)-plane, with $k = 1, 2$, Fig. 3.3b is obtained. In contrast to Fig. 3.3a, this figure more clearly shows that there is a maximum L for which a stable equilibrium exists.

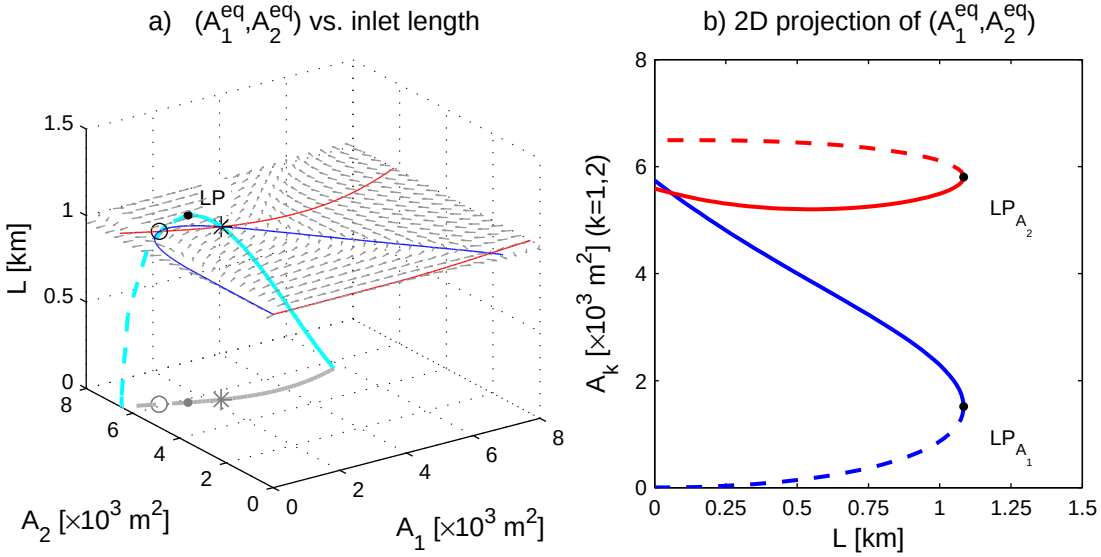

Figure 3.3: Visualizing the influence of parameter variability on the stability of an equilibrium. (a) (A_1^{eq}, A_2^{eq}) for a tidal inlet system resembling the Faro-Armona (in cyan), for varying inlet length L. The dashed, cyan line indicates linearly unstable solutions (unstable saddle) and the solid, cyan line indicates linearly stable solutions (stable node). The cyan curve passes through the flow diagram at the black circle, indicating an unstable equilibrium, and at the black cross, indicating a stable equilibrium. The black dot indicates a limit point, where the cyan curve changes stability. The cyan curve and the black markers are projected on the base plane in grey. (b) Projection of (A_1^{eq}, A_2^{eq}) in (a) on the (L, A_k)-plane $(k = 1, 2)$. The blue line corresponds to Inlet 1 and the red line to Inlet 2. A solid line indicates stable equilibriums and a dashed line unstable ones. Calculations carried out using Eq. (3.2); $m = 1$, $\gamma = 0.2$, $F = 2 \cdot 10^{-3}$, $Z_1 = 1.43\ m$, $Z_2 = 1.36\ m$, $\theta_k = 0$ $(k = 1, 2)$.

3.3 Entrance/exit losses only

3.3.1 Conditions for stable equilibriums

Neglecting inertia and bottom friction in the dynamic equations, Eq. (3.2), and taking $U_k = U_{eq}$, yields

$$cmU_{eq}u_k = \zeta_k - \zeta_b, \qquad \text{with} \quad c = \tfrac{4}{3\pi g}. \tag{3.6}$$

In a strict sense, when replacing U_k with U_{eq} in the linearised quadratic term, Eq. (3.6) is only valid in a neighbourhood of the equilibrium. Solutions to Eq. (3.6) and the continuity equation Eq. (3.3) are presented in Appendix 3.A.1. In this appendix, the forcing condition $\zeta_k = Z_k \exp(i\omega t)$ is used, where only amplitude differences between the inlets are allowed so that an analytical approach is possible. At the end of this section the case of only phase differences between the in-

lets is briefly discussed. Because of its importance in determining cross-sectional stability the solution for U_k is repeated here:

$$U_k = \frac{1}{cmU_{eq}}\sqrt{\frac{(\mu m U_{eq} Z_k)^2 + A_{3-k}^2 (Z_1 - Z_2)^2}{(\mu m U_{eq})^2 + (A_1 + A_2)^2}}, \tag{3.7}$$

where $\mu = c\omega B$. For equilibrium, the inlet velocities U_1 and U_2 must be equal to the equilibrium velocity U_{eq}. This results in a system of two equations in A_1 and A_2 from which in principle the conditions for equilibrium can be derived. Two cases can be distinguished, equal amplitudes of the sea surface elevation ($Z_1 = Z_2$) and different amplitudes ($Z_1 \neq Z_2$).

For $Z_1 = Z_2 = Z_0$ there is an infinite number of equilibriums:

$$A_1^{eq} + A_2^{eq} = \frac{\mu m}{U_{eq}}\sqrt{\frac{Z_0^2}{(cm)^2} - U_{eq}^4}. \tag{3.8}$$

This is a straight line of equilibrium points in the (A_1, A_2)-space. Eq. (3.8) is only valid if the argument under the square root is positive, i.e. $Z_0 > cmU_{eq}^2$. From a linear stability analysis (see 3.C) it follows that the equilibriums are always *neutrally* stable, which means that when an arbitrary equilibrium is perturbed it will return to an equilibrium, however, not necessarily the same one. In nature, this situation is not often encountered, as usually the amplitudes off the inlets differ.

In case of $Z_1 \neq Z_2$ conditions under which equilibriums exist are difficult to derive directly from Eq. (3.7). Therefore, a slightly different approach is taken; see Appendix 3.A.2. From this the following expression for the equilibrium cross-sectional areas is derived:

$$A_k^{eq} = \frac{\mu m}{\sin \psi_1^{eq}}\left[\frac{Z_1 + Z_2}{4cmU_{eq}} - (-1)^k U_{eq}\left(\frac{1 - \cos^2 \psi_1^{eq}}{2\cos \psi_1^{eq}}\right)\right], \quad k = 1, 2, \tag{3.9}$$

where

$$\cos \psi_1^{eq} = \frac{\Delta Z}{2cmU_{eq}^2}. \tag{3.10}$$

Here, ψ_1 is the phase of the inlet velocity in inlet 1 and $\Delta Z = Z_1 - Z_2$. For A_1^{eq} and A_2^{eq} to be positive it follows from Eq. (3.9) that

$$\frac{Z_1 \Delta Z}{2(cm)^2 U_{eq}^4} \geq 1, \qquad \Delta Z > 0. \tag{3.11}$$

Table 3.2: Conditions for Equilibrium Cross-Sectional Areas to Exist and Stability Modes; Entrance/Exit Losses Only

Amplitude	Number of Equilibriums	Stability Mode
$Z_1 = Z_2 = Z_0$	Infinite, provided $Z_0 > cmU_{eq}^2$	Neutrally Stable
$\Delta Z > 0$	$\begin{cases} 1, \text{ provided } \frac{2(cm)^2 U_{eq}^4}{Z_1} \leq \quad \Delta Z \leq 2cmU_{eq}^2 \\ 0 \text{ in all other cases than above} \end{cases}$	Stable
$\Delta Z < 0$	$\begin{cases} 1, \text{ provided } \frac{2(cm)^2 U_{eq}^4}{Z_2} \leq -\Delta Z \leq 2cmU_{eq}^2 \\ 0 \text{ in all other cases than above} \end{cases}$	Stable

From Eq. (3.10) with $|\cos\psi_1| \leq 1$, it follows that

$$\frac{\Delta Z}{2cmU_{eq}^2} \leq 1, \qquad \Delta Z > 0. \tag{3.12}$$

Similar conditions as those given by Eqs. (3.11) and (3.12) hold for $\Delta Z < 0$. In that case, Z_1 is replaced by Z_2 in Eq. (3.11) and in Eqs. (3.11) and (3.12) ΔZ is replaced by $-\Delta Z$. From Eqs. (3.11) and (3.12) it follows that there is a limited interval of m-values for which equilibriums exist. The interval ranges from $m_{\min}$ to $m_{\max}$ with

$$m_{\min} = \frac{\Delta Z}{2cU_{eq}^2}, \tag{3.13}$$

and

$$m_{\max} = \frac{1}{cU_{eq}^2}\sqrt{\frac{Z_1 \Delta Z}{2}}. \tag{3.14}$$

It can be shown that the equilibriums in this interval are linearly stable (see Appendix 3.C). In Table 3.2 an overview is given of the conditions for equilibrium for both $Z_1 = Z_2$ and $Z_1 \neq Z_2$. In the same table their linear stability is indicated.

3.3.2 Physical explanation for the interval of stable equilibriums when $Z_1 \neq Z_2$

In the foregoing it is shown that for $m_{\min} \leq m \leq m_{\max}$ (physically realistic) stable equilibriums exist, i.e. the amplitude of the velocity in both inlets equals the equilibrium velocity. Given a value of m, inlet velocities depend on the difference in water level between basin and ocean. A logical question then is what are the amplitude and phase of the basin water level at times of equilibrium and how do they depend on the entrance/exit loss coefficient m?

Lower limit $m = m_{\min}$

Starting with $m = m_{\min}$, it is shown in Appendix 3.A.3 that for equilibrium the basin water level lies between the two ocean levels, i.e. $Z_b^{eq} = (Z_1 + Z_2)/2$, and they are in phase, i.e. $\varphi^{eq} = 0$. This corresponds to a situation with a minimal pressure gradient over both inlets simultaneously. Furthermore, it follows from Appendix 3.A.2 that at equilibrium the corresponding phases of the velocities in Inlet 1, ψ_1^{eq}, and Inlet 2, ψ_2^{eq}, are related by $\psi_2^{eq} = \pi - \psi_1^{eq}$. For $m = m_{\min}$, $\psi_1^{eq} = 0$ and thus the velocities in Inlet 1 and Inlet 2 are 180° out of phase. Hence, making use of the momentum equations (3.6), the water level difference between ocean and basin is the same for both inlets, but has opposite sign, and maximum ocean and basin water levels occur simultaneously. Subsequently, from continuity it follows that values of both equilibrium cross-sectional areas approach infinity.

Upper limit $m = m_{\max}$

For increasing m-values it follows from the momentum balance (Eq. 3.6) that the water level difference between ocean and basin has to increase to attain the equilibrium velocity in both inlets. This can only be satisfied if the basin water level increases and its phase decreases. For an explanation, see Appendix 3.A.3. Furthermore, it is shown in this appendix that from continuity it follows that A_2^{eq} decreases with increasing values of m and becomes zero for $m = m_{\max}$. For increasing m-values A_1^{eq} remains finite and is always larger than A_2^{eq}. ψ_1^{eq} increases and ψ_2^{eq} decreases for increasing values of m and thus the difference between the two phases decreases.

3.3.3 Model results

Using the continuation method and the parameter values in Table 3.1, last column, values of A_1^{eq} and A_2^{eq} as a function of m are presented in Fig. 3.4a, where a solid line indicates stable equilibrium solutions. As only entrance/exit losses are considered, Eq. (3.6) is used in the continuation method. For $m = m_{\min}$ both cross-sections go to infinity. For increasing values of m, A_2^{eq} becomes zero at $m = m_{\max}$. A_1^{eq} first decreases and then increases to reach a value of approximately $6 \cdot 10^4$ m^2 at $m_{\max}$. The black dotted lines in Fig. 3.4a indicate physically unrealistic equilibrium solutions, i.e. A_2^{eq} negative. They are added to show that theoretically equilibrium solutions are possible for $m > m_{\max}$. Using the equilibrium cross-sectional areas for corresponding m-values from Fig. 3.4a and the analytical expressions for Z_b, φ, ψ_1 and ψ_2 from Appendix 3.A.1, Figs. 3.4b and 3.4c are constructed. Fig. 3.4b shows the dependence of the amplitude of the basin surface elevation Z_b^{eq} on m, where Z_b^{eq} increases monotonically from $m_{\min}$ toward $m_{\max}$. Fig. 3.4c illustrates the behaviour of the phases of the velocity in Inlet 1, ψ_1^{eq},

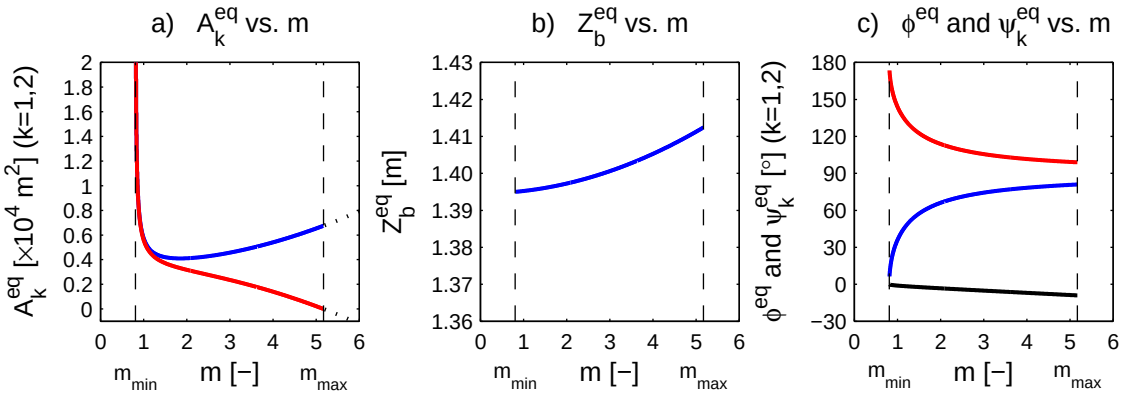

Figure 3.4: The role of entrance/exit losses. Dependence of system variables on entrance/exit losses (m) for equilibrium conditions. (a) Dependence of stable equilibrium cross-sectional areas for Inlet 1 (blue) and 2 (red). A black dotted line indicates physically unrealistic equilibriums. (b) Dependence of the amplitude of the basin water level. (c) Dependence of the phases of the basin water level (black) and the velocity in Inlet 1 (blue) and 2 (red). Calculations carried out using Eq. (3.6)*;* $Z_1 = 1.43$ *m,* $Z_2 = 1.36$ *m,* $\theta_k = 0$ $(k = 1, 2)$*.*

and 2, ψ_2^{eq}, and of the basin water level φ^{eq}. $\psi_1^{eq} = 0$ for $m_{\min}$ and increases with increasing values of m to a value of approximately 90° at $m = m_{\max}$. ψ_2^{eq} is 180° at $m_{\min}$ and decreases with increasing values of m to a value of approximately 90° at $m = m_{\max}$. $\varphi^{eq} = 0$ at $m_{\min}$ and decreases to a value of approximately -10° at $m_{\max}$. These findings are in agreement with the analytical results presented in Appendix 3.A.3 and summarised in the preceding paragraph of this section. It is noted that beyond $m = 2$ the results in Fig. 3.4 have no physical significance, however values up to $m = 6$ are shown for completeness.

3.3.4 Phase differences and stable equilibriums

To allow for an analytical solution, so far only amplitude differences between the two ocean tides have been considered. However, this does not imply that phase differences could not lead to stable equilibriums. To further investigate this, using the continuation method described in Subsection 3.2.2, equilibrium cross-sectional areas for inlets 1 and 2 are calculated for different values of $\Delta\theta = \theta_1 - \theta_2$. The results presented in Fig. 3.5 show that only unstable equilibrium inlet configurations are present. Although it is realised that only a limited parameter space is being considered, the suggestion is that phase differences between the ocean tide off the inlets alone do not lead to stable equilibriums. Besides the latter suggestion, the effect of phase differences in combination with amplitude differences will be investigated in more detail in Section 3.5.

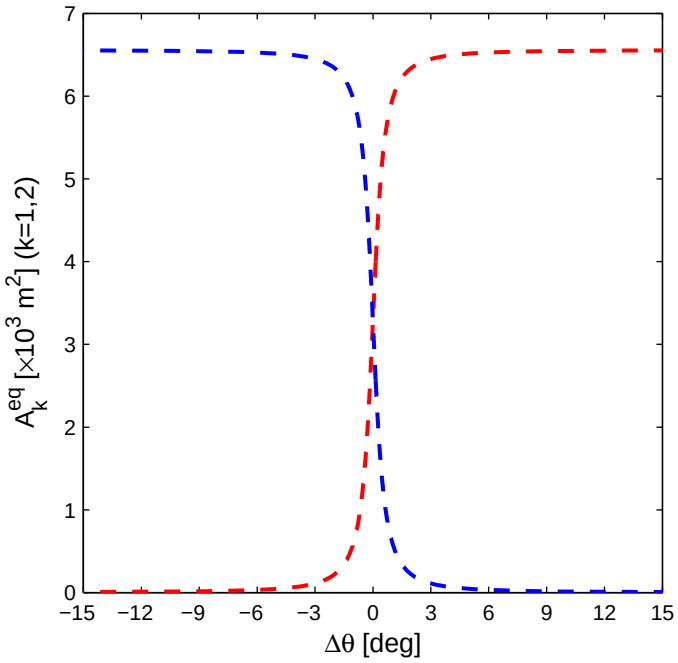

Figure 3.5: The role of a phase difference between the ocean tides. Dependence of the equilibrium cross-sectional areas of Inlet 1 (blue) and 2 (red) on the phase difference between the inlets $\Delta\theta$. A dashed line indicates unstable equilibriums. Calculations carried out using Eq. (3.6)*; $m = 1$, $Z_1 = Z_2 = 1.36\ m$, $\theta_2 = 0$ and variable θ_1.*

3.4 Bottom friction and inertia

In the previous section it was shown that with only entrance/exit losses and a difference in forcing amplitudes, stable double inlet systems can be found. However referring to Section 3.2, in the dynamic equations (3.2) inertia and bottom friction are not necessarily small compared to entrance/exit losses and, therefore, could play a role in the equilibrium of the inlets. In the following the effect of these terms on the cross-sectional stability is further investigated. In the analysis the additional restriction is made that the two inlets have the same length.

3.4.1 Bottom Friction

Including bottom friction in Eq. (3.6) results in

$$cU_{eq}\left(m + \frac{2FL}{\gamma\sqrt{A_k}}\right)u_k = \zeta_k - \zeta_b, \tag{3.15}$$

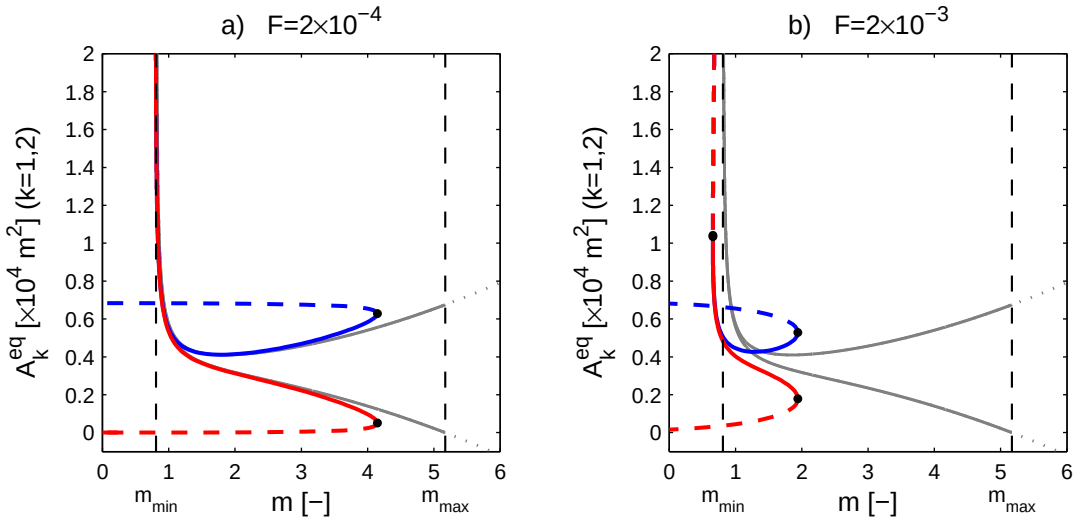

Figure 3.6: The role of bottom friction. Dependence of the equilibrium cross-sectional area of Inlet 1 (blue) and Inlet 2 (red) on the entrance/exit loss coefficient m in the presence of (a) little bottom friction $F = 2 \cdot 10^{-4}$ and (b) the default bottom friction $F = 2 \cdot 10^{-3}$. A solid line indicates stable equilibriums and a dashed line unstable ones. A grey line indicates stable equilibrium solutions for entrance/exit losses only, where the dotted part indicates physically unrealistic equilibriums. Calculations carried out using Eq. (3.15); $L = 1$ km, $\gamma = 0.2$, $Z_1 = 1.43$ m, $Z_2 = 1.36$ m, $\theta_k = 0$ $(k = 1, 2)$.

with $c = 4/(3\pi g)$. Using this equation, the relationship between A_k^{eq} and m is shown for a small and a large value of bottom friction in respectively Figs. 3.6a and 3.6b. The two figures are constructed using the default values in Table 3.1, except for Fig. 3.6a where $F = 2 \cdot 10^{-4}$ instead of $F = 2 \cdot 10^{-3}$. The corresponding figure for entrance/exit losses only is Fig. 3.4a. For comparison the curves in this figure are reproduced in both Figs. 3.6a and 3.6b. From these figures it can be seen that when including bottom friction, unstable as well as stable equilibrium cross-sectional areas are present (shown as a dashed line). The transition from stable to unstable equilibriums constitutes a limit point marked with a black dot. Figs. 3.6a and 3.6b show that when increasing bottom friction the maximum and minimum values of m for which there are stable equilibriums decrease. The decrease is larger for the maximum than for the minimum value, resulting in a decrease in the range of m-values for which there are stable equilibriums. The shift in m-values increases with increasing bottom friction. An explanation for this shift in m-values is presented in Appendix 3.B.

The behaviour of the system when increasing bottom friction is in some ways similar to that when increasing the entrance/exit losses. This is shown in Fig. 3.7 where for stable equilibrium conditions (unstable solutions are not shown) the dependence of system variables on bottom friction (by varying the inlet length L) is shown. The dependence of the cross-sectional areas, the basin level amplitude

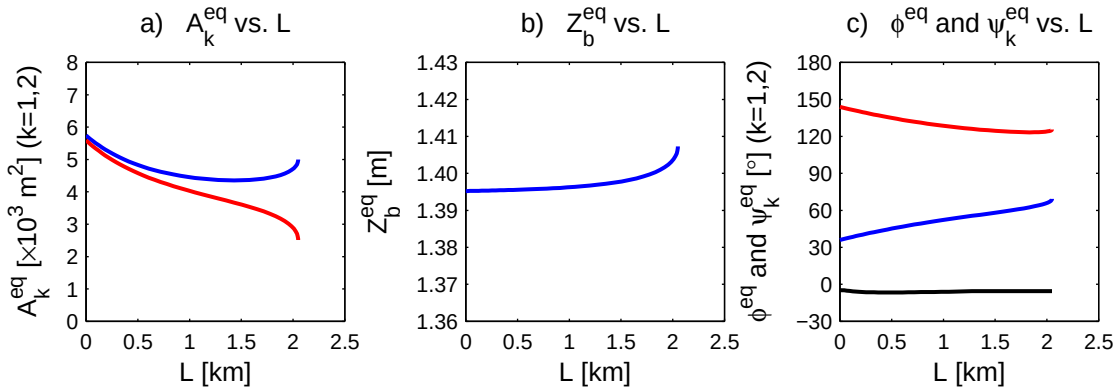

Figure 3.7: The role of bottom friction. Dependence of (a) stable equilibrium cross-sectional areas for Inlet 1 (blue) and 2 (red), (b) the amplitude of the basin water level, and (c) the phases of the basin water level (black) and the velocity in Inlet 1 (blue) and Inlet 2 (red) on bottom friction (L) for equilibrium conditions. Calculations carried out using Eq. (3.15)*;* $m = 1$*,* $F = 2 \cdot 10^{-3}$*,* $\gamma = 0.2$*,* $Z_1 = 1.43$ *m,* $Z_2 = 1.36$ *m,* $\theta_k = 0$ *(*$k = 1, 2$*).*

and the phases of the basin level and inlet velocities in Inlet 1 and 2 on the inlet length is shown in respectively Fig. 3.7a, 3.7b and 3.7c. When only considering entrance/exit losses these dependencies are displayed in Fig. 3.4. In comparing Figs. 3.4 and 3.7 it should be realised that in Fig. 3.7 in addition to bottom friction, entrance/exit losses (corresponding to $m = 1$) are present. Therefore, only the part of Fig. 3.4 beyond $m = 1$ should be compared to Fig. 3.7. From this comparison it follows that A_k^{eq}, Z_b^{eq}, φ^{eq}, ψ_k^{eq} ($k = 1, 2$) show the same trend for increasing m and increasing L. In particular, Z_b^{eq} increases and φ^{eq} decreases with increasing values of L. From this it can be concluded that, similarly to entrance/exit losses, when bottom friction is increased, the equilibrium velocity is attained by an increase in basin level and a decrease in basin level phase.

3.4.2 Inertia

When adding inertia to Eq. (3.15) the effect on the range of m-values for which stable equilibriums exist is shown in Fig. 3.8, together with the case for entrance/exit losses and bottom friction only (depicted as a grey line). This figure is constructed using the default parameter values of Table 3.1. The curves in Fig. 3.8 are qualitatively similar. For this particular case adding inertia decreases the range of (physically realistic) m-values for which stable equilibriums exist. Results of additional numerical experiments (see also Fig. 3.9a) show that the effect of adding inertia is somewhat sensitive to the other parameter values and can also increase the range of m-values for which stable equilibriums exist. Therefore, care should be taken in generalising the foregoing conclusion.

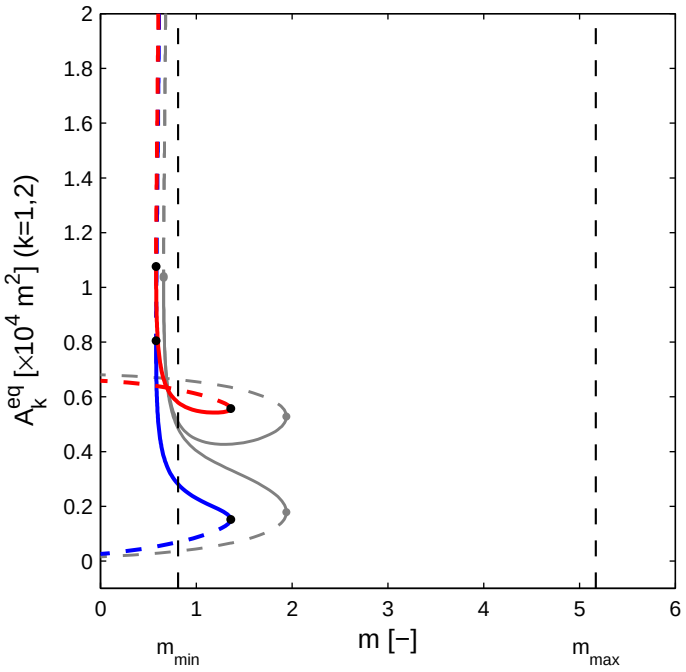

Figure 3.8: The role of inertia. Dependence of the equilibrium cross-sectional area of Inlet 1 (blue) and Inlet 2 (red) on the entrance/exit loss coefficient m in the presence of bottom friction and inertia. A solid line indicates stable equilibriums and a dashed line unstable ones. A grey line indicates equilibrium solutions for entrance/exit losses and bottom friction only. Calculation are carried out using Eq. (3.2)*; $F = 2 \cdot 10^{-3}$, $L = 1$ km, $\gamma = 0.2$, $Z_1 = 1.43$ m, $Z_2 = 1.36$ m, $\theta_k = 0$ $(k = 1, 2)$.*

3.4.3 Relative Importance of the Entrance/Exit Loss Term and the Bottom Friction Term

In the preceding subsection it is shown that bottom friction in the presence of entrance/exit losses can lead to stable double inlet systems. However, from Fig. 3.6 it follows that increasing the amount of bottom friction leads to a significantly smaller range of m-values where stable equilibriums can be found. This suggests that there is a limit to the amount of bottom friction that can be added, such that stable equilibriums still exist. This is further investigated in this subsection.

Using the continuation method, the range of m-values where stable equilibriums are found in Fig. 3.8 (notice that this range between two limit points is similar for A_1^{eq} and A_2^{eq}) is calculated for values of L ranging between 0 and 1.6 km. This results in the blue curve plotted in Fig. 3.9a. Each point on the curve corresponds to a value of m, L and A_k^{eq} $(k = 1, 2)$. Stable equilibriums are found for combinations of m, L and A_k^{eq} inside this curve. It follows that stable equi-

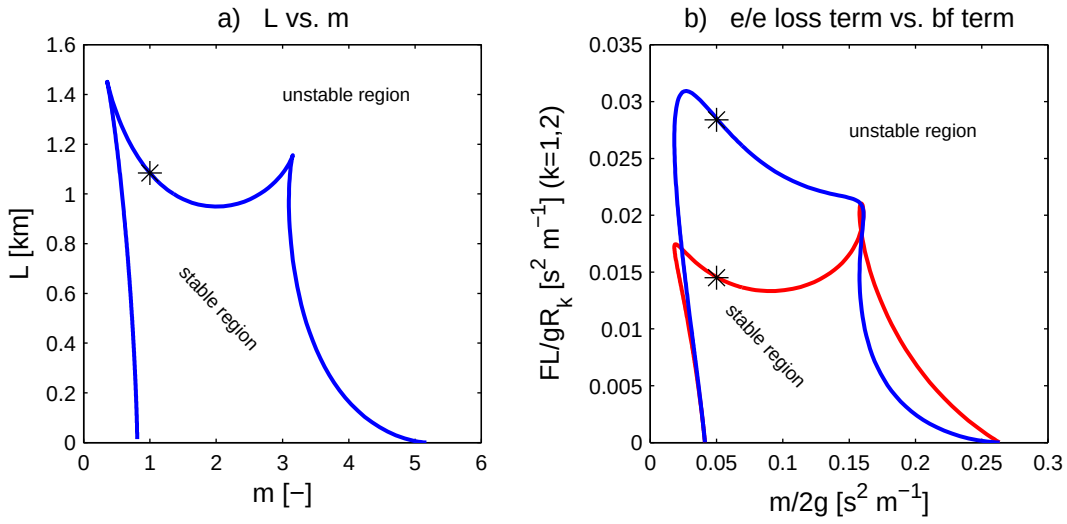

Figure 3.9: Relative importance of entrance/exit loss term and bottom friction term. (a) Values of entrance/exit loss coefficient m and inlet length L for which there are stable equilibriums. (b) Values of the entrance/exit loss term and bottom friction term for Inlet 1 (blue) and Inlet 2 (red) for which there are stable equilibriums. For the significance of the asterisk see text. Calculations carried out using Eq. (3.2)*;* $F = 2 \cdot 10^{-3}$, $\gamma = 0.2$, $Z_1 = 1.43\,m$, $Z_2 = 1.36\,m$, $\theta_k = 0\,(k = 1, 2)$.

libriums exist for values of L smaller than approximately 1 km. In some cases L can be as high as approximately 1.5 km. As an example, the range of (physically realistic) m-values where stable equilibriums are found for $L = 1$ km in Fig. 3.9a, i.e. between approximately 0.6 and 1.4, corresponds to the range of m-values found in Fig. 3.8. Note that for $L = 1$ km a second range of m-values where stable equilibriums are found exists between approximately 2.7 and 3.1. For this range, however, the m-values are physically unrealistic and therefore this range is not shown in Fig. 3.8. Furthermore, it can be seen that for very small L, i.e. negligible bottom friction and inertia, the range of m-values for which there are stable equilibriums lies between approximately 0.8 and 5.2, which corresponds with the values for $m_{\min}$ and $m_{\max}$ that follow from Eqs. (3.13) and (3.14) and the default parameter values from Table 3.3.

For each of the points on the curve in Fig. 3.9a the value of the bottom friction term $FL/(g\gamma\sqrt{A_k^{eq}})$ is calculated and plotted versus the entrance/exit loss term $m/(2g)$ in Fig. 3.9b. Because each point on the curve in Fig. 3.9a has different values for A_1^{eq} and A_2^{eq} (see also Fig. 3.8), the bottom friction term has a different value for each inlet. The blue curve corresponds to Inlet 1 and the red curve to Inlet 2. Values of F and γ are those listed in Table 3.1. To emphasise that a single point on the blue curve in Fig. 3.9a corresponds to a point on both the blue curve (Inlet 1) and the red curve (Inlet 2) in Fig. 3.9b, black asterisks are added in both figures for $m = 1$ and thus $m/(2g) = 0.05$ s^2 m^{-1}. It can be seen from Fig. 3.9b that, starting at zero bottom friction, when increasing the value of the bottom fric-

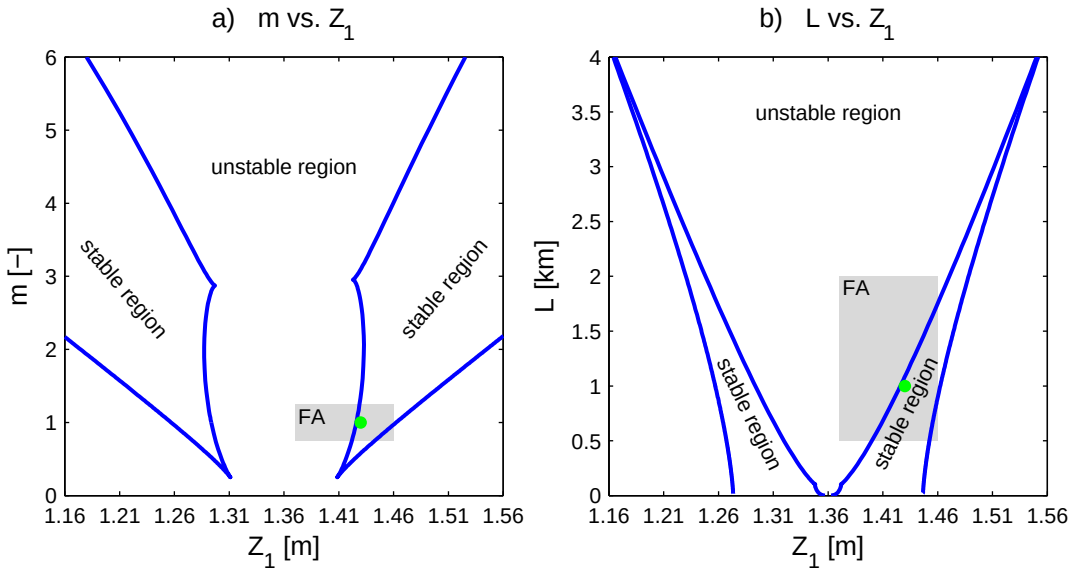

Figure 3.10: Dependence of stable equilibriums on the ocean tidal amplitude of Inlet 1. (a) Values of Z_1 and m for which stable equilibriums exist, where $L = 1$ km. (b) Values of Z_1 and L for which stable equilibriums exist, where $m = 1$. The green solid dot corresponds with parameter values for the symmetric Faro-Armona system. The grey box indicates the assumed range of parameter values for the asymmetric system (see text Section 3.6). Calculations carried out using Eq. (3.2)*; $F = 2 \cdot 10^{-3}$, $\gamma = 0.2$, $Z_2 = 1.36$ m, $\theta_k = 0$ $(k = 1, 2)$.*

tion term the range of m-values for which there are stable equilibriums generally decreases. This is in agreement with the observations made in Subsection 3.4.1. For a given value of the entrance/exit loss term there is a limit to the bottom friction that can be added. The limit value of the bottom friction term is in most cases smaller than the corresponding value of the entrance/exit loss term. Taking as a typical value $m = 1$ and thus $m/(2g) = 0.05$ s^2 m^{-1}, corresponding to the black asterisks in Fig. 3.9b, the maximum of the bottom friction term for Inlet 1 is approximately 0.028 and for Inlet 2 approximately 0.015. This results in a ratio of entrance/exit loss term and bottom friction term of respectively 1.79 and 3.3. In conclusion the entrance/exit loss term has to be considerably larger than the bottom friction term for a double inlet system to be stable.

3.5 Effect of forcing on stable equilibriums

Parameters in the forcing are Z_k and θ_k $(k = 1, 2)$. In Section 3.3 it is shown that for entrance/exit losses only, ocean tidal amplitudes and amplitude differences determine whether or not stable equilibriums exist. The effect of the ocean tidal amplitude when using the complete dynamic equation is demonstrated in Figs. 3.10a and 3.10b where the regions of stable equilibriums are plotted in re-

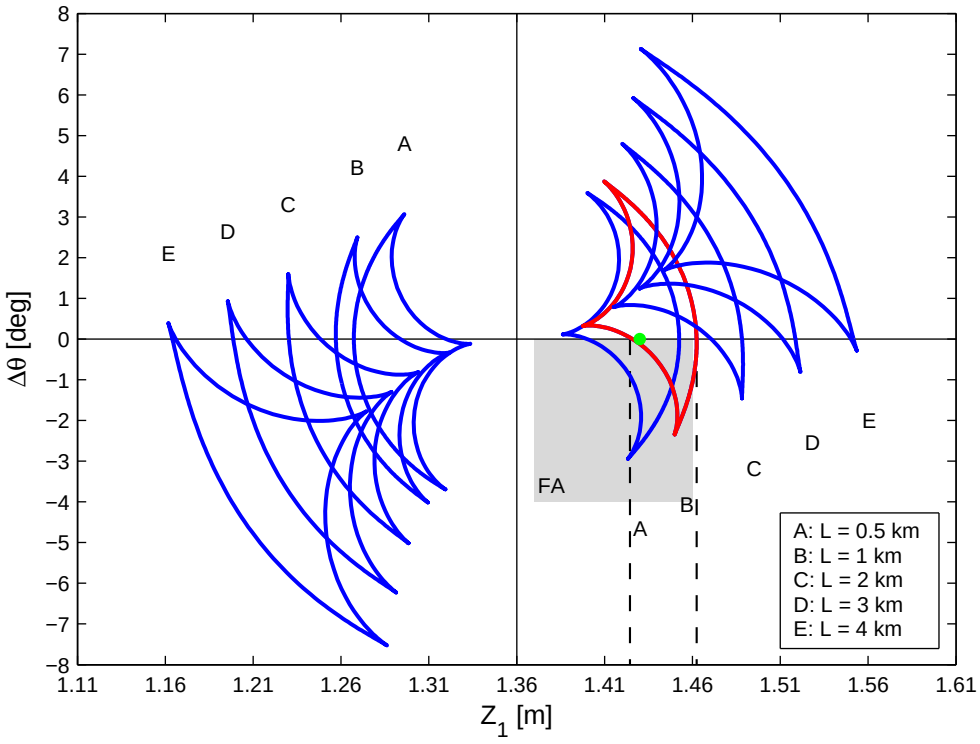

Figure 3.11: Regions in which stable equilibriums exist for different values of Z_1, $\Delta\theta = \theta_1 - \theta_2$ and L. The red region indicates the default case (Table 3.3) with $L = 1$ km. The solid green dot corresponds with parameter values for the symmetric Faro-Armona system. The grey box indicates the assumed range of parameter values for the asymmetric system (see text Section 3.6). For explanation of the dashed vertical line see text Section 3.5. The red region indicates the region for the symmetric Faro-Armona case with L = 1 km. Calculations carried out using Eq. (3.2)*; $m = 1$, $F = 2 \cdot 10^{-3}$, $\gamma = 0.2$, $Z_2 = 1.36$ m, $\theta_2 = 0$.*

spectively the (Z_1, m)-space and the (Z_1, L)-space. The parameters m and L can be interpreted as measures for respectively the entrance/exit losses and the bottom friction losses. It follows from Fig. 3.10a that for increasing Z_1-values and keeping Z_2 constant at 1.36 m, the range of m-values for which there are stable equilibriums shifts to larger values of m. Similarly to m it follows from Fig. 3.10b that for increasing Z_1-values and keeping Z_2 constant at 1.36 m, the range of L-values for which there are stable equilibriums shift to larger L-values.

The influence of phase differences between the ocean tides $\Delta\theta = \theta_1 - \theta_2$ on the presence of stable equilibriums is demonstrated in Fig. 3.11. This figure is based on a practical situation for which it is generally assumed that $F = 2 \cdot 10^{-3}$ and $m = 1$. In the figure $\Delta\theta$ is plotted versus Z_1 with L as parameter. The range of Z_1-values between the dashed lines (red region) correspond to the default case

with $L = 1$ km and $m = 1$. This range corresponds with the range for Z_1 in Fig. 3.10a with $m = 1$ and in Fig. 3.10b with the range for Z_1 for $L = 1$ km. From Fig. 3.11 the following general conclusions can be drawn.

- $Z_1 = Z_2$. No curve crosses the ordinate. This was further confirmed by calculations with $L < 0.5$ km (not shown here). Therefore, phase differences between the inlets alone cannot cause a double inlet system to be in a stable equilibrium. A similar conclusion was arrived at when discussing entrance/exit losses only; see Section 3.3.
- $Z_1 \neq Z_2$. Phase differences between the ocean tides affect the stability region, i.e. the range of Z_1-values for which there are stable equilibriums. As an example for $L = 2$ km, increasing $\Delta\theta$ from 0 to 1° increases the range of Z_1-values for which there are stable equilibriums from $1.47 < Z_1 < 1.49$ to $1.42 < Z_1 < 1.48$.
- $\theta_1 = \theta_2$ and $\theta_1 \neq \theta_2$. For stable equilibriums the difference between Z_1 and Z_2 increases for increasing bottom friction (increasing L). As an example for $Z_1 > Z_2$, the values of Z_1 are larger for $L = 4$ km than for $L = 0.5$ km.

3.6 The Faro-Armona double inlet system

The Faro-Armona double inlet system was already introduced in Section 1.3. Summarising, it is the western sub-system of the multiple-inlet barrier island system Ría Formosa on the southern coast of Portugal (see Fig 1.3 on page 7). It consists of the Armona, Faro and Ancão Inlets, and covers approximately 3.4×10^7 m^2. The Faro and Armona Inlets capture 90% of the tidal prism of the western sub-system and, moreover, there exists a relatively long winding connection between Faro/Armona Inlets and Ancão Inlet (Salles et al., 2005, and references therein). This suggests that, as a first approximation, the Faro and Armona Inlets can be treated as a double inlet system only. Furthermore, the Faro-Armona system may be considered stable (Pacheco et al., 2011a).

For our approach to be applicable to the Faro-Armona system, typical values of bulk parameters are estimated using observations and modelling results presented in Salles et al. (2005); Dias & Sousa (2009); Pacheco et al. (2010, 2011a,b) and references therein. Geometrical parameters were also estimated using Google Earth. Specifically, to determine the shape factor for the Faro and Armona Inlets, a rectangular cross-sectional area is assumed. From the above mentioned sources characteristic ranges of parameters were found, see Column 2 and 4 of Table 3.3. Based on these parameter ranges and making some reasonable assumptions the most likely parameter values for the system used for the lumped parameter model are listed in the third and fifth column of Table 3.3. In Table 3.3 tidal amplitudes pertain to spring tide conditions as observed off the inlets (Stations F and H in Dias & Sousa (2009), Fig. 5).

Table 3.3: Parameter Values Representative for the Faro-Armona double inlet system

	Armona Inlet (1)		Faro Inlet (2)	
Parameter	**Range**	**Model**	**Range**	**Model**
Inlets				
A_i (m^2)	$\sim 2,000$ [c],[d]	variable	$\sim 4,000$ [c],[d]	variable
L_i (km)	$0.5 - 1$ [f]	0.7	$1 - 2$ [d],[f]	2
m_i (-)	$0.75 - 1.25$ [e]	1	$0.75 - 1.25$ [e]	1
γ_i (-)	$0.05 - 0.13$ [a]	0.12	$0.2 - 0.37$ [a],[d]	0.2
F_i (-)	$0.002 - 0.0027$ [a]	0.002	$0.0011 - 0.002$ [a],[d]	0.002
U_{eq} (m s^{-1})	~ 1.05 [c]	1	$0.9 - 1.18$ [a]	1
Forcing				
ω^* (s^{-1})	-	1.4×10^{-4}		
Z_i (m)	~ 1.43 [b]	1.43	~ 1.36 [b]	1.36
ΔZ^* (m)	$0.01 - 0.1$ [b],[c]	0.07		
$\Delta\theta^*$ (deg)	-4 – 0 [b]	0		
General				
B (m^2)	$\sim 2.5 \times 10^7$ [c]	2.5×10^7	$\sim 0.9 \times 10^7$ [c]	0.9×10^7
M^* (m^3 $year^{-1}$)	$4 \times 10^4 - 3 \times 10^5$ [d],[e]	1×10^5		

[a] Salles et al. (2005) [b] Dias & Sousa (2009) [c] Pacheco et al. (2010) [d] Pacheco et al. (2011a) [e] Pacheco et al. (2011b) [f] Google Earth [*] pertaining to the entire system

Using the parameter values in Column 3 and 5 of Table 3.3 it is of interest to show how far the conditions for stability derived in Sections 3.3-3.5 are satisfied keeping in mind that these conditions were derived for a symmetric system. When neglecting bottom friction and inertia in the dynamic equation and only including entrance/exit losses the range of m-values for a stable system is between 0.8 and 5.2 (Eqs. (3.13) and (3.14)). When including bottom friction both the maximum and minimum values are slightly reduced. Adding inertia the minimum m-value slightly decreases and the maximum m-value slightly increases. It seems safe to conclude that the adopted value $m = 1$ satisfies the condition for stability. A second condition is that entrance/exit losses are considerably larger than bottom friction losses. Using $m = 1$ for both inlets it follows that the entrance/exit loss term $m/(2g) \approx 0.05\ s^2\ m^{-1}$. Taking for Armona Inlet $F_1 = 0.002$, $L_1 = 0.7$ km, $\gamma_1 = 0.12$, $A_1 = 2,000\ m^2$ and for Faro-Alhão Inlet $F_2 = 0.002$, $L_2 = 2$ km, $\gamma_2 = 0.2$, $A_2 = 4,000\ m^2$, bottom friction terms $FL/(gR)$ of approximately 0.026 and 0.032 $s^2\ m^{-1}$, respectively, are obtained. Thus, for both inlets the entrance/exit loss term is larger than the bottom friction term.

In the forgoing it is shown that a symmetric system resembling Faro-Armona satisfies the theoretically derived conditions for cross-sectional stability. Referring to Fig. 3.2, for this system a stable equilibrium is indeed present. To investigate if this is also the case for the actual asymmetric system a flow diagram is constructed using the most likely parameter values for Faro-Armona listed

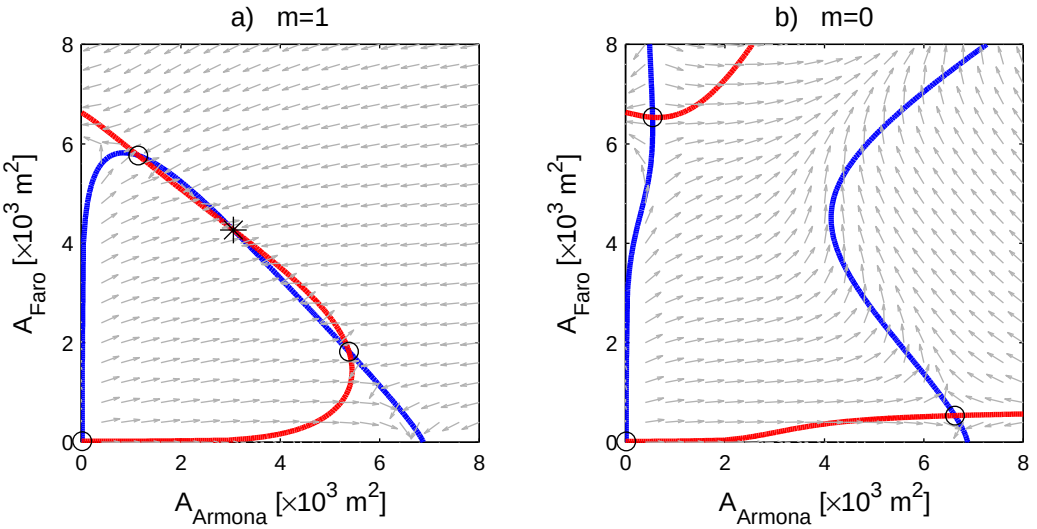

Figure 3.12: Flow diagram for Faro-Armona double inlet system when (a) including entrance/exit losses: $m = 1$ and (b) excluding entrance/exit losses: $m = 0$. The blue and red solid line correspond to the equilibrium flow curves of Armona and Faro, respectively, the grey vectors indicate the direction in which the values of the cross-sectional areas change when they are not in equilibrium, the black circles indicate an unstable equilibrium and the black cross indicates a stable equilibrium. Calculations carried out using Eq. (3.2)*; $F = 0.002$, $L_1 = 0.7$ km, $L_2 = 2$ km, $\gamma_1 = 0.12$, $\gamma_2 = 0.2$, $Z_1 = 1.43$ m, $Z_2 = 1.36$ m, $\Delta\theta = 0$.*

in Columns 3 and 5 of Table 3.3. The flow diagram is presented in Fig. 3.12a and, next to three unstable equilibriums, shows a stable equilibrium with cross-sectional areas of approximately 3,000 m^2 for Armona and 4,000 m^2 for Faro. This is close to the observed values listed in Table 3. In Fig. 3.12b the same flow diagram is presented for $m = 0$: no stable equilibriums are present, illustrating the importance of including entrance/exit losses in the stability analysis.

In Figs. 3.10 and 3.11 in the previous section the grey boxes indicate the range of parameter values from Columns 2 and 4 of Table 3.3. Keeping in mind that Figs. 3.10 and 3.11 pertain to a symmetric system discussed in Section 3.2.2, the grey boxes show that depending on the choice of the value of the particular parameter the system can be stable or unstable.

3.7 Discussion

The present approach to evaluate cross-sectional stability is based on the premise that when at equilibrium the amplitude of the tidal velocity in both inlets is close to 1 m s^{-1}. Velocities in the inlets are calculated using a lumped-parameter model. Using this approach it is shown that double inlets can be stable provided bottom friction and inertia in the inlet are small compared to entrance/exit losses. Essentially this limits cross-sectional stability to double inlet systems with rela-

tively short inlets. In addition, the amplitudes of the tides off the two inlets have to be different.

Referring to Figs. 3.10 and 3.11, cross-sectional stability is limited to a relatively narrow range of parameter values. Parameters include the entrance/exit loss coefficient m, the bottom friction factor F, the basin surface area B and the inlet length L. In addition, there is the value of the equilibrium velocity U_{eq}. In particular, the values of m and F require calibration and validation of the lumped-parameter model. In applying the stability analysis to the Faro-Armona system values of m and F were ascertained from previous studies carried out by other investigators. Inlet length was also estimated from Google Earth. Values of the amplitudes of the offshore tide were determined from measurements. The value of U_{eq} was taken from the literature and taken as a constant value to allow an analytical approach. Even though the 1 m s^{-1} for the equilibrium velocity is a generally accepted value, starting with the empirical cross-sectional area tidal prism relationship (A-P relationship), recent studies suggest that this value is a (weak) function of littoral drift and cross-sectional area rather than a constant (van de Kreeke, 2004).

The fact remains that the zero-dimensional lumped-parameter model including the assumption of a pumping mode for the basin represents a simplification of an essentially 2D hydrodynamics problem. Admittedly, this is a simplification that, similar to the constant value of U_{eq}, was introduced to allow an analytical approach to derive conditions for stability. The ability of the lumped-parameter models to capture the dynamics of the flow was shown in Herman (2007) who applied both a 2D hydrodynamics model and a lumped-parameter model to inlets in the German Wadden Sea.

In view of the sensitivity of the stability to the various parameters in the lumped-parameter model as well as the assumed stability criterion (the equilibrium velocity), the present application to the Faro-Armona system is of a diagnostic nature. To arrive at a predictive approach it is suggested to combine results obtained with the type of models used in this paper and process-based models in which water motion and sediment transport are based on physical first principles (e.g, de Vriend & Ribberink, 1996; Pacheco et al., 2011b; Nahon et al., 2012; Tung et al., 2012; Wang & Beck, 2012). At present, neither of these models can be used to make predictions. Therefore, it is important to improve both the lumped-parameter models and process-based morphodynamic models for tidal inlets. A possible first step to improve the lumped-parameter model is to investigate the applicability and limitations of the pumping mode assumption. With regards to the Faro-Armona system an improved estimate of the equilibrium velocity could be obtained if for this part of the Portuguese coast the AP relationship was known.

3.8 Conclusions

In evaluating the cross-sectional stability of tidal inlets it has been customary to describe the hydrodynamics with a lumped-parameter model. In this model the dynamics of the flow in the inlet constitutes a balance between inertia, entrance/exit losses and bottom friction on the one hand and the pressure gradient across the inlet on the other hand. A pumping mode is assumed for the basin.

In this chapter the role of inertia, entrance/exit losses and bottom friction on the cross-sectional stability of a double inlet system is investigated with emphasis on entrance/exit losses. The reason for this is that results of previous studies suggest that when neglecting entrance/exit losses no stable equilibriums are present. In the present study both analytical models and numerical experiments are used. To allow a physical explanation of the various terms in the lumped-parameter model use is made of a simplified version of the Faro-Armona system in which the length, friction factor and entrance/exit loss coefficient are the same for both inlets and the offshore tides may differ. The Faro-Armona double inlet system is part of the Ría Formosa, Portugal. This inlet system can be considered to be in stable equilibrium.

The model results in this chapter lead to the following conclusions. When retaining only entrance/exit losses and neglecting inertia and bottom friction, stable equilibriums are possible provided the two off-shore water level amplitudes are different. A difference in phase between the ocean tides does not lead to stable inlets.

Adding bottom friction, stable equilibriums exist provided the entrance/exit loss term is considerably larger than the bottom friction term. Increasing bottom friction leads to a downward shift and narrowing of the range of entrance/exit loss coefficients for which stable equilibriums exist.

Adding inertia, thus using the complete dynamic equation, somewhat affects the range of values of the entrance/exit loss coefficient for which stable cross-sections exist. Depending on the various parameter values the range can either increase or decrease.

In addition to the terms in the dynamic equation, the magnitude of the amplitudes of the off-shore tides and their differences affect the presence of stable equilibriums. For example, for stable equilibriums to exist an increase in the difference between the amplitude requires an increase in the entrance/exit loss term and/or an increase in the bottom friction term. Phase differences between the off-shore tides affect the range of amplitude differences where stable equilibriums exist.

For the simplified symmetric version of the Faro-Armona system it is shown that the presence of stable equilibriums is sensitive to the selection of parameter values such as inlet length, bottom friction factor and entrance/exit loss coefficient. This makes it difficult for practical cases to use the lumped-parameter model as a predictive tool.

Applying the stability analysis to the actual Faro-Armona system and judiciously selecting parameter values it is shown that the stability of this system can be explained (as opposed to predicted) using the lumped-parameter model together with the condition that inlets are stable when the velocity amplitude equals the equilibrium velocity (~ 1 m s^{-1}).

3.A Entrance/Exit Losses Only

In this appendix the analytical derivations to support the explanation of the role of the entrance/exit loss coefficient m on the equilibrium and stability of double inlet systems are given.

3.A.1 Basin Tide and Inlet Velocities

Neglecting inertia and bottom friction, the linearised equations for the water motion in the inlets are:

$$cmU_{eq}u_k = \zeta_k - \zeta_b, \qquad k = 1, 2, \tag{3.A.1}$$

with, $c = 4/(3\pi g)$. Assuming a pumping mode for the basin the continuity equation is:

$$B\frac{d\zeta_b}{dt} = A_1u_1 + A_2u_2. \tag{3.A.2}$$

The open boundary condition, which now only allows amplitude differences, is:

$$\zeta_k = \Re\left\{Z_k e^{i\omega t}\right\}, \tag{3.A.3}$$

where $\Re$ is the real part and Z_k is real-valued. To arrive at an analytical solution for the basin tide and inlet velocities the following trial solutions are introduced:

$$\zeta_b \sim \Re\left\{Z_b e^{i(\omega t+\varphi)}\right\}, \tag{3.A.4}$$

$$u_k \sim \Re\left\{U_k e^{i(\omega t+\psi_k)}\right\}, \tag{3.A.5}$$

where Z_b and U_k are real-valued. Eliminating u_k between Eqs. (3.A.1) and (3.A.2) results in an equation for the basin tide ζ_b. Substituting ζ_k and the trial solution for ζ_b in this equation and separating into real and imaginary parts leads to expressions for the amplitude Z_b and phase φ of the basin tide. It follows that

$$\tan\varphi = \frac{-\mu m U_{eq}}{(A_1 + A_2)}, \tag{3.A.6}$$

where $\mu = c\omega B$. The phase φ is in the fourth quadrant, i.e. $-\pi/2 < \varphi < 0$. As expected, the sea surface elevation precedes the basin surface elevation. The amplitude of the basin tide is

$$Z_b = \frac{(A_1Z_1 + A_2Z_2)}{\sqrt{(\mu m U_{eq})^2 + (A_1 + A_2)^2}}. \tag{3.A.7}$$

Substituting the trial solution for u_k in Eq. (3.A.1) and separating into real and imaginary parts leads to expressions for the amplitude U_k and phase ψ_k of the inlet velocity as a function of the known expressions Z_b (Eq. 3.A.7) and φ (Eq. 3.A.6). Substituting these expressions it follows that

$$\tan\psi_k = \frac{\mu m U_{eq}(A_1 Z_1 + A_2 Z_2)}{((\mu m U_{eq})^2 + (A_1 + A_2)^2)Z_k - (A_1 Z_1 + A_2 Z_2)(A_1 + A_2)}. \quad (3.A.8)$$

When deriving the expression for $\sin\psi_k$ from Eq. (3.A.8), it follows that it is always positive and thus ψ_k is located in the first or second quadrant. From Eq. (3.A.8) it then follows that ψ_k is in the first quadrant when the denominator is positive and in the second quadrant when the denominator is negative. In both cases the velocity precedes the ocean tide. The amplitude of the inlet velocity is

$$U_k = \frac{1}{cmU_{eq}}\sqrt{\frac{(\mu m U_{eq} Z_k)^2 + A_{3-k}^2 (Z_1 - Z_2)^2}{(\mu m U_{eq})^2 + (A_1 + A_2)^2}}. \quad (3.A.9)$$

3.A.2 Conditions for Equilibrium Cross-Sections for $Z_1 \neq Z_2$

Eliminating ζ_b between Eqs. (3.A.1) and (3.A.2) results in two equations in u_1 and u_2. Substituting the trial solutions for u_k (Eq. 3.A.5) and taking $U_k = U_{eq}$, two equations are obtained with the equilibrium cross-sectional areas A_1^{eq} and A_2^{eq} as unknowns:

$$(A_1^{eq} + i\mu m U_{eq})U_{eq} e^{i\psi_1^{eq}} + A_2^{eq} U_{eq} e^{i\psi_2^{eq}} = i\omega B Z_1, \quad (3.A.10)$$

$$(A_2^{eq} + i\mu m U_{eq})U_{eq} e^{i\psi_2^{eq}} + A_1^{eq} U_{eq} e^{i\psi_1^{eq}} = i\omega B Z_2. \quad (3.A.11)$$

Writing the real and imaginary parts of Eqs. (3.A.10) and (3.A.11) it can be shown that for $Z_1 \neq Z_2$ these equations can only be satisfied provided the phases of the inlet velocities are related as $\psi_2^{eq} = \pi - \psi_1^{eq}$. Making use of this, the following solution for A_k^{eq} is obtained:

$$A_k^{eq} = \frac{\mu m}{\sin\psi_1^{eq}}\left[\frac{Z_1 + Z_2}{4cmU_{eq}} - (-1)^k U_{eq}\left(\frac{1 - \cos^2\psi_1^{eq}}{2\cos\psi_1^{eq}}\right)\right]. \quad (3.A.12)$$

Subtracting the imaginary parts of Eqs. (3.A.10) and (3.A.11) and substituting ψ_2^{eq} it follows that

$$\cos\psi_1^{eq} = \frac{\Delta Z}{2cmU_{eq}^2}, \quad (3.A.13)$$

where $\Delta Z = Z_1 - Z_2$. As shown in Appendix 3.A.1, depending on the sign of the denominator of Eq. (3.A.8), ψ_1^{eq} is in the first or second quadrant. It follows from Eq. (3.A.13) that for inlets that are in equilibrium and $\Delta Z > 0$, ψ_1^{eq} is in the first quadrant.

With $\sin\psi_k^{eq}$ positive (see Appendix 3.A.1) a requirement for A_k^{eq} to be positive is that the expression between square brackets in Eq. (3.A.12) is positive. With the expression for $\cos\psi_1^{eq}$ given by Eq. (3.A.13) this leads to the condition

$$\frac{Z_1 \Delta Z}{2(cm)^2 U_{eq}^4} \geq 1, \qquad \Delta Z > 0. \tag{3.A.14}$$

A second condition for Eq. (3.A.12) to be a valid solution for A_k^{eq} is that the absolute value of $\cos\psi_1^{eq}$ is equal to or smaller than one, and thus from Eq. (3.A.13)

$$\frac{\Delta Z}{2cmU_{eq}^2} \leq 1, \qquad \Delta Z > 0. \tag{3.A.15}$$

Similar conditions as expressed by Eqs. (3.A.14) and (3.A.15) hold for $\Delta Z < 0$. In that case in Eq. (3.A.14) Z_1 is replaced by Z_2 and in Eqs. (3.A.14) and (3.A.15) ΔZ is replaced by $-\Delta Z$.

3.A.3 The Role of the Entrance/Exit Loss Coefficient m

From Eqs. (3.A.14) and (3.A.15) it follows that for given Z_1 and Z_2 there is only a limited range of m-values for which equilibrium cross-sectional areas exist; see expressions for $m_{\min}$, Eq. (3.13), and $m_{\max}$, Eq. (3.14). In the following the effect of varying m on A_k^{eq}, ζ_b^{eq}, φ^{eq} and ψ_k^{eq} is investigated, where it is assumed that $Z_1 > Z_2$. To show the effect on A_k^{eq}, values of A_k^{eq} are evaluated for $m = m_{\min}$ and $m = m_{\max}$. As explained in Appendix 3.A.2, $m = m_{\min}$ corresponds to $|\cos\psi_1^{eq}| = 1$ and thus $\sin\psi_1^{eq} = 0$. It then follows from Eq. (3.A.12) that A_k^{eq} goes to infinity. For $m = m_{\max}$ and $k = 2$ the term between square brackets in Eq. (3.A.12) is zero and thus $A_2^{eq} = 0$. The value of A_1^{eq} is positive and finite. Furthermore, it follows from Eq. (3.A.12) that, with $\cos\psi_1$ positive, $A_1^{eq} > A_2^{eq}$.

To evaluate the effect of varying m on ζ_b^{eq}, φ^{eq} and ψ_k^{eq} the trial solutions, Eqs. (3.A.4) and (3.A.5), and open boundary condition, Eq. (3.A.3), are substituted in Eq. (3.A.1). The real and imaginary parts of the resulting equation are

$$\Re: \quad cmU_{eq}U_k \cos\psi_k = Z_k - Z_b \cos\varphi, \tag{3.A.16a}$$

$$\Im: \quad cmU_{eq}U_k \sin\psi_k = -Z_b \sin\varphi. \tag{3.A.16b}$$

Squaring and adding Eqs. (3.A.16a) and (3.A.16b) and substituting $U_k = U_{eq}$ results in

$$(cm)^2 U_{eq}^4 = \left(Z_k - Z_b^{eq} \cos \varphi^{eq}\right)^2 + (Z_b^{eq})^2 \sin^2 \varphi^{eq}. \tag{3.A.17}$$

Subtracting the equations for $k = 1$ and $k = 2$ yields

$$Z_1 - Z_b^{eq} \cos \varphi^{eq} = \pm(Z_2 - Z_b^{eq} \cos \varphi^{eq}). \tag{3.A.18}$$

Because of the assumption $Z_1 > Z_2$ the positive variant of Eq. (3.A.18) is not possible. Therefore, from (3.A.18) it follows that

$$Z_b^{eq} \cos \varphi^{eq} = \frac{Z_1 + Z_2}{2}. \tag{3.A.19}$$

Substituting for $Z_b^{eq} \cos \varphi^{eq}$ in Eq. (3.A.17) yields

$$(cm)^2 U_{eq}^4 = \left(\frac{\Delta Z}{2}\right)^2 + (Z_b^{eq})^2 \sin^2 \varphi^{eq}. \tag{3.A.20}$$

With the expression for $m_{\min}$ (Eq. 3.13), it follows from Eq. (3.A.20) that $\sin \varphi^{eq} = 0$ and, thus, with φ^{eq} in the fourth quadrant $\varphi^{eq} = 0$. It then follows from Eq. (3.A.19) that

$$Z_b^{eq} = \frac{Z_1 + Z_2}{2}. \tag{3.A.21}$$

With $m = m_{\min}$, the water level in the basin lies between the two ocean water levels. Using Eqs. (3.A.13) and (3.13), the phase angles of the velocity are $\psi_1^{eq} = 0$ and $\psi_2^{eq} = \pi$. Summarizing, for $m = m_{\min}$, Z_b^{eq} is given by Eq. (3.A.21), $\varphi^{eq} = 0$, $U_k = U_{eq}$, $\psi_1^{eq} = 0$ and $\psi_2^{eq} = \pi$.

Eliminating φ^{eq} between Eqs. (3.A.19) and (3.A.20) results in

$$(Z_b^{eq})^2 = (cm)^2 U_{eq}^4 + Z_1 Z_2, \tag{3.A.22}$$

and thus Z_b^{eq} increases with increasing values of m. It then follows from Eq. (3.A.19) that $\cos \varphi^{eq}$ decreases. With φ^{eq} in the fourth quadrant this implies decreasing values of φ^{eq} for increasing values of m. The basin tide increasingly lags the ocean tide. From (3.A.13) and with ψ_1^{eq} in the first quadrant it follows that for increasing values of m, ψ_1^{eq} increases and, with $\psi_2^{eq} = \pi - \psi_1^{eq}$, ψ_2^{eq} decreases. Summarizing, for increasing values of m, Z_b^{eq} and ψ_1^{eq} increase and φ^{eq} and ψ_2^{eq} decrease.

3.B Entrance/Exit Losses and Bottom Friction

This appendix explains the change in the range of m-values for which there are stable equilibriums when in addition to entrance/exit losses bottom friction is included in the dynamic equations. The shift in the lower limit of m can be explained realizing that in the neighbourhood of $m = m_{\min}$ the equilibrium cross-sectional areas A_1^{eq} and A_2^{eq} are large and thus bottom friction is small. From this it is concluded that in the neighbourhood of $m = m_{\min}$ bottom friction has little effect on the basin level and thus on the water level difference between ocean and basin when the system is in equilibrium. Writing Eq. (3.15) for equilibrium conditions results in

$$c\left(m + \frac{2FL}{\gamma\sqrt{A_k^{eq}}}\right) U_{eq}^2 = (\hat{\zeta}_k - \hat{\zeta}_b)^{eq}. \tag{3.B.1}$$

With the right-hand side being the same with and without bottom friction it then follows that for a given equilibrium state adding bottom friction requires that the entrance/exit losses decrease and thus the value of m decreases.

In explaining the downward shift of the maximum m-value the amount of bottom friction that is added is assumed to be small compared to the entrance/exit losses. In that case it is reasonable to assume that in the neighbourhood of $m = m_{\max}$ the qualitative behaviour of Z_b^{eq}, A_1^{eq} and A_2^{eq} as a function of m is the same as in the absence of bottom friction, i.e. Z_b^{eq} increases and A_2^{eq} decreases with increasing values of m and $A_1^{eq} \gg A_2^{eq}$.

When including bottom friction the governing equations for inlet 1 and 2 are respectively

$$cU_{eq}\left(m + \tfrac{2FL}{\gamma\sqrt{A_1}}\right) u_1 = \zeta_1 - \zeta_b, \tag{3.B.2}$$

$$cU_{eq}\left(m + \tfrac{2FL}{\gamma\sqrt{A_2}}\right) u_2 = \zeta_2 - \zeta_b. \tag{3.B.3}$$

Substituting the trial solutions for ζ_b and u_k, respectively Eqs. (3.A.4) and (3.A.5), separating into real and imaginary parts and, subsequently, squaring and adding these parts results in

$$(cU_{eq})^2\left(m + \frac{2FL}{\gamma\sqrt{A_1}}\right)^2 U_1^2 = Z_1^2 + Z_b^2 - 2Z_1Z_b\cos\varphi, \tag{3.B.4}$$

$$(cU_{eq})^2\left(m + \frac{2FL}{\gamma\sqrt{A_2}}\right)^2 U_2^2 = Z_2^2 + Z_b^2 - 2Z_2Z_b\cos\varphi. \tag{3.B.5}$$

Writing Eqs. (3.B.4) and (3.B.5) for equilibrium conditions yields

$$c^2 U_{eq}^4 \left(m + \frac{2FL}{\gamma \sqrt{A_1^{eq}}} \right)^2 = Z_1^2 + (Z_b^{eq})^2 - 2 Z_1 Z_b^{eq} \cos \varphi^{eq}, \tag{3.B.6}$$

$$c^2 U_{eq}^4 \left(m + \frac{2FL}{\gamma \sqrt{A_2^{eq}}} \right)^2 = Z_2^2 + (Z_b^{eq})^2 - 2 Z_2 Z_b^{eq} \cos \varphi^{eq}. \tag{3.B.7}$$

Eliminating $Z_b^{eq} \cos \varphi^{eq}$ between Eqs. (3.B.6) and (3.B.7) the following expression for Z_b^{eq} as a function of m, A_1^{eq} and A_2^{eq} is derived

$$\begin{aligned} (Z_b^{eq})^2 =& (cm)^2 U_{eq}^4 + Z_1 Z_2 + c^2 U_{eq}^4 \left(\frac{Z_2}{Z_2 - Z_1} \right) \left[\frac{4mFL}{\gamma \sqrt{A_1^{eq}}} + \left(\frac{2FL}{\gamma \sqrt{A_1^{eq}}} \right)^2 \right] \\ & - c^2 U_{eq}^4 \left(\frac{Z_1}{Z_2 - Z_1} \right) \left[\frac{4mFL}{\gamma \sqrt{A_2^{eq}}} + \left(\frac{2FL}{\gamma \sqrt{A_2^{eq}}} \right)^2 \right]. \end{aligned} \tag{3.B.8}$$

Making use of $A_1^{eq} \gg A_2^{eq}$, Eq. (3.B.8) is simplified to

$$\begin{aligned} (Z_b^{eq})^2 =& (cm)^2 U_{eq}^4 + Z_1 Z_2 - \\ & c^2 U_{eq}^4 \left(\frac{Z_1}{Z_2 - Z_1} \right) \left[\frac{4mFL}{\gamma \sqrt{A_2^{eq}}} + \left(\frac{2FL}{\gamma \sqrt{A_2^{eq}}} \right)^2 \right]. \end{aligned} \tag{3.B.9}$$

This equation relates m, Z_b^{eq} and A_2^{eq} in the neighbourhood of $m = m_{\max}$ when the system is in equilibrium. The system is perturbed by increasing the value of m by an amount of Δm (with Δm positive) and keeping all other parameters constant. As a result the system is assumed to go to a new equilibrium. The resulting changes in Z_b^{eq} and A_2^{eq} are respectively ΔZ_b and ΔA_2. Here, it is assumed that the perturbations are small compared to the equilibrium values. In Eq. (3.B.9) replacing m by $m^{eq} + \Delta m$, A_2^{eq} by $A_2^{eq} + \Delta A_2$ and Z_b^{eq} by $Z_b^{eq} + \Delta Z_b$ results in an equation relating m^{eq}, Z_b^{eq} and A_2^{eq} for a new equilibrium. This equation can be further simplified by expanding $1/\sqrt{A_2^{eq}}$ in a Taylor series and only considering terms of perturbed order, i.e. Δm, ΔZ_b and ΔA_2. The result is

$$\Delta m \cdot 2c^2 U_{eq}^4 \left[m^{eq} \left(\frac{Z_1 - Z_2}{Z_1} \right) + \frac{2FL}{\gamma \sqrt{A_2^{eq}}} \right] =$$
$$\Delta Z_b \cdot 2Z_b^{eq} \left[\frac{Z_1 - Z_2}{Z_1} \right] + \tag{3.B.10}$$
$$\Delta A_2 \cdot 2c^2 U_{eq}^4 \left[\frac{m^{eq} FL}{\gamma (A_2^{eq})^{3/2}} + 2 \left(\frac{FL}{\gamma A_2^{eq}} \right)^2 \right].$$

In this equation, the expressions in square brackets are all positive ($Z_1 > Z_2$). Because Z_b^{eq} increases and A_2^{eq} decreases with increasing values of m, ΔZ_b is positive and ΔA_2 is negative. It then follows from Eq. (3.B.10) that for Δm to be positive the term multiplying ΔZ_b has to be larger than the absolute value of the term multiplying ΔA_2, which is only possible for $A_2^{eq} > 0$. In turn, this implies that in the presence of bottom friction the maximum value of m for which equilibrium is possible is smaller than $m_{\max}$.

3.C Linear Stability Entrance/Exit Losses Only

In this appendix the linear stability of the equilibrium for entrance/exit losses only, as summarised in Section 3.3, is discussed in detail. Linear stability is investigated by considering Eq. (3.1), which determines the rate of change of the equilibrium after a perturbation:

$$A_k = A_k^{eq} + \Delta A_k. \tag{3.C.1}$$

Here, it is assumed that the equilibrium value is much larger than the perturbation, i.e. $A_k^{eq} \gg \Delta A_k$. Next, the system of Eq. (3.1) for $k = 1, 2$ is linearised around the equilibrium solution (i.e. only terms linear in the perturbation are retained). Therefore, the amplitude of the inlet velocity U_k , Eq. (3.7), is linearised. The first order Taylor expansion for U_k around the equilibrium solution has the form

$$\begin{aligned} U_k(A_1, A_2) &= U_k^{eq} + \Delta U_k \\ &= U_k(A_1^{eq}, A_2^{eq}) + \Delta A_1 \frac{\partial U_k}{\partial A_1}\Big|_{(A_1,A_2)} + \Delta A_2 \frac{\partial U_k}{\partial A_2}\Big|_{(A_1,A_2)}, \end{aligned} \tag{3.C.2}$$

where

$$\begin{aligned} \frac{\partial U_k}{\partial A_1}\Big|_{(A_1,A_2)} = &- \frac{1}{cmU_{eq}} \sqrt{\frac{(\mu m U_{eq} Z_k)^2 + (A_2)^2 (Z_1 - Z_2)^2}{(\mu m U_{eq})^2 + (A_1 + A_2)^2}} \cdot \\ &\left(\frac{A_1 + A_2}{(\mu m U_{eq})^2 + (A_1 + A_2)^2} \right), \end{aligned} \tag{3.C.3}$$

and

$$\begin{aligned} \frac{\partial U_k}{\partial A_2}\Big|_{(A_1,A_2)} = &\frac{1}{cmU_{eq}} \left(\frac{1}{\sqrt{\frac{(\mu m U_{eq} Z_k)^2 + A_2^2 (Z_1 - Z_2)^2}{(\mu m U_{eq})^2 + (A_1 + A_2)^2}}} \cdot \right. \\ &\left[\frac{A_2 (Z_1 - Z_2)^2}{(\mu m U_{eq})^2 + (A_1 + A_2)^2} \right] - \\ &\sqrt{\frac{(\mu m U_{eq} Z_k)^2 + A_2^2 (Z_1 - Z_2)^2}{(\mu m U_{eq})^2 + (A_1 + A_2)^2}} \cdot \\ &\left. \left[\frac{A_1 + A_2}{(\mu m U_{eq})^2 + (A_1 + A_2)^2} \right] \right). \end{aligned} \tag{3.C.4}$$

Here, $c = 4/(3\pi g)$ and $\mu = c\omega B$. Using Eq. (3.C.1) and considering only terms of perturbed order ΔA_k, it follows that:

$$\begin{aligned}\Delta U_k =& \frac{1}{(cm)^2 U_{eq}^3}\left(\frac{A_{3-k}^{eq}(Z_1-Z_2)^2}{(\mu m U_{eq})^2+(A_1^{eq}+A_2^{eq})^2}\right)\Delta A_{3-k} - \\ & U_{eq}\left(\frac{A_1^{eq}+A_2^{eq}}{(\mu m U_{eq})^2+(A_1^{eq}+A_2^{eq})^2}\right)(\Delta A_1+\Delta A_2).\end{aligned} \tag{3.C.5}$$

With $U_k = U_k^{eq} + \Delta U_k$ the expression for $dA_k(U_k)/dt$ (Eq. 3.1) can be written as

$$\frac{dA_k}{dt}(U_k) = \frac{M}{L}\left(1 + 3\frac{\Delta U_k}{U_{eq}} + \mathcal{O}(\Delta U_k^2)\right) \tag{3.C.6}$$

Considering only terms of perturbed order ΔU_k and substituting Eq. (3.C.5) in Eq. (3.C.6) results in:

$$\begin{aligned}\left.\frac{dA_k}{dt}\right|_{\Delta A_k} = \frac{3M}{(cm)^2 U_{eq}^4 L}\Bigg(&\frac{A_{3-k}^{eq}(Z_1-Z_2)^2\Delta A_{3-k}}{(\mu m U_{eq})^2+(A_1^{eq}+A_2^{eq})^2} - \\ &\frac{(cm)^2 U_{eq}^4 (A_1^{eq}+A_2^{eq})(\Delta A_1+\Delta A_2)}{(\mu m U_{eq})^2+(A_1^{eq}+A_2^{eq})^2}\Bigg).\end{aligned} \tag{3.C.7}$$

With $\Delta A_k = \tilde{A}_k e^{\lambda t}$ the eigenvalue problem for $\tilde{A}_k$ can now be written as

$$\lambda\begin{bmatrix}\tilde{A}_1\\ \tilde{A}_2\end{bmatrix} = \begin{bmatrix}-\kappa\xi & \kappa(\sigma_1-\xi)\\ \kappa(\sigma_2-\xi) & -\kappa\xi\end{bmatrix}\begin{bmatrix}\Delta A_1\\ \Delta A_2\end{bmatrix}, \tag{3.C.8}$$

with

$$\begin{aligned}\kappa &= \frac{3M}{(cm)^2 U_{eq}^4 L}\left(\frac{1}{(\mu m U_{eq})^2+(A_1^{eq}+A_2^{eq})^2}\right),\\ \xi &= (cm)^2 U_{eq}^4 (A_1^{eq}+A_2^{eq}),\\ \sigma_k &= A_k^{eq}(Z_1-Z_2)^2.\end{aligned}$$

If $\Re\{\lambda\} > 0$, the equilibrium is unstable as the amplitude of the perturbation increases in time. $\Re\{\lambda\} < 0$ indicates that the equilibrium is stable. The stability of the equilibrium can be deduced from the matrix in (3.C.8) by investigating its trace and the determinant (i.e. without explicitly calculating the eigenvalues), as the trace is equal to the sum of the eigenvalues and the determinant to their

product. Hence, the conditions for a stable equilibrium are a negative trace and a positive determinant. From the matrix in (3.C.8) it follows that the trace is always negative, since ζ and ξ are always positive. In the case of similar forcing amplitudes ($\sigma_1 = \sigma_2 = 0$), the determinant is zero. Hence, one eigenvalue is zero and the other negative. It can thus be concluded that for similar forcing amplitudes there are an infinite number of equilibriums on a straight line which are neutrally stable. If the system is perturbed, it returns to equilibrium, but not necessarily the same equilibrium.

For different forcing amplitudes ($\sigma_1 \neq \sigma_2$) the determinant of the matrix in (3.C.8) is positive provided

$$\frac{A_1^{eq}}{A_2^{eq}} + \frac{A_2^{eq}}{A_1^{eq}} > \frac{(Z_1 - Z_2)^2}{(cm)^2 U_{eq}^4} - 2. \tag{3.C.9}$$

It can be shown that the left-hand side of (3.C.9) is minimal, and equal to 2, if both equilibrium cross-sections are equal. Hence, if $Z_1 - Z_2 < 2cmU_{eq}^2$, the determinant is always positive. From (3.11) it follows that if an equilibrium exists, $Z_1 - Z_2$ is always smaller than $2cmU_{eq}^2$ and, therefore, the determinant of the matrix in (3.C.8) is always positive. As the trace is negative and the determinant positive, the equilibriums given by (3.C.9) are always stable. Summarizing, for different forcing amplitudes and provided that an equilibrium exists, this equilibrium is always stable.

4

Double inlet stability by spatially varying water motion*

Abstract The cross-sectional stability of double inlet system is investigated using an exploratory model that combines Escoffier's stability concept for the evolution of the inlet's cross-sectional area with a two-dimensional, depth-averaged (2DH) hydrodynamic model for tidal flow. The model geometry consists of four rectangular compartments, each with a uniform depth, associated with the ocean, two tidal inlets and the basin. The water motion, forced by an incoming Kelvin wave at the ocean's open boundary and satisfying the linear shallow water equations on the f-plane with linearised bottom friction, is in each compartment written as a superposition of eigenmodes, i.e. Kelvin and Poincaré waves. A collocation method is employed to satisfy boundary and matching conditions. The analysis of resulting equilibrium configurations is done using flow diagrams.

Model results show that internally generated spatial variations in the water motion are essential for the existence of stable equilibriums with two inlets open. In the hydrodynamic model used in this chapter, both radiation damping into the ocean and basin bottom friction result in these necessary spatial variations. Cori-

This chapter is based on a paper ("Influence of basin geometry on equilibrium and stability of double inlet systems"* by R.L. Brouwer, H.M. Schuttelaars and P.C. Roos (2012), In: Jubilee Conference Proceedings NCK-days 2012: Crossing borders in coastal research, Enschede, The Netherlands, pp. 85-89.) and on a conference contribution (*"Influence of basin characteristics on equilibrium and stability of double inlet systems"* by R.L. Brouwer, H.M. Schuttelaars, P.C. Roos and J. van de Kreeke (2012), In: Book of abstracts of Physics of Estuaries and Coastal Seas 2012, New York, USA.). It has been submitted to appear in the Topical Collection - PECS 2012 of Ocean Dynamics.

olis effects trigger an asymmetry in the stable equilibrium cross-sectional areas of the inlets. Furthermore, more elongated basin geometries in the inlet-parallel direction generally correspond to significantly larger equilibrium values of the inlet cross-sections. These model outcomes result from a competition between a destabilising (caused by inlet bottom friction) and a stabilising mechanism (caused by spatially varying local pressure gradients over the inlets).

4.1 Introduction

About ten percent of the world's coastline consists of barrier coasts (Glaeser, 1978). They generally display a chain of barrier islands separated by tidal inlets that connect one or more back-barrier basins to an ocean or a coastal sea. The combination of tidal inlet and back-barrier basin is commonly known as a tidal inlet system. Examples are found along the Wadden Sea coast of the Netherlands, Germany and Denmark (see Fig. 1.2), the Ría Formosa in southern Portugal (see Fig. 1.3) and the U.S. east coast. These morphologically dynamic systems are subject to potentially conflicting interests of economy, coastal safety and ecology.

To manage these different interests, it is important to understand the long-term morphological evolution of these inlet systems and their adaptation to natural changes (e.g., sea level rise, storm-induced barrier island breaching) and human interventions (e.g., basin reduction, dredging activities, inlet relocation). For example, the closure of the Zuiderzee (now called Lake IJssel) in the northwest of the Netherlands in 1932 induced extensive morphological changes in the Dutch Wadden Sea that are still felt today (for more details see, e.g., Elias et al., 2003). An example of barrier island breaching occurred recently along the south shore of Long Island (NY) where Hurricane Sandy created three breaches on Fire Island, which led to (expensive) measures to close them again (National Park Service, 2012).

The stability properties of these systems can be inferred from the morphological evolution of the cross-sectional area of the tidal inlets. For single inlet systems in equilibrium, various empirical relationships exist between the inlet's cross-sectional area A and ebb-tidal prism P (e.g. LeConte, 1905; O'Brien, 1931; Jarrett, 1976). Alternatively, Escoffier (1940) related the equilibrium cross-sectional area to a balance between the wave-driven import of sediment and the tide-driven sediment export, resulting in the definition of an equilibrium velocity U_{eq}. If the ebb-tidal inlet velocity amplitude U is larger than the equilibrium velocity, $U > U_{eq}$, the inlet's cross-sectional area increases (erodes), and if $U < U_{eq}$ it decreases (accretes). An equilibrium is considered stable, when after being perturbed, the cross-sectional area returns to its original equilibrium value. To calculate the amplitude of the inlet velocity, Escoffier used a simple hydrodynamic model (Brown, 1928) that assumes a uniformly fluctuating surface elevation in the basin, and prescribed a sinusoidal forcing at the seaside. In general,

one stable and one unstable equilibrium cross-sectional area exist (see Fig. 1.4 on page 10).

van de Kreeke (1990a) extended Escoffier's stability concept to double inlet systems, taking the Pass Cavallo-Matagorda Inlet system on the US Gulf coast as an example. For these systems, an equilibrium is considered stable, when after being perturbed, the cross-sectional areas of both inlets return to their original equilibrium values. Similarly to Escoffier (1940), in his model schematisation the surface elevation in the basin was also assumed to fluctuate uniformly. Considering a balance between bottom friction in the inlets and the pressure gradient over the inlet, he concluded that only unstable equilibriums exist, i.e. one inlet closes and the other remains open. This model result contradicts observations in, for instance, the Dutch Wadden Sea (Louters & Gerritsen, 1994) and the Portuguese Ría Formosa (Salles et al., 2005) where tidal inlet systems with more than one inlet connecting the back-barrier basin to the ocean are stable on a historical time scale ($\sim$centuries). This inconsistency between model results and observations is probably due to the too-restrictive assumption of a uniformly fluctuating basin surface elevation: Escoffier (1977) already suggested that spatial variations in basin surface elevation may lead to stable configurations with more than one inlet open. In Chapters 2 (see also de Swart & Volp, 2012) and 3 it was shown that accounting for these spatial variations explicitly, by implementing a topographic high in the basin schematisation, or parametrically, by including entrance/exit losses in the dynamic equation, stable equilibrium configurations with more than one inlet open could be found. However, in these chapters the (sub-)basin surface elevation was still assumed to fluctuate uniformly, neglecting effects of basin bottom friction and geometry. In addition, the forcing off the inlets was prescribed, thereby neglecting the influence of the inlet system on the hydrodynamics on the seaward side of the tidal inlets: this interaction will influence the surface elevations off the inlets by waves radiating away from the inlet into the ocean (radiation damping). Finally, Coriolis effects have been omitted so far, which are also likely to influence the surface elevations in ocean, inlets and basin.

To scrutinise Escoffier's (1977) suggestion, this chapter aims to investigate the influence of a spatially varying water motion on the cross-sectional stability of double inlet systems. In particular, the individual contributions of basin bottom friction, radiation damping and Coriolis effects are examined. Therefore, Escoffier's concept of inlet stability is combined with a 2DH hydrodynamic model (see Taylor, 1920; Godin, 1965; Roos & Schuttelaars, 2011; Roos et al., 2011) based on the linear shallow water equations in an idealised, rotating geometry consisting of ocean, tidal inlets and basin.

This chapter is organised as follows. In the following section the new 2DH model and solution method will be presented. Subsequently, in Section 4.3 the water motion for a rotating double inlet system is discussed, as well as the influence of radiation damping, basin bottom friction and Coriolis effects on the cross-sectional stability of double inlet systems. In addition, the effect of different

basin geometries is examined. Finally, Sections 4.4 and 4.5 contain the discussion and conclusions, respectively.

4.2 Model and method

4.2.1 Cross-sectional stability

In this study the focus is on cross-sectional stability of double inlet systems. Following Escoffier (1940) an inlet is assumed to be in equilibrium if the amplitude of the cross-sectionally averaged inlet velocity U_p is equal to the so-called equilibrium velocity U_{eq}, generally taken as 1 m s^{-1} (Bruun et al., 1978). This equilibrium velocity is defined as the amplitude of the tidal current that is just sufficient to flush the sediment carried into the inlet by the wave-induced alongshore current. Hence, inlets are in equilibrium (assuming average weather conditions as opposed to storm conditions) if there is a balance between the volume of sediment entering and leaving the inlet. van de Kreeke (2004) defined the volume of sediment entering the inlet as a constant fraction of the littoral drift, while the volume leaving the inlet is taken proportional to a power of the ebb tidal velocity amplitude. It is assumed that the inlet accretes uniformly over its entire length if the difference between the amount of sediment that enters and leaves the inlet during a tidal cycle is positive. Similarly, the inlet erodes if this difference is negative. Hence, sediment exchange between inlet and basin is assumed to be negligible. Under these assumptions, the rate of change of the cross-sectional area of Inlet k ($k = 1, 2$) can be written as (van de Kreeke, 1998)

$$\frac{dA_k}{dt} = \frac{M}{L_k}\left[\left(\frac{U_k}{U_{eq}}\right)^n - 1\right], \qquad k = 1, 2. \tag{4.1}$$

Here, A_k is the cross-sectional area of Inlet k (m^2); t is time (s); L_k is the length of Inlet k (m); M is the sediment import (a constant fraction of the littoral drift) (m^3 yr^{-1}); U_k is the cross-sectionally averaged velocity amplitude of Inlet k (m s^{-1}); and n is a power whose value depends on the adopted sand-transport law. Here n is assumed to be 3. If $U_k = U_{eq}$, it follows from Eq. (4.1) that $dA_k/dt = 0$. If this is true for both inlets, the inlet system is in equilibrium. The equilibrium is stable when after a small perturbation, both cross-sectional areas return to the original equilibrium values.

4.2.2 Hydrodynamic model formulation

As discussed in the previous section, the response of the inlet's cross-sectional area depends on the amplitude of the cross-sectionally averaged inlet veloci-

Table 4.1: Comparison of classical LP model and 2DH model

Aspect	**LP model**	**2DH model**
Inertia	Yes	Yes
Inlet bottom friction	Yes	Yes
basin bottom friction	No	Yes
Ocean bottom friction	No	Yes
Entrance/exit losses	Yes	No
Radiation damping	No[a]	Yes
Coriolis effects	No	Yes
Forcing	Prescribed[b]	Dynamic result[c]
Basin geometry	Surface area only[d]	Specific length, width and depth

[a]Possibility to include parametrically (see Maas, 1997).
[b]The ocean surface elevation is prescribed externally just outside the inlets.
[c]The model is forced by an incoming Kelvin wave through the open boundary of the ocean compartment. The ocean surface elevation just outside the inlets is a result of the dynamics equations.
[d]Basin is schematised as a basin area only. Hypsometric effects can be included (see de Swart & Volp, 2012).

ties U_k. To obtain U_k, one may apply an analytical or numerical hydrodynamic model. In this chapter, the velocities are calculated using an idealised 2DH hydrodynamic model based on the modelling approach described in Taylor (1920); Godin (1965); Roos & Schuttelaars (2011); Roos et al. (2011). Using this hydrodynamic model, the influence of some of the assumptions made in the description of the hydrodynamics in the more classical lumped-parameter (LP) models (see e.g. van de Kreeke (2004) and Chapters 2 and 3) on the cross-sectional stability of tidal inlets can be investigated. The model extensions, listed in Table 4.1, are:

1. Since the adjacent sea/ocean is contained in the model geometry, the tidal wave travelling past the inlet system is part of the solution. This implies that the amplitude and phase differences between the two inlets are not prescribed externally but follow from the model.
2. Bottom friction in the ocean, inlets and basin is taken into account, thus triggering spatial variations in the water motion.
3. By adopting a two-dimensional model, the ocean, inlets and basin each have a length and width, allowing for a systematic study into the influence of geometries on inlet stability.
4. Coriolis effects are taken into account.

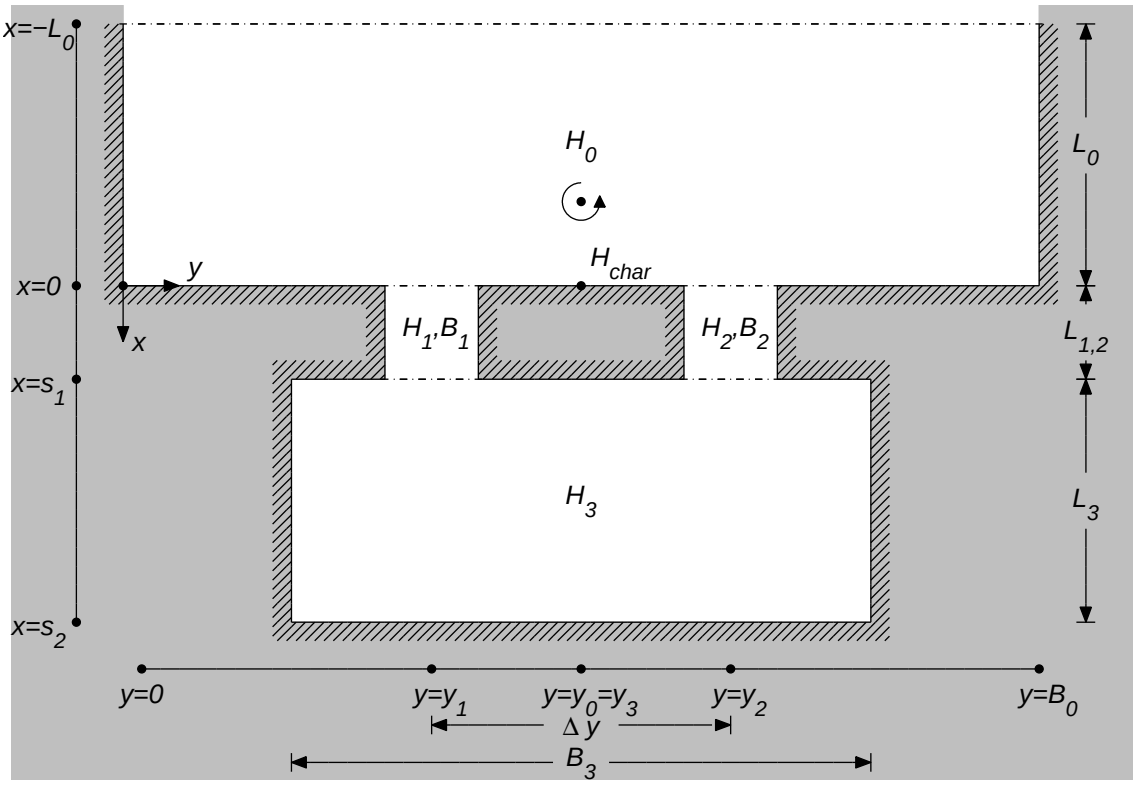

Figure 4.1: Schematisation of the model geometry.

The model calculates tidal elevation and flow in a geometry consisting of four adjacent rectangular compartments constituting a double inlet system (see Fig. 4.1). It consists of four compartments of length L_p, width W_p and (uniform) depth H_p ($p = 0, \ldots, 3$). Compartment 0, which has an open boundary at $x = -L_0$, represents the ocean/sea. Compartment 1 and 2 are two inlet channels of rectangular cross-section and equal length ($L_1 = L_2$). Compartment 3 is the tidal basin. The double inlet system (Compartments 1, 2 and 3) is symmetrically aligned with respect to the central axis y_0 of the ocean compartment. As a result, $y_3 = y_0$ and $|y_1 - y_0| = |y_2 - y_0|$. Furthermore, the distance between the inlets' central axes is defined as $\Delta y = y_2 - y_1$. In each compartment, conservation of momentum and mass is expressed by the linearised depth-averaged shallow water equations on the f-plane:

$$\frac{\partial u_p}{\partial t} - f v_p + \frac{r_p u_p}{H_p} = -g \frac{\partial \zeta_p}{\partial x}, \tag{4.2}$$

$$\frac{\partial v_p}{\partial t} + f u_p + \frac{r_p v_p}{H_p} = -g \frac{\partial \zeta_p}{\partial y}, \tag{4.3}$$

$$\frac{\partial \zeta_p}{\partial t} + H_p \left[\frac{\partial u_p}{\partial x} + \frac{\partial v_p}{\partial y} \right] = 0. \tag{4.4}$$

For Compartment p, $u_p(x, y, t)$ and $v_p(x, y, t)$ are the depth-averaged flow velocity components in the positive x- and y-direction, respectively, and $\zeta_p(x, y, t)$ is the free surface elevation. Furthermore, $g = 9.81$ m s^{-2} is the gravitational acceleration and $f = 2\Omega \sin \vartheta$ is a Coriolis parameter in the northern Hemisphere ($f > 0$), with $\Omega = 7.292 \times 10^{-5}$ rad s^{-1} the angular frequency of the Earth's rotation and ϑ the central latitude of the system. In Eqs. (4.2)-(4.4), r_p is a linear bottom friction coefficient:

$$r_p = \frac{8 F U_p}{3\pi}. \tag{4.5}$$

It is obtained from Lorentz' linearisation of a quadratic friction law (Lorentz, 1926; Zimmerman, 1982) with a default value of the bottom friction coefficient $F = 2.5 \times 10^{-3}$ and typical flow velocity scale U_p. Since velocities will differ per compartment, each compartment is allowed to have a different bottom friction coefficient r_p. Calculating each friction coefficient thus requires an estimate of the flow velocity scale, which is defined as the velocity amplitude averaged over Compartment p. The friction coefficients are obtained using an iterative procedure (for details see Appendix 4.A).

At the closed boundaries a no-normal flow condition is imposed ($u = 0$ or $v = 0$). Across the interfaces between ocean and inlets, and between inlets and basin, continuity of elevation and normal flux is required:

$$\zeta_0 = \zeta_k, \qquad H_0 u_0 = H_k u_k, \tag{4.6}$$

$$\zeta_k = \zeta_3, \qquad H_k u_k = H_3 u_3, \tag{4.7}$$

with $k = 1, 2$. Analogous to the classical Taylor (1920) problem, the system is forced by a single incoming Kelvin wave with angular frequency ω and typical elevation amplitude Z_{M2} entering through the open boundary of the ocean compartment. Due to the Coriolis effect, the Kelvin wave travels along the coast past the two inlets. The reflected Kelvin wave along with other waves generated within the model domain, leave the ocean compartment without reflection.

To solve the problem for ζ_p, u_p and v_p, the solution in each compartment is written as a truncated sum of analytical wave solutions in an infinite channel. Subsequently, a collocation technique is used to satisfy the no-normal flow condition at the closed boundaries as well as the matching conditions (cf. Eqs. (4.6) and (4.7)). For a detailed description of the solution method, the reader is referred to Appendix 4.A.

4.2.3 Flow diagram

To determine the equilibrium cross-sectional areas and their stability properties, the results are shown using so-called flow diagrams (see Section 2.2). A flow diagram plots the cross-sectional area of Inlet 1, A_1, against that of Inlet 2, A_2, and consists of the equilibrium flow curves for both inlets together with a vector plot. The equilibrium flow curve for Inlet 1 represent the locus of (A_1, A_2)-values for which for that inlet $U_1(A_1, A_2) = U_{eq}$ and similarly for Inlet 2, i.e. $U_2(A_1, A_2) = U_{eq}$. Here, the velocities U_1 and U_2 are the cross-sectionally averaged velocity amplitudes, calculated using the hydrodynamic equations, described above, at the transect $x = s_1/2$, i.e. halfway between the basin and the sea, for different combinations of (A_1, A_2). During the calculation of U_1 and U_2 for different combinations of (A_1, A_2), the inlet's cross-sectional areas A_k are assumed to remain geometrically similar (O'Brien & Dean, 1972). Assumed is a rectangular cross-section with a depth to width ratio $H_k/W_k = 0.005$ for both inlets. Hence, the shape factor $\gamma_k = \sqrt{H_k/W_k} \approx 0.07$ is constant for all values of the cross-sectional areas. The intersections of the two curves represent sets of equilibrium cross-sectional areas. To determine the stability of the equilibriums, vectors are added to the flow diagram. These vectors are the unit vectors in the direction of $(dA_1/dt, dA_2/dt)$ calculated from Eq. 4.1. The vectors indicate the system's tendency to evolve, i.e. the direction in which the values of cross-sectional areas change when they are not in equilibrium.

4.3 Model Results

The influence of the various model extensions, compared to the L-P model, on the water motion and equilibrium configuration of a double inlet system will be presented in this section. Default values for the geometry and parameters used in this section are given in Table 4.2. These are based on characteristic values of the Marsdiep-Vlie system in the western Dutch Wadden Sea found in literature and using Google Earth (see also Section 1.3 on page 4). Even though previous studies (e.g. Roos & Schuttelaars, 2011; Roos et al., 2011) using a similar model approach showed that tidal observations at various locations can be well reproduced, it is emphasised that the aim is neither to accurately reproduce the water motion of the Marsdiep-Vlie system, nor to predict its long-term evolution.

The Marsdiep-Vlie system is situated at a latitude of 53°N. To roughly represent its basin surface area a value of $L_3 \times W_3 = 30 \times 40 = 1200$ km^2 is adopted (approximated using Google Earth), with uniform depth $H_3 = 5$ m (e.g. Dastgheib et al., 2008). The inlet compartments have identical dimensions $L_{1,2} \times W_{1,2} = 6 \times 3$ km^2 (Google Earth) and reference depths $H_{1,2} = 15$ m. The inlet spacing is chosen to be $\Delta y = 10$ km, so that different basin geometries can be adopted with the same inlet spacing. The width of the ocean compartment is chosen as $L_0 = 200$ km, such that the tidal wave in front of the inlets closely resembles a Kelvin wave. With an arbitrary length of 50 km, the surface area of the ocean compartment is $L_0 \times W_0 = 50 \times 200$ km^2. Furthermore, an ocean depth H_0 of 20 m is assumed to be representative for the North Sea.

The tide in the area is dominated by the semi-diurnal lunar constituent (M2) with radian frequency $\omega = 1.4 \times 10^{-4}$ s^{-1}. The associated characteristic tidal amplitude for the Marsdiep-Vlie system, $Z_{\text{char}} = 0.8$ m, is defined on the coastline exactly between the two inlets (i.e. at $(x, y) = (0, L_0/2)$ in Fig. 4.1). This value equals the mean tidal amplitude in front of the Marsdiep Inlet, $Z_{\text{Mars}} = 0.7$ m, and Vlie Inlet, $Z_{\text{Vlie}} = 0.9$ m (see Section 1.3 on page 4). To subsequently determine the typical amplitude Z_{M2} of the incoming Kelvin wave (see Section 4.2), the model is run with the ocean compartment only, as if there were no double inlet system connected to it. Consequently, depending on ocean depth and latitude, Z_{M2} can be determined by trial and error so that $Z_{\text{char}} = 0.8$ m. The reason for defining a Z_{char} is to make sure that the forcing of the double inlet system is approximately similar for each combination of parameter values. Hence, model results can be compared with each other.

4.3.1 Water motion

The water motion for the default case is shown in Fig. 4.2. It displays the calculated instantaneous surface elevations and flow velocities at four moments of the tidal cycle. Left panels show the double inlet system with the ocean compartment and right panels only show the double inlet system, i.e. inlets and basin. The ebb phase is indicated by cold colors and the flood phase by warm colors. Notice that the velocity scale in Figs. 4.2b and f is different from the other sub-figures.

Fig. 4.2 shows that surface elevations in the ocean, inlets and basin display significant spatial variations in the order of magnitude of tens of centimetres. In the inlets the spatial variation of the surface elevation is predominantly in the along-channel direction. Furthermore, it follows from Fig. 4.2 that the basin surface elevation constantly lags the ocean surface elevation, resulting in pressure gradients across the tidal inlets.

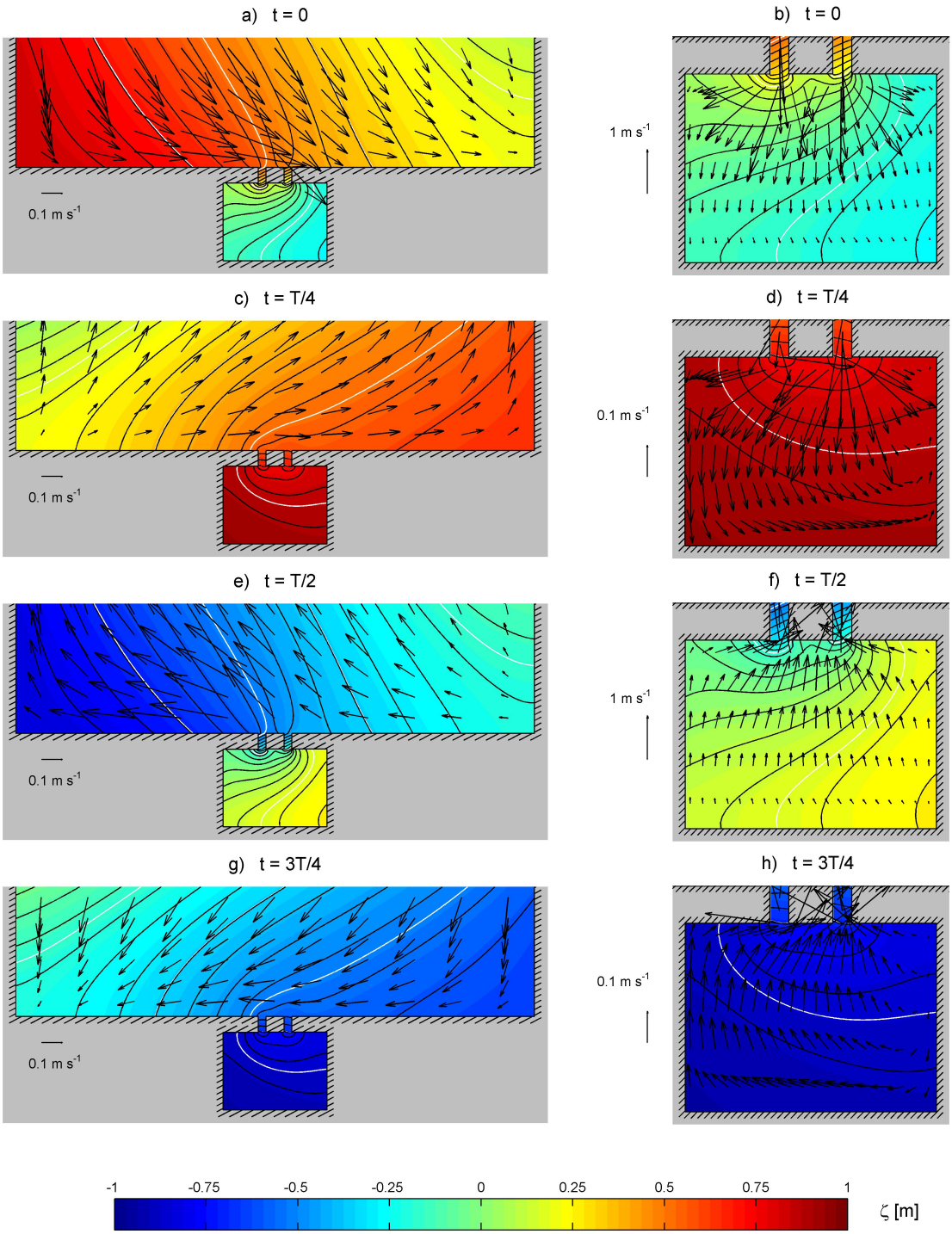

Figure 4.2: Instantaneous surface elevation and flow velocities in a rotating double inlet system connected to an ocean at four moments of the tidal cycle: $t = 0$ (a and b), $t = T/4$ (c and d), $t = T/2$ (e and f) and $t = 3T/4$ (g and h). Here, $T = 2\pi/\omega = 12.42$ hr denotes the tidal period. Surface elevations are in metres, arrows denote flow direction and magnitude, white lines indicate areas with the same phase with intervals of 10° and black lines indicate areas with the same tidal amplitude with intervals of 0.05 m. Default parameter values are listed in Table 4.2.

Table 4.2: Parameter values for the default case (see Fig. 4.3)

Parameter	Symbol	Dimension	Default Value
Compartments			
Ocean length	L_0	km	50
Ocean width	W_0	km	200
Ocean depth	H_0	m	20
Inlet lengths	$L_1 = L_2$	km	6
Inlet widths	$W_1 = W_2$	km	3
Inlet depths	$H_1 = H_2$	m	15
Basin length	L_3	km	30
Basin width	W_3	km	40
Basin depth	H_3	m	5
General			
Central latitude	ϑ	°N	53
Characteristic tidal amplitude	Z_{char}	m	0.8
Radian frequency of the tide	ω	rad s^{-1}	1.4×10^{-4}
Sediment import	M	m^3 yr^{-1}	5×10^5
Equilibrium velocity	U_{eq}	m s^{-1}	1
Inlet shape factor	γ^2	-	5×10^{-3}

4.3.2 Influence of radiation damping, basin bottom friction and Coriolis effects

The results of the previous section clearly show that spatial variations in surface elevation in both ocean and basin are significant. To systematically investigate their influence on the stability of double inlet systems, the various mechanisms that are included in the model formulation resulting in these spatial inhomogeneities will be investigated separately. As a first step, parameters in the 2DH model are chosen such that the characteristics of the LP model used in previous studies (e.g. van de Kreeke, 1985, 1990a,b) and Chapters 2 and 3 are reproduced. Next, additional mechanisms, such as radiation damping, basin bottom friction and Coriolis effects, will be introduced one at a time, and their influence on the cross-sectional stability of double inlet systems will be investigated.

L-P model limit

To approximate the model formulation used in the L-P model as closely as possible, the ocean and basin compartment are assumed to be deep, $H_0 = H_3 = 1,000$ m. As a result, bottom friction effects in the basin and ocean, and radiation damping into the ocean become negligible. Hence, the incoming wave has neither an

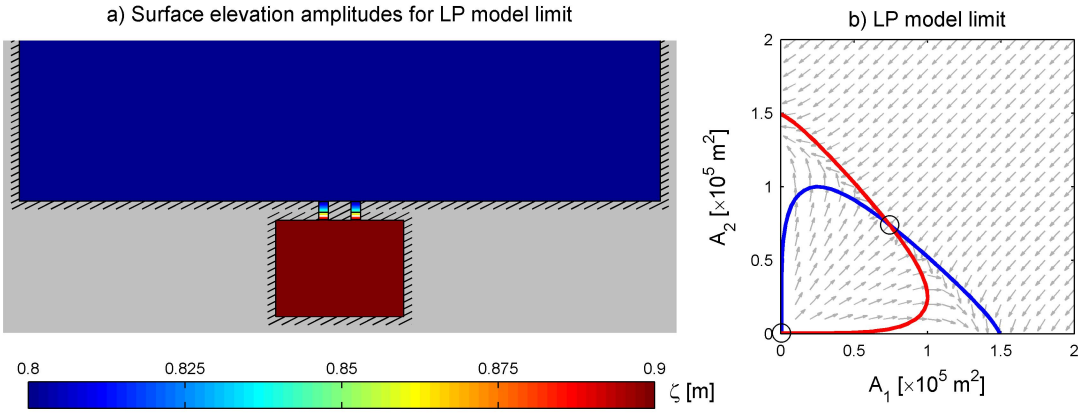

Figure 4.3: a) Surface elevation amplitudes for a double inlet system in the L-P model limit. b) Flow diagram for a double inlet system with inertia and inlet bottom friction only. The green and red line represent the equilibrium flow curve for inlet Compartment 1 and 2, respectively; the blue circle indicates an unstable equilibrium; and the grey arrows indicate the system's tendency when out of equilibrium. In these figures $H_0 = H_3 = 1,000\ m$, $\vartheta = 0$ *and other parameter values are listed in Table 4.2.*

amplitude nor a phase difference between the two inlets. Additionally, the central latitude of the double inlet system is assumed to be located at the equator, i.e. $\vartheta = 0$, thereby omitting Coriolis effects. Other parameter values used are listed in Table 4.2. The resulting surface elevation in ocean and basin are approximately uniform (see Fig. 4.3a). The corresponding flow diagram is presented in Fig. 4.3b.

The flow diagram shows a configuration without stable equilibriums. Hence, ultimately only one inlet remains open and the other closes. Additional calculations (not shown here) with varying inlet lengths L_1 and L_2, inlet shape factor γ and characteristic tidal amplitude Z_{char}, show that the equilibrium configuration might change in shape, but will not yield more than two equilibrium cross-sectional areas. Hence, no stable equilibriums will arise. This result confirms the results by van de Kreeke (1990a): when only bottom friction and pressure gradients are retained in the dynamic inlet equation and assuming a uniformly fluctuating basin surface elevation, at best two combinations of equilibrium cross-sectional areas exist that are both unstable. In addition, Fig.4.3b is in agreement with Figs. 2.4 and 2.8 in Chapter 2 for large cross-sectional areas of the topographic high and Fig. 3.8 in Chapter 3 for an entrance/exit loss coefficient $m = 0$.

Radiation damping

The incoming Kelvin wave induces an oscillatory flow in each inlet, thereby triggering spatially varying co-oscillations in the basin. Simultaneously, the co-oscillations in the basin result in waves radiating away into the ocean (radiation

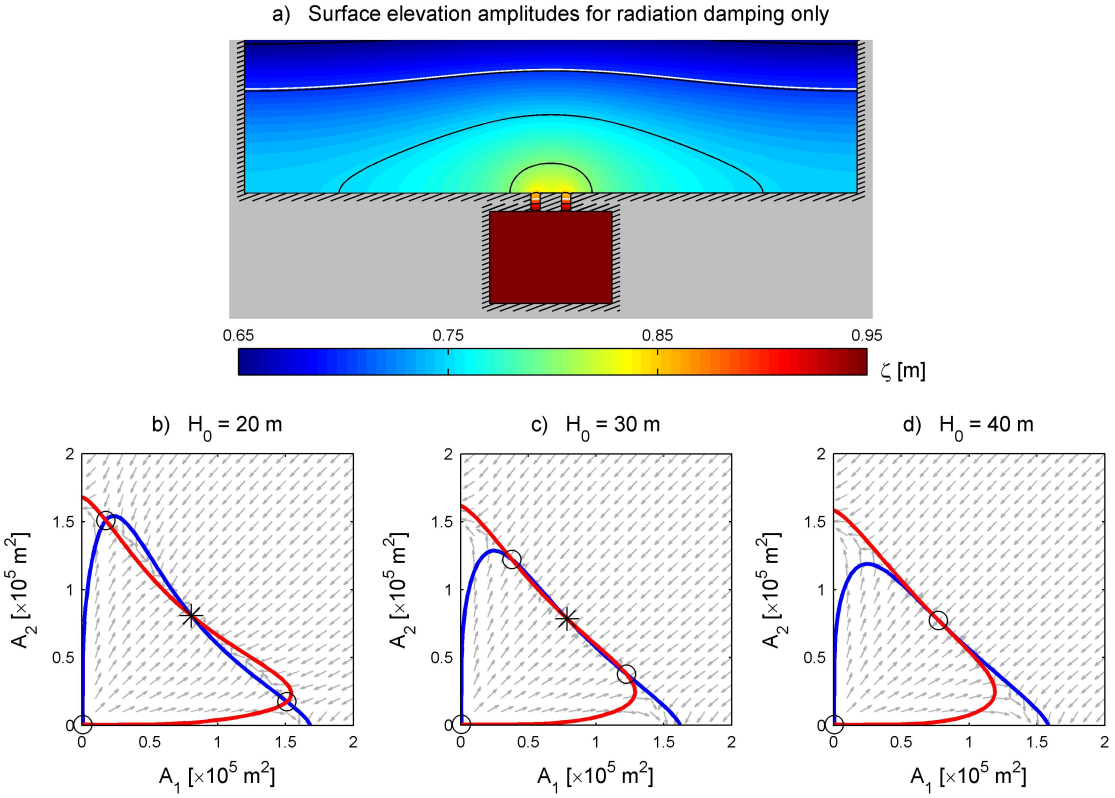

Figure 4.4: a) Surface elevation amplitudes for a double inlet system with radiation damping in the ocean, inertia and inlet bottom friction for $H_0 = 20$ m. Associated flow diagrams are depicted for a) $H_0 = 20$ m, b) $H_0 = 30$ m and c) $H_0 = 40$ m. Furthermore, $L_1 = L_2 = 6$ km, $H_3 = 1,000$ m, $\vartheta = 0$ and other parameter values are listed in Table 4.2.

damping). As a consequence, the surface elevation off each inlet is influenced by waves radiating away from both inlets. Since the effect of radiation damping on surface elevations in the ocean is proportional to the ratio between inlet and ocean depth (see e.g. Eq. 4.2 in Buchwald, 1971), its influence on the cross-sectional stability of double inlet systems can be investigated by considering three different ocean depths: $H_0 = 20$ m, $H_0 = 30$ m and $H_0 = 40$ m. The basin depth and the central latitude are chosen equal to the L-P limit, i.e. $H_3 = 1,000$ m and $\vartheta = 0$, respectively. Since a shallow ocean implies that radiation damping into the ocean affects surface elevations, (symmetric) inhomogeneities in the water motion are observed in the ocean. On the other hand, the surface elevation in the basin is approximately uniform (see Fig. 4.4a). The flow diagrams for ocean depths $H_0 = 20$ m, $H_0 = 30$ m and $H_0 = 40$ m are shown in Figs. 4.4b, c and d, respectively.

Fig. 4.4b shows that for $H_0 = 20$ m a stable equilibrium exists; there are four equilibrium cross-sectional areas, one of which is stable. Hence, there is an equilibrium situation where both inlets are open. Increasing H_0 to 30 m

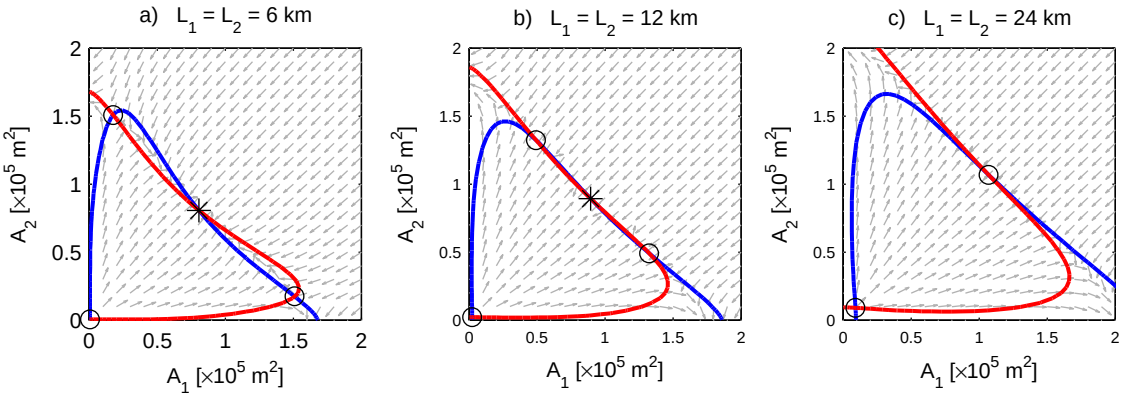

Figure 4.5: Flow diagrams for a double inlet system with radiation damping in the ocean, inertia and inlet bottom friction for a) $L_1 = L_2 = 6$ km, b) $L_1 = L_2 = 12$ km and c) $L_1 = L_2 = 24$ km. Furthermore, $H_0 = 20$ m, $H_3 = 1{,}000$ m, $\vartheta = 0$ and other parameter values are listed in Table 4.2.

(Fig. 4.4c), the stable equilibrium still exists, but the two unstable equilibriums (excluding the one near the origin) have moved considerably closer to the stable equilibrium. Eventually, for $H_0 = 40$ m (Fig. 4.4d), the stable equilibrium has disappeared (in fact, has merged with the two unstable equilibriums) and only two unstable equilibrium cross-sectional areas remain; ultimately one of the inlets will close while the other remains open. In addition, from the flow diagrams in Fig. 4.4 it follows that the set of stable equilibrium cross-sectional areas slightly decrease from $(A_1^{eq}, A_2^{eq}) \approx (0.81 \times 10^5, 0.81 \times 10^5)$ for $H_0 = 20$ m to $(A_1^{eq}, A_2^{eq}) \approx (0.79 \times 10^5, 0.79 \times 10^5)$ for $H_0 = 30$ m and disappears between $H_0 = 30$ m and $H_0 = 40$ m. The gradual disappearance of the stable equilibrium in Fig. 4.4b and c to 4.4d implies that for increasing ocean depth the radiation damping mechanism becomes weaker.

Besides the ratio between inlet and ocean depth, also the inlet length determines the strength of the radiation damping mechanism (see e.g. Maas, 1997; Miles, 1948; Garrett, 1975). It turns out that the radiation damping mechanism is inversely proportional to the inlet length. Hence, this contribution loses importance with increasing inlet length. This sensitivity is shown in Fig. 4.5, which shows flow diagrams for inlet lengths $L_1 = L_2 = 6$ km (Fig. 4.5a), $L_1 = L_2 = 12$ km (Fig. 4.5b) and $L_1 = L_2 = 24$ km (Fig. 4.5c). The ocean depth is taken to be 20 m. These figures indeed show that radiation damping loses importance for increasing inlet lengths, which can be inferred from the disappearing stable equilibrium between $L_1 = L_2 = 12$ km (Fig. 4.5b) and $L_1 = L_2 = 24$ km (Fig. 4.5c). Furthermore, the stable equilibrium cross-sectional areas increase for increasing inlet lengths from $(A_1^{eq}, A_2^{eq}) \approx (0.81 \times 10^5, 0.81 \times 10^5)$ for $L_1 = L_2 = 6$ km to $(A_1^{eq}, A_2^{eq}) \approx (0.89 \times 10^5, 0.89 \times 10^5)$ for $L_1 = L_2 = 12$ km.

The results in this subsection suggest that radiation damping may be an im-

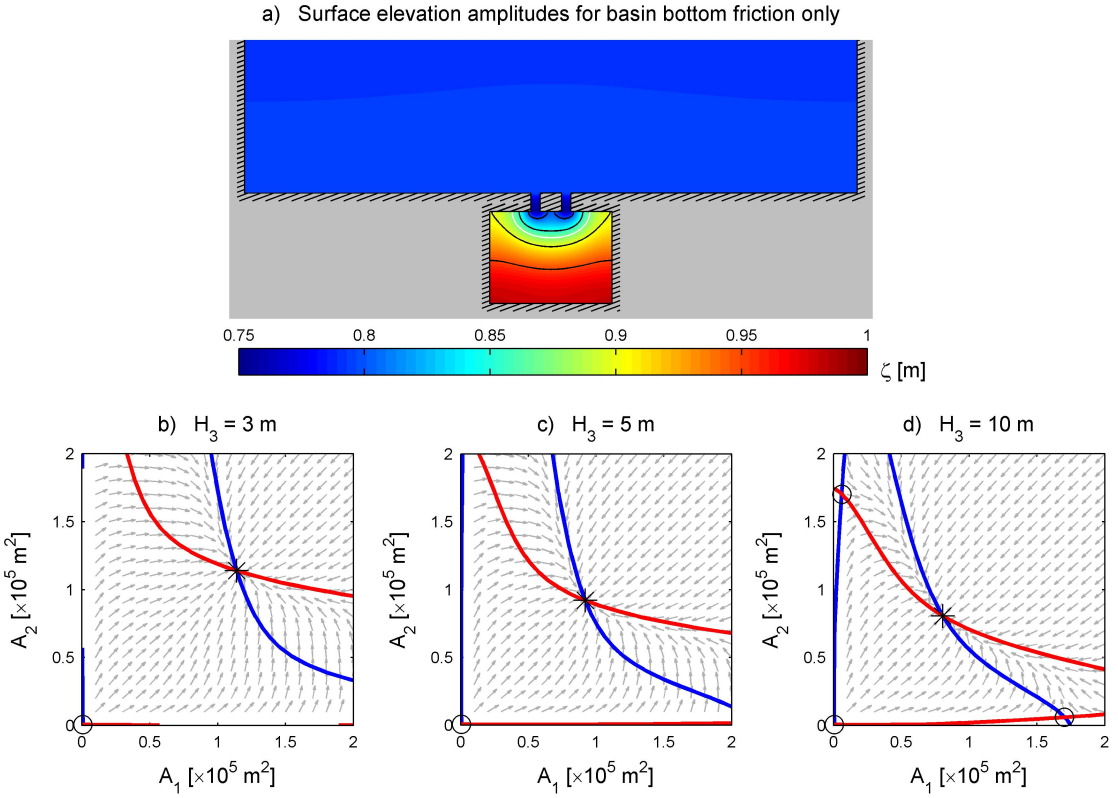

Figure 4.6: a) Surface elevation amplitudes for a double inlet system with basin bottom friction, inertia and inlet bottom friction for $H_3 = 5$ m. Associated flow diagrams are depicted for a) $H_3 = 3$ m, b) $H_3 = 5$ m and c) $H_3 = 10$ m. Furthermore, $H_0 = 1{,}000$ m, $L_1 = L_2 = 6$ km, $\vartheta = 0$ and other parameter values are listed in Table 4.2.

portant mechanism in determining the cross-sectional stability of double inlet systems. Depending on, among others, the inlet length and the ratio between inlet and ocean depth it might result in a stable equilibrium configuration. However, the exact way in which radiation damping contributes to the existence of a stable equilibrium configuration is beyond the scope of this thesis.

Basin bottom friction

The effect of bottom friction on the cross-sectional stability of double inlet systems is investigated by only reducing the depth of the basin with respect to the L-P model limit. Three depths are considered: $H_3 = 3$ m, $H_3 = 5$ m and $H_3 = 10$ m. The ocean depth and the central latitude are still equal to the L-P limit, i.e. $H_0 = 1{,}000$ m and $\vartheta = 0$, respectively. Since only basin bottom friction is considered, spatial variations in the water motion are observed inside the basin, whereas the surface elevation in the ocean is approximately uniform (see Fig. 4.6). The flow diagrams corresponding with the different depths are shown in Fig. 4.6a, b and c.

From Fig. 4.6 it follows that basin bottom friction triggers a stabilising mechanism. All flow diagrams in Fig. 4.6 show an equilibrium configuration with one stable equilibrium with two inlets open. For $H_3 = 3$ m, $H_3 = 5$ m and $H_3 = 10$ m, the stable set of equilibrium cross-sectional areas (A_1^{eq}, A_2^{eq}) is approximately $(1.14 \times 10^5, 1.14 \times 10^5)$, $(0.92 \times 10^5, 0.92 \times 10^5)$ and $(0.81 \times 10^5, 0.81 \times 10^5)$, respectively. This shows that stable equilibrium cross-sections are larger for shallower basins.

Coriolis effects

The last mechanism that is considered in the cross-sectional stability of double inlet systems are Coriolis effects. So far, the influence of Coriolis effects on cross-sectional stability of double inlet systems has not been studied. They mainly influence the flow characteristics in the ocean and basin and as a result influence the spatial structure of surface elevations. When, in addition to inertia and inlet bottom friction, only Coriolis effects are included by increasing the central latitude to a (North Sea) value of $\vartheta = 53^\circ N$, calculations show (not depicted here) the same equilibrium configuration as when the double inlet system is situated on the equator (see Fig. 4.3b). This can also be expected as the Rossby radius of deformation, $L_R = \sqrt{gH}/f$, is large for a large depth H and small Coriolis parameter f and therefore Coriolis effects only will not affect the equilibrium configuration.

All mechanisms

The previous subsection concluded that Coriolis effects only will not affect the equilibrium configuration of a double inlet system. However, in the supporting model calculations the ocean and basin depth were assumed to be relatively deep, i.e. $H_0 = H_3 = 1,000$ m, respectively. When these depths are reduced to realistic values, and thus bottom friction plays a significant role, Coriolis effects may have an impact on the equilibrium configuration. Therefore, in this sub-section all mechanisms discussed previously are taken into account, i.e. radiation damping and basin bottom friction. Hence, the ocean and basin depth are assumed to be $H_0 = 20$ m and $H_3 = 5$ m, respectively. Three cases are considered, one where the central latitude of the double inlet system is on the equator, $\vartheta = 0$, one on $\vartheta = 25^\circ N$ and one on the latitude of the Marsdiep-Vlie system, $\vartheta = 53^\circ N$. The corresponding flow diagrams are depicted in Fig. 4.7a, b and c, respectively.

Fig. 4.7 shows that, qualitatively, Coriolis effects do not change the presence of a stable equilibrium configuration. However, quantitatively Coriolis effects introduce an asymmetry in the equilibrium cross-sections. On the equator, $\vartheta = 0$ (Fig. 4.7a), the set of equilibrium cross-sections $(A_1^{eq}, A_2^{eq}) \approx (1.01 \times 10^5, 1.01 \times 10^5)$; for $\vartheta = 25^\circ N$ (Fig. 4.7b), $(A_1^{eq}, A_2^{eq}) \approx (0.99 \times 10^5, 1.02 \times 10^5)$; and for $\vartheta =$

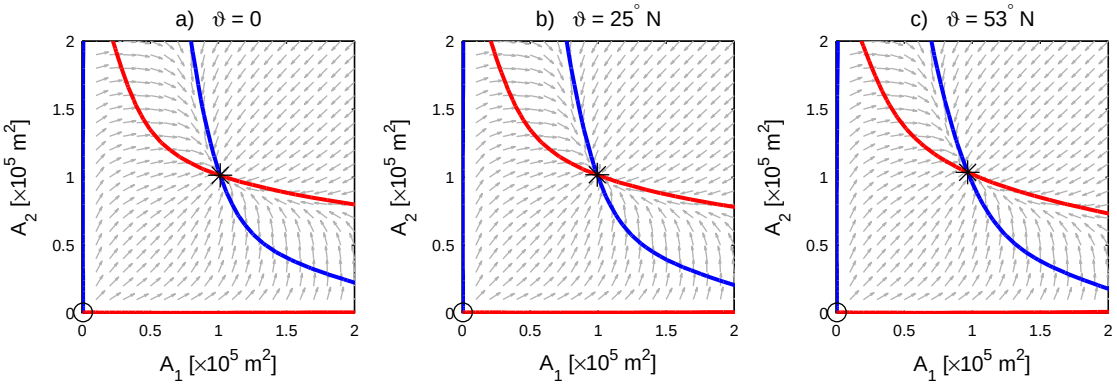

Figure 4.7: Flow diagrams for a double inlet system with radiation damping, basin bottom friction, Coriolis effects, inertia and inlet bottom friction for a) $\vartheta = 0$, b) $\vartheta = 25^{\circ}N$ and c) $\vartheta = 53^{\circ}N$. Other parameter values are listed in Table 4.2.

$53^{\circ}N$ (Fig. 4.7c), $(A_1^{eq}, A_2^{eq}) \approx (0.97 \times 10^5, 1.04 \times 10^5)$. It follows that the smallest stable equilibrium cross-section is observed where the tide arrives first. In the case discussed here (in the northern hemisphere), the cross-sectional area of Inlet 1 is smaller than that of Inlet 2.

In addition, when considering a double inlet system situated on the equator ($\vartheta = 0$), the relative importance of radiation damping and basin bottom friction on the stable equilibrium cross-sectional areas might be assessed by comparing Figs. 4.4b (radiation damping only), 4.6c (basin bottom friction only) and 4.7a (radiation damping and basin bottom friction). The corresponding values of the equilibrium cross-sectional areas are $(A_1^{eq}, A_2^{eq}) \approx (0.81 \times 10^5, 0.81 \times 10^5)$, $(A_1^{eq}, A_2^{eq}) \approx (0.92 \times 10^5, 0.92 \times 10^5)$ and $(A_1^{eq}, A_2^{eq}) \approx (1.01 \times 10^5, 1.01 \times 10^5)$, respectively. From these values it is difficult to suggest whether radiation damping or basin bottom friction is dominant in determining the value of the stable equilibrium cross-sectional area. However, the small difference in appearance between 4.6c and 4.7a after adding radiation damping suggest that basin bottom friction is the more important mechanism in determining the equilibrium configuration of a double inlet system.

4.3.3 Influence of basin geometry on cross-sectional stability

In the previous section the influence of radiation damping, basin bottom friction and Coriolis effects on the cross-sectional stability of double inlet systems was investigated. In calculating the associated flow diagrams to study their influence, a basin geometry of $L_3 \times W_3 = 30 \times 40$ km^2 was assumed. In reality, basin geometries vary between short and wide basins and long and narrow ones. In this

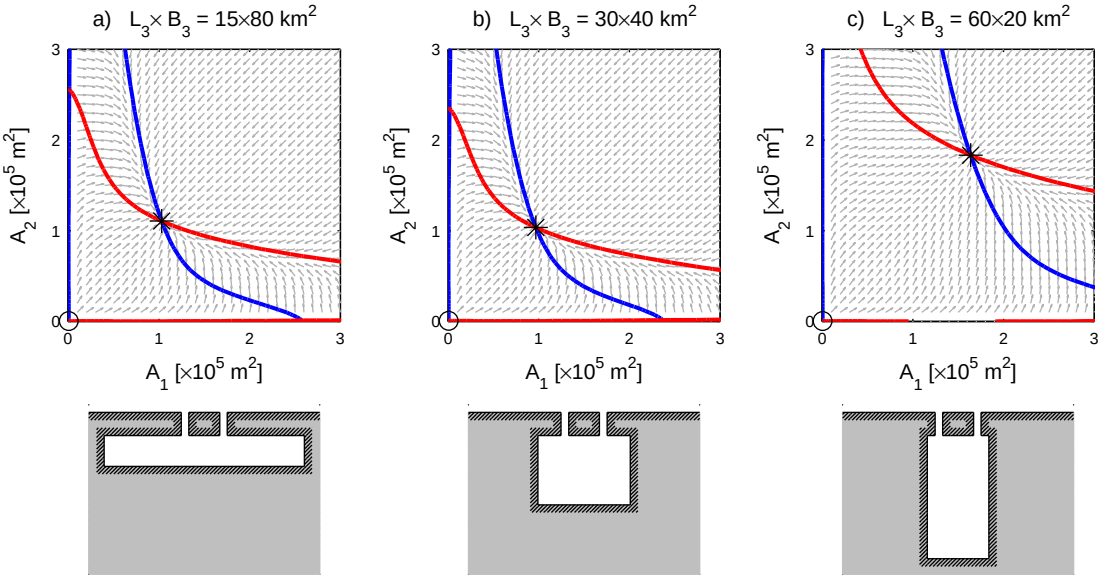

Figure 4.8: Flow diagrams for a double inlet system with basin radiation damping, bottom friction, Coriolis effects, inertia and inlet bottom friction for a) $L_3 \times W_3 = 15 \times 80$ km^2, b) $L_3 \times W_3 = 30 \times 40$ km^2 and c) $L_3 \times W_3 = 60 \times 20$ km^2. Other parameter values are listed in Table 4.2. For clarity the basin geometries are depicted as well.

section the influence of these different geometries on the cross-sectional stability is investigated. To that end, in the calculations the default parameter values denoted in Table 4.2 are used. Furthermore, three basin geometries ($L_3 \times W_3$) are chosen with a constant basin surface area of 1200 km^2: 15×80 km^2, 30×40 km^2 (default case) and 60×20 km^2. For each calculation the centreline of the tidal basin is on the same position as the centreline of the ocean, and the inlet channels are 10 km apart and symmetrically positioned with respect to the centrelines of the ocean and basin. The resulting flow diagrams for each basin geometry are depicted in Fig. 4.8.

From Fig 4.8 it follows that for all three cases next to three unstable equilibriums, a single stable equilibrium exists. In that sense, the basin geometry does not qualitatively change the presence of a stable equilibrium configuration. Quantitatively, however, the influence of basin geometry has a large influence on the equilibrium values of the cross-sectional areas. The largest equilibrium values are found for the 60×20 km^2 geometry in Fig. 4.8c, i.e. $(A_1, A_2) \approx (1.64 \times 10^5, 1.83 \times 10^5)$. The other basin shapes lead to smaller equilibrium values (Figs. 4.8a and b): $(A_1, A_2) \approx (1.03 \times 10^5, 1.11 \times 10^5)$ for the 15×80 km^2 geometry and $(A_1, A_2) \approx (0.97 \times 10^5, 1.04 \times 10^5)$ for the 30×40 km^2 geometry, respectively. This leads to a difference in stable equilibrium cross-sectional areas up to a factor of approximately 2 depending on the geometry of the basin.

The results presented in this section show a discrepancy with preliminary results with the same model in Brouwer et al. (2012). In that paper, the opposite

was concluded with regards to which basin geometry displays the largest stable equilibrium inlet cross-sections, i.e. the largest set of stable cross-sections was found for the basin geometry $L_3 \times W_3 = 30 \times 40$ km^2 and for more elongated basin geometries these stable cross-sections were significantly smaller. However, in these preliminary results the typical velocity scales for all the compartments were based on the current amplitude of a classical Kelvin wave without bottom friction: $U_p = Z_{M2}\sqrt{g/H_p}$. In the inlet compartments this current amplitude significantly under- or overestimates the typical velocity scale depending on the inlet cross-sectional area and thus inlet depth. In the basin compartment it significantly overestimates the typical velocity scale. Therefore, an iterative procedure has to be adopted, leading to realistic velocity scales for inlet and basin compartments.

4.4 Discussion

Based on the model results in this chapter, Roos et al. (2013, submitted) developed a new exploratory morphodynamic model that revealed an explanation for the (non-)existence of stable double inlet systems with two inlets open. This explanation is based on a competition between a destabilising and a stabilising mechanism. The first one is associated with bottom friction in the inlets. Because bottom friction depends on depth and therefore on the inlet's cross-sectional area, perturbations from the equilibrium cross-sectional area tend to amplify, thus acting as a destabilising mechanism. The second mechanism concerns the system's feedback to the local pressure gradients over the inlets. As it turns out, these local pressure gradients counteract the destabilising flow response from bottom friction alone, thus acting as a stabilising mechanism. Furthermore, they concluded that for stable double (or multiple) inlet systems to exist, this pressure gradient induced stabilising mechanism requires surface elevations in the basin and ocean to vary in space.

The results presented in this chapter support the above explanation for the (in)stability of double inlet systems with a model that includes more details in the inlet flow and physics by taking Coriolis effects and ocean bottom friction into account. Assuming a deep ocean and basin (lumped-parameter limit), hence retaining only bottom friction in the inlets, Fig. 4.3 shows that no stable equilibriums with two inlets open exist. The same results were obtained by van de Kreeke (1990a) who used a lumped-parameter model with essentially the same assumptions. According to Roos et al. (2013, submitted), the local pressure gradient over the inlets associated with a uniformly fluctuating basin surface elevation is not sufficient to counteract the flow response from inlet bottom friction alone.

When accounting for spatially varying surface elevations in the ocean and/or basin, results in this chapter show that stable equilibrium configurations can be found. Figs. 4.4 and 4.5 illustrated that, depending on ocean depth and inlet

length, spatial variations in ocean surface elevation alone (radiation damping) can result in a stable double inlet system with two inlets open. Similarly, basin bottom friction alone (Fig. 4.6), depending on basin depth, can lead to stable double inlet systems. Apparently, in these cases the stabilising mechanism, induced by local pressure gradients over the inlets, can overcome the destabilising effect from inlet bottom friction. Roos et al. (2013, submitted) explain the positive effect of spatially varying surface elevations on the stabilising mechanism by considering spatial variations in the basin only. As it turns out, spatial variations in surface elevation in the ocean have the same effect on the stability of double inlet systems.

The effects of Coriolis on the stability of double inlet systems was investigated. The results revealed that without spatial variations in ocean and basin surface elevations Coriolis effects do not lead to stable equilibrium configurations. When spatially varying surface elevations are accounted for, Coriolis effects modify the spatial structure of the surface elevations thereby introducing an asymmetry between the equilibrium inlet cross-sectional areas of both inlets.

4.5 Conclusions

In this chapter, the influence of spatial variations in surface elevation on the cross-sectional stability of double inlet systems is investigated. In particular, the individual contributions of radiation damping in the ocean, basin bottom friction and Coriolis effects as well as basin geometry to this stability are examined. To that extent, a new 2DH hydrodynamic model that explicitly accounts for spatially varying surface elevations in ocean and basin is combined with a stability concept for tidal inlets (Escoffier, 1940). Because the model is computationally efficient by schematising the ocean, inlets and basin as rectangular compartments with uniform depth, it allows the assessment of the equilibrium configuration by using flow diagrams. Below, conclusions are drawn from the main model results.

When, in addition to inlet bottom friction and inertia, radiation damping is considered, stable equilibrium configurations with more than two inlets open are possible. The influence of the radiation damping mechanism is stronger for increasing ratios of inlet and ocean depth and decreasing inlet length. Similar to radiation damping, basin bottom friction alone leads to the existence of stable equilibrium configurations. This mechanism leads to larger stable inlet cross-sectional areas for decreasing basin depth. Coriolis effects do not qualitatively change the stable equilibrium configuration of double inlet systems. However, quantitatively, model results including radiation damping and basin bottom friction show that Coriolis effects trigger an asymmetry in the stable equilibrium cross-sections. The cross-section of the inlet where the tide arrives first is smaller than that of the other inlet. Analysis of the previous three mechanisms suggests that basin bottom friction is the most important one, implying that care should

be taken of assuming a uniformly fluctuating sea surface elevation for the entire back-barrier basin when investigating the stability of double inlet systems.

As well as the mechanisms that trigger spatial variations in surface elevation, the influence of basin geometry is considered. Model results suggest that, qualitatively the basin geometry does not change the presence of stable equilibriums. Quantitatively, a more elongated basin shape in the x-direction, generally corresponds to significantly larger equilibrium values. Specifically, taking a basin surface area of 1200 km^2, equilibrium values can differ up to a factor of approximately 2 depending on basin shape.

Model results further confirm the presence of a competition between a destabilising mechanism, caused by inlet bottom friction, and a stabilising mechanism, caused by the local pressure gradient over the inlets, that explain the (non-)existence of stable double inlet systems with two inlets open. Besides spatial variations in surface elevation in the basin, model results in this chapter also identified that spatial variations in the ocean surface elevation are crucial for the strength of the stabilising mechanism.

Finally, care should be taken in applying the model to natural double inlet systems. This has mainly to do with schematising the basin bathymetry into a mean depth, whereas natural back-barrier basins display a complex network of channels and shoals. To overcome this discrepancy, the basin depth could be used as a tuning parameter by requiring the total energy dissipation during a tidal cycle of the natural basin to be equal to the schematised one.

4.A Solution method for the 2DH model for double inlet systems

This appendix presents the solution method for the 2DH hydrodynamical model for double inlet system. This method is based on the model originally proposed by Roos & Schuttelaars (2011); Roos et al. (2011) for large-scale semi-enclosed rectangular basins with longitudinal and transverse topographic steps.

4.A.1 Wave solutions in a channel of uniform depth

As a first step, the system of equations (4.2)-(4.4) is solved to find the (analytical) wave solutions in infinitely long, semi-enclosed, rotating channels with uniform width B_p and uniform depth H_p, including bottom friction. These equations can be written in terms of the surface level elevation ζ_p, also known as the *Klein-Gordon equation*:

$$[\mathcal{L}^2 + f^2]\frac{\partial \zeta_p}{\partial t} - gH_p\mathcal{L}[\frac{\partial^2 \zeta_p}{\partial x^2} + \frac{\partial^2 \zeta_p}{\partial y^2}] = 0, \tag{4.A.1}$$

with differential operator $\mathcal{L} = \partial/\partial t + r_p/H_p$. A description of the other parameters can be found in the main text of Section 4.2.2. This equation allows for solutions of the form

$$\zeta_p = \Re\left\{\tilde{\zeta}_p(y)e^{i[k_p x - \omega t]}\right\}. \tag{4.A.2}$$

where $\Re$ denotes the real part, ω is the angular frequency, k_p is the wave number and $\tilde{\zeta}_p(y)$ the lateral structure for the surface elevation. Using Eq. (4.A.2), it follows from Eq. (4.A.1) that the wave solutions involve Kelvin modes propagating in the positive and negative x-direction, as well as two families of Poincaré modes, generated at the closed ends. Introducing $\Phi_p = (\zeta_p, u_p, v_p)$, to symbolically represent the system's state in Compartment p, the analytical expressions of these wave solutions in the positive x-direction are:

$$\Phi^{\oplus}_{p,d}(x,y,t) = \begin{pmatrix} \zeta^{\oplus}_{p,d} \\ u^{\oplus}_{p,d} \\ v^{\oplus}_{p,d} \end{pmatrix} = \Re\left\{ Z'_{p,d} \begin{pmatrix} \tilde{\zeta}^{\oplus}_{p,d}(y) \\ \tilde{u}^{\oplus}_{p,d}(y) \\ \tilde{v}^{\oplus}_{p,d}(y) \end{pmatrix} e^{(i[k^{\oplus}_{p,d}x - \omega t])} \right\}, \tag{4.A.3}$$

with amplitude factor $Z'_{p,d}$ (m), wave number $k^{\oplus}_{p,d}$ and lateral structures $\tilde{\zeta}^{\oplus}_{p,d}(y)$, $\tilde{u}^{\oplus}_{p,d}(y)$ and $\tilde{v}^{\oplus}_{p,d}(y)$. For the Kelvin mode ($d = 0$) propagating in the positive x-

direction and defining $\tilde{\Phi}^{\oplus}_{p,0}(y) = (\tilde{\zeta}^{\oplus}_{p,0}(y), \tilde{u}^{\oplus}_{p,0}(y), \tilde{v}^{\oplus}_{p,0}(y))$, the lateral structures read

$$\tilde{\Phi}^{\oplus}_{p,0}(y) = \begin{pmatrix} 1 \\ \varrho_p^{-1}\sqrt{g/H_p} \\ 0 \end{pmatrix} e^{-\frac{y}{\varrho_p L_{R,p}}}, \tag{4.A.4}$$

and the wave number is

$$k^{\oplus}_{p,0} = \varrho_p K_p, \tag{4.A.5}$$

Here, the reference wave number K_p, the Rossby radius of deformation $L_{R,p}$ (both typical for a classical Kelvin wave without bottom friction) and a frictional correction factor ϱ_p are given by

$$K_p = \frac{\omega}{\sqrt{gH_p}}, \qquad L_{R,p} = \frac{\sqrt{gH_p}}{f}, \qquad \varrho_k = \sqrt{1 - \frac{ir_p}{\omega H_p}}, \tag{4.A.6}$$

respectively.

The wave number and lateral structures of the d^{th} Poincaré mode ($d > 0$) propagating (if free) or decaying (if evanescent) in the positive x-direction are given by

$$k^{\oplus}_{p,d} = \sqrt{\varrho_p^2 K_p^2 - \varrho_p^{-2} L_{R,p}^{-2} - \alpha_d^2}, \tag{4.A.7}$$

$$\tilde{\Phi}^{\oplus}_{p,d}(y) = \begin{pmatrix} \cos(\alpha_d y) - \frac{f k^{\oplus}_{p,d}}{\alpha_d \omega \varrho^2} \sin(\alpha_d y) \\ \frac{g k^{\oplus}_{p,d}}{\omega \varrho_p^2} \cos(\alpha_d y) - \frac{f}{\alpha_d \varrho^2 H_p} \sin(\alpha_d y) \\ \frac{i\omega}{\alpha_d \varrho_p^2 H_p} \left[\varrho_p^2 - \frac{k^{\oplus 2}_{p,d}}{K_p^2} \right] \sin(\alpha_d y) \end{pmatrix}, \tag{4.A.8}$$

respectively, with $\alpha_d = d\pi / W_p$.

The modes propagating or decaying in the negative x-direction are defined analogous to Eq. (4.A.3), but now using a superscript $^{\ominus}$ instead of a $^{\oplus}$. By symmetry, the two types of modes $\tilde{\Phi}^{\oplus}_{p,d}$ and $\tilde{\Phi}^{\ominus}_{p,d}$ satisfy the following relationships:

$$\tilde{\Phi}^{\ominus}_{p,d}(y) = \begin{pmatrix} \tilde{\zeta}^{\oplus}_{p,0}(W_p - y) \\ -\tilde{u}^{\oplus}_{p,0}(W_p - y) \\ -\tilde{v}^{\oplus}_{p,0}(W_p - y) \end{pmatrix}, \qquad k^{\ominus}_{p,d} = -k^{\oplus}_{p,d}. \tag{4.A.9}$$

4.A.2 Superposition of wave solutions

The next step is to write the solution in each compartment as a truncated sum of the analytical wave solutions in an infinite channel derived above. To that end, $\Phi_p = (\zeta_p, u_p, v_p)$ is first rewritten as

$$\Phi_p(x,y,t) = \Re\left\{\hat{\Phi}_p(x,y)e^{-i\omega t}\right\}, \tag{4.A.10}$$

where the vector $\hat{\Phi}_p = (\hat{\zeta}_p, \hat{u}_p, \hat{v}_p)$ contains the complex amplitudes of surface elevation, longitudinal and lateral flow velocity, respectively.

The first compartment, 0, is forced at the open boundary by an incoming Kelvin wave. Since, the Poincaré modes bound to the open end ($x = -L_0$) are neglected, the only mode propagating or decaying in the positive x-direction is the incoming Kelvin wave, with coastal amplitude Z_{M2} and initial phase φ (both defined at $x = 0$). At the other interface $x = 0$, Kelvin modes ($d = 0$) and Poincaré modes ($d = 1, 2, \ldots, D$) are generated (i.e., reflected or transmitted). The solution for Compartment 0 can thus be written as

$$\hat{\Phi}_0(x,y) = Z_{M2}e^{i\varphi}\tilde{\Phi}^{\oplus}_{0,0}(y)e^{ik^{\oplus}_{0,0}(x-L_0)} + \sum_{d=0}^{D} a^{\ominus}_{0,d}\tilde{\Phi}^{\ominus}_{0,d}(y)e^{ik^{\ominus}_{0,d}x}, \tag{4.A.11}$$

with truncation number D.

For the other compartments, modes propagating (if free) or decaying (if evanescent) in positive and negative x-directions exist. For the inlet compartments ($p = k = 1, 2$), this results in

$$\hat{\Phi}_k(x,y) = \sum_{d=0}^{D}\left[a^{\oplus}_{k,d}\tilde{\Phi}^{\oplus}_{k,d}(y)e^{ik^{\oplus}_{k,d}x} + a^{\ominus}_{k,d}\tilde{\Phi}^{\ominus}_{k,d}(y)e^{ik^{\ominus}_{k,d}(x-s_1)}\right], \tag{4.A.12}$$

and for the basin compartment ($p = 3$) in

$$\hat{\Phi}_3(x,y) = \sum_{d=0}^{D}\left[a^{\oplus}_{3,d}\tilde{\Phi}^{\oplus}_{3,d}(y)e^{ik^{\oplus}_{3,d}(x-s_1)} + a^{\ominus}_{3,d}\tilde{\Phi}^{\ominus}_{3,d}(y)e^{ik^{\ominus}_{3,d}(x-s_2)}\right], \tag{4.A.13}$$

To make sure that the coefficients $a^{\oplus}_{p,d}$ and $a^{\ominus}_{p,d}$ in Eqs. (4.A.12) and (4.A.13) are of the same order of magnitude as Z_{M2}, the exponential functions in these equations have been normalised to unity at the interfaces $x = 0$,$x = s_1$ and $x = s_2$ respectively.

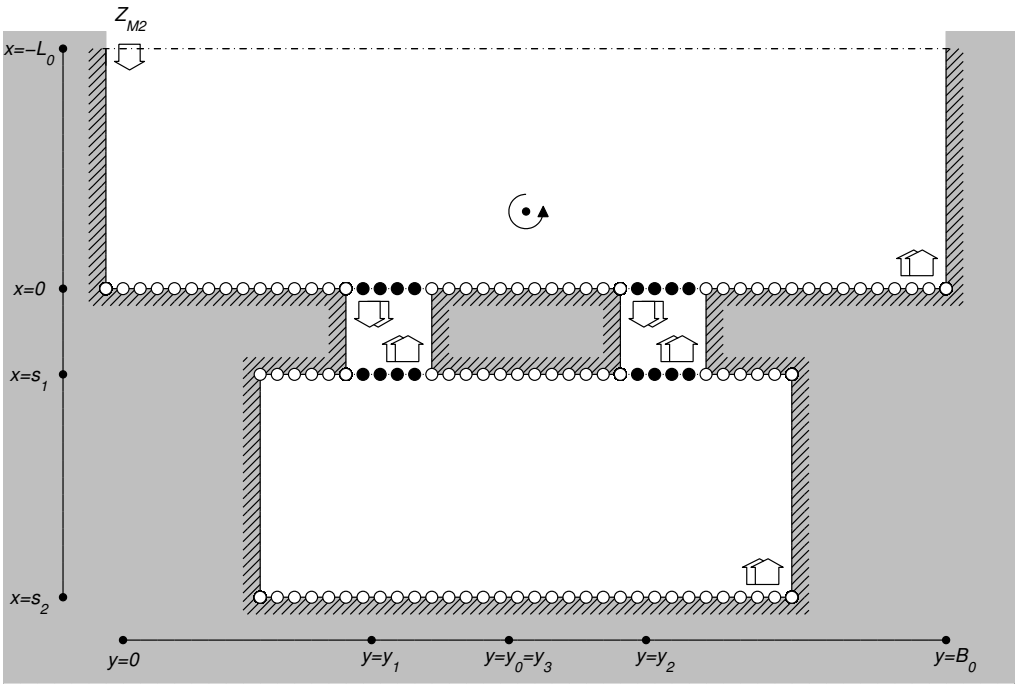

Figure 4.9: Collocation points used to satisfy no-normal flow at the compartments' closed ends (open circles) and continuity of elevation ζ and flux Hu across the topographic steps (solid circles). Combined sets of Kelvin/Poincaré modes are indicated by double arrows, pointing in the direction of propagation/decay; a single arrow represents the incoming Kelvin wave.

4.A.3 Collocation technique

Since each of the individual wave solutions in Eqs. (4.A.11)-(4.A.13) satisfies the no-normal flow condition at the closed boundaries, so do the superpositions $\hat{\Phi}_p$. A collocation technique is used to also satisfy the no-normal flow condition at the closed ends and the matching conditions in Eqs. (4.6) and (4.7) (see Fig. 4.9).

Defining $D+1$ lateral points $y_j = jW_0/D$ for $j = 0, 1, \ldots, D$, the following conditions are required for the closed ends:

$$\hat{u}_0 = 0, \qquad \text{at } (x,y) = (0,y_j) \in \mathcal{B}_{u,0} \tag{4.A.14}$$

$$\hat{u}_3 = 0, \qquad \text{at } \begin{cases} (x,y) = (s_1,y_j) \in \mathcal{B}_{u,k}, \\ (x,y) = (s_2,y_j) \in \mathcal{B}_{u,3}, \end{cases} \tag{4.A.15}$$

for continuity of elevation across the topographic steps:

$$\hat{\zeta}_0 = \hat{\zeta}_k, \qquad \text{at } (x,y) = (0,y_j) \in \mathcal{T}_{0,k}, \tag{4.A.16}$$

$$\hat{\zeta}_k = \hat{\zeta}_3, \qquad \text{at } (x,y) = (s_1,y_j) \in \mathcal{T}_{k,3}, \tag{4.A.17}$$

and for continuity of flux across the topographic steps:

$$H_0\hat{u}_0 = H_k\hat{u}_k, \qquad \text{at } (x,y) = (0,y_j) \in \mathcal{T}_{0,k}, \tag{4.A.18}$$

$$H_k\hat{u}_k = H_3\hat{u}_3, \qquad \text{at } (x,y) = (s_1,y_j) \in \mathcal{T}_{k,3}, \tag{4.A.19}$$

for $k = 1, 2$. This leads to a linear system of equations for the coefficients $a^{\oplus}_{p,d}$ and $a^{\ominus}_{p,d}$, which is solved using standard techniques.

4.A.4 Iterative procedure to calculate friction coefficients

Calculating the bottom friction coefficients r_p in each compartment using Eq. (4.5) requires a typical velocity scale U_p. This quantity is defined as the square root of the squared velocity amplitude, averaged over Compartment p, i.e.

$$U_p^2 = \frac{1}{L_p W_p}\int_0^{L_p}\int_0^{W_p}(|\hat{u}|^2 + |\hat{v}|^2)dxdy. \tag{4.A.20}$$

Subsequently, an iterative procedure is adopted to arrive at the appropriate value for r_p. As a first guess, r_p is obtained from Eq. (4.5) using a typical velocity scale for each compartment. For the ocean compartment, the typical velocity of a classical Kelvin wave without friction is used: $U_0 = Z\sqrt{g/H_0}$ (Pedlosky, 1987). For the inlet compartments, the equilibrium velocity as proposed by Escoffier (1940) of $U_{1,2} = U_{eq} = 1$ m s^{-1} is used. Because the averaged flow velocities in shallow basins are lower than in the inlets, $U_3 = 0$ is taken as initial guess for the basin. Next, these initial guesses are used to obtain a new solution for U_p, U_p^{new}, which is subsequently compared with U_p^{old} and appropriately adjusted according to $U_p^{\text{new}} = U_p^{\text{old}} + \epsilon(U_p^{\text{new}} - U_p^{\text{old}})$. Here, $\epsilon \sim 0.5$ is an under-relaxation factor that significantly accelerates the iteration process. The new (better) U_p-values and thus new r_p values, in turn lead to a new solution and so forth. The iteration ends when the desired accuracy is obtained. Note that the feedback of the solution on the values of the friction coefficients is in fact a non-linear element in an otherwise linear hydrodynamic model.

5 Conclusions and recommendations

This chapter summarizes the main conclusions of this thesis. These conclusions are subdivided in conclusions answering the research questions as formulated in Chapter 1 (Section 5.1), and in overall conclusions (Section 5.2) to address the general aim of this thesis and to place the outcome of this work in a broader perspective. Besides these conclusions, Section 5.3 provides recommendations for improvements of the research methods described in this thesis and for future research areas with respect to barrier coasts and the associated tidal inlet systems.

5.1 Answers to the research questions

Q1: *What is the effect of a topographic high on the cross-sectional stability of double inlet systems? Are sets of stable inlets possible?*

The results of Chapter 2 show that the inclusion of a topographic high can result in sets of stable inlets. Depending on the size of the opening over the topographic high, one, two or no sets of stable inlets are found.

For a relatively small or large opening over the topographic high, the results are in agreement with earlier studies. A small opening reduces the double inlet system to two single inlet systems, yielding one stable inlet for each system (e.g. Escoffier, 1940). For the large opening, the double inlet system behaves as if it has a single, deep basin and no sets of stable inlets are possible (e.g. van de Kreeke, 1990a). In both cases, amplitude and/or phase differences in the tidal forcing seaward of the two inlets do not affect these conclusions.

For intermediate sizes of the opening over the topographic high, either one or two sets of stable inlets can be found. A set of stable inlets in this context refers to a situation where both inlets of the double inlet system are open and stable, i.e. they return to their original equilibrium values after being perturbed. The exact number of these sets of stable inlets depends on amplitude and/or phase differences between the forcing off the two inlets. For relatively small amplitude or phase differences (in the order of centimetres and deciradians, respectively), two sets of stable inlets are found and for larger differences the number of sets of stable inlets reduces to one. For increasing sizes of the opening over the topographic high, the range of amplitude or phase differences where two sets of stable inlets are found increases and vice versa.

Q2: *Can the cross-sectional stability of a double inlet system be determined and explained using a lumped-parameter model including the assumption of a uniformly fluctuating basin level? In particular, what is the role of the different terms in the dynamic equation and the boundary conditions in determining the cross-sectional stability of the inlets?*

In Chapter 3 it is shown that the cross-sectional stability of double inlet systems can be explained (as opposed to predicted) using a lumped-parameter model. A prerequisite to obtain a set of stable inlets is that entrance/exit losses are accounted for in the dynamic equation and that an amplitude difference between the off-shore tides at the inlets is present. Furthermore, the entrance/exit loss term should be considerably larger than the bottom friction term, implying that for longer (from ocean to basin) inlets it is more difficult to find sets of stable inlets. Inertia is the least important term in the dynamic equation and affects the range of the entrance/exit loss coefficient for which sets of stable inlets exist only slightly.

With respect to amplitude differences, for sets of stable inlets to exist an increase in the difference between the amplitudes requires an increase in the entrance/exit loss term and/or an increase in the bottom friction term. Phase differences between the off-shore tides affect the range of amplitude differences where sets of stable inlets exist.

The application of the lumped-parameter model to explain the stability of natural double inlet systems has its limitations. For instance, the presence of stable equilibriums is sensitive to the selection of parameter values, such as inlet length, bottom friction factor and entrance/exit loss coefficient.

Q3: *How do spatial variations in surface elevation and geometry influence the cross-sectional stability of a double inlet system? Can the stabilising and destabilising mechanisms associated with cross-sectional stability be identified?*

As it turns out from Chapter 4, spatial variations in surface elevation in the basin and ocean are crucial to the cross-sectional stability of double inlet systems. They appear to trigger a stabilising mechanism that keeps both inlets open.

Using a two-dimensional, depth-averaged, hydrodynamic model, these spatial variations are mainly induced by radiation damping into the ocean and bottom friction in the basin. In turn, these mechanisms are modified by Coriolis effects.

Radiation damping into the ocean as well as basin bottom friction separately lead to stable equilibrium configurations with two inlets open. The radiation damping mechanism is stronger for increasing ratios of inlet and ocean depth and decreasing inlet length. On the other hand, basin bottom friction leads to larger stable inlet cross-sectional areas for decreasing basin depth.

Coriolis effects do not qualitatively change the stable equilibrium configuration of double inlet system. Quantitatively, however, model results have shown that for increasing latitude the asymmetry between the stable equilibrium cross-sectional area of each inlets becomes larger. The model results suggest that the cross-section of the inlet where the tide arrives first is smaller than the other inlet.

In Chapter 4 it was further shown that basin geometry, i.e. the shape of the basin, does not qualitatively change the presence of stable equilibriums. Quantitatively, a more elongated basin shape in cross-shore direction generally corresponds to significantly larger stable equilibrium cross-sectional areas.

Based on model results, the presence of a competition between a destabilising and a stabilising mechanism that explain the (non-)existence of stable double inlet systems is confirmed (see Roos et al., 2013, submitted). The destabilising mechanism is caused by bottom friction in the inlets, amplifying perturbations from the inlet's equilibrium cross-sectional area, hence moving the cross-sectional area of each inlet further away from its equilibrium value. On the other hand, spatially varying pressure gradients over the inlets trigger a stabilising mechanism that tends to keep the inlets open. Besides spatial variations in surface elevation in the basin (Roos et al., 2013, submitted), model results in Chapter 4 also identified that spatial variations in the ocean surface elevation are able to stabilise the tidal inlets of double inlet systems.

5.2 Overall conclusions

Aim: *To obtain fundamental knowledge of the cross-sectional stability of tidal inlets in double inlet systems, identifying stabilising and destabilising mechanisms.*

The conclusions drawn from Chapters 2-4 and summarized above have clearly increased the fundamental knowledge of the cross-sectional stability of tidal inlets in double inlet systems. According to observations in, for instance, the Dutch Wadden Sea, the Portuguese Ría Formosa and the US east coast, double (or multiple) inlet systems have persisted over a historical time-scale. However, up to now these observations have hardly been supported by model studies. In this thesis, a widely used empirical relationship for inlet stability is combined with (i) a lumped-parameter model (Chapters 2 and 3) and (ii) a two-dimensional, depth-averaged model for the water motion (Chapter 4). The main conclusion is

that accounting for spatial variations in surface elevations in basin and/or ocean either parametrically (Chapter 3) or explicitly (Chapter 2 and 4) is crucial to simulate and explain the long-term evolution of double inlet systems.

Additionally, the competition between a destabilising mechanism (caused by bottom friction in the inlets, tending to close an inlet) and a stabilising one (caused by spatially varying pressure gradients over the inlets, tending to keep inlets open) provides insight as to how double inlet systems may either persist on the long term with two inlets open or may reduce to a single inlet system.

Finally, from a broader perspective the results obtained in this thesis help the design of sustainable and cost-effective coastal zone management strategies. In particular, the fundamental insights, such as the importance of spatial variations in surface elevation in modelling efforts and the identification of a physical mechanism that explains the (in)stability of a double inlet system, facilitate the decision-making on how to deal with the impacts of natural changes and human interventions in double inlet systems.

5.3 Recommendations

Even though this thesis contributes to the fundamental knowledge of the long-term evolution and stability properties of double inlet systems as part of a barrier coast, various questions still remain. To direct future research, some recommendations are made based on the knowledge gained in this thesis.

- **Multiple inlet systems**

  One obvious next step is to study the long-term evolution of multiple (more than two) inlet systems. To that extent, it is particularly important that spatial variations in surface elevation are accounted for. One approach is recently introduced by Roos et al. (2013, submitted) who solve the water motion in ocean, inlets and basin analytically. In their study, the dynamics of the flow in ocean and basin allows for spatial variation in the surface elevation. Because of practical reasons, the approach by Roos et al. (2013, submitted) omits bottom friction in the ocean and Coriolis effects. Another approach is to extend the 2DH model introduced in Chapter 4 from two inlets to more than two inlets connecting ocean and basin.

- **Wave-dominated barrier coasts**

  In this thesis the focus is on the cross-sectional stability of double inlet systems in mixed-energy coasts, where the morphotype displays tide-dominated characteristics (see Section 1.1). However, there are various examples where barrier island coasts have wave-dominated characteristics, or even a combination of the two morphotypes within the same coastal stretch, e.g. the Dutch Wadden Sea coast (Sha, 1989). The effects of wind waves on cross-sectional stability of tidal inlets is not explicitly incorporated in Escoffier's

(1940) stability concept for tidal inlets. One obvious effect of wind waves is the generation of littoral drift, which was assumed constant in this thesis for both inlets. Research is needed to study the effects of wind waves and the associated (spatially varying) littoral drift on the cross-sectional stability of double (or multiple) inlet systems.

- **Natural phenomena of barrier coasts**

  The research approach adopted in this thesis intentionally ignored natural phenomena associated with barrier coasts, such as complex channel-shoal interactions, inlet migration and more complex inlet/basin geometries. Even though it is believed that the general conclusions arrived at in this thesis will be sustained, more research is necessary to study the effects of these natural phenomena on the cross-sectional stability of (multiple) tidal inlet systems.

References

Abramowitz, M. & Stegun, I.A. (1972) Handbook of Mathematical Functions with Formulas, Graphs, and Mathematical Tables. No. 55 in Applied Mathematics Series, Dover Publications, New York, 10th edn., 1046 pp.

Andrade, C.F. (1990) Estudo da susceptibilidade ao galgamento da Ría Formosa, Algarve–Portugal. *Geolis* **IV**(1-2): 69–76.

Beets, D.J. & van der Spek, A.J.F. (2000) The Holocene evolution of the barrier and the back-barrier basins of Belgium and the Netherlands as a function of late Weichselian morphology, relative sea-level rise and sediment supply. *Netherlands Journal of Geosciences* **79**(1): 3–16.

Bettencourt, P. (1988) Apports de l'étude sedimentologique a la comprehension de l'evolution d'un system d'iles barriéres (Algarve, Sud Portugal). *Bulletin de l'Institut de Geologie du Bassin d'Aquitaine* **44**: 81–96.

Boon, J.D. & Byrne, R.J. (1981) On basin hyposmetry and the morphodynamic response of coastal inlet systems. *Marine Geology* **40**(1-2): 27–48, doi:10.1016/0025-3227%2881%2990041-4.

Boyd, J.P. (2001) Chebyshev and Fourier spectral methods. Dover Publications, New York, 2nd edn., 665 pp.

Brouwer, R.L., Schuttelaars, H.M., & Roos, P.C. (2012) Influence of basin geometry on equilibrium and stability of double inlet systems. In: Jubilee Conference Proceedings NCK-days 2012: Crossing borders in coastal research, edited by W.M. Kranenburg, E.M. Horstman, & K.M. Wijnberg, pp. 85–89, University of Twente, 13-16 March 2012, Enschede, The Netherlands, doi:10.3990/2.175.

Brown, E.I. (1928) Inlets on sandy coasts. In: Proceedings of the American Society of Civil Engineers, vol. 54, pp. 505–553.

Bruun, P. & Gerritsen, F. (1960) Stability of coastal inlets. North Holland Publishing Co., The Netherlands.

Bruun, P., Mehta, A.J., & Johnsson, I.G. (1978) Stability of tidal inlets: Theory and engineering. Elsevier Scientific Publishing Co., The Netherlands, 510 pp.

Buchwald, V.T. (1971) The diffraction of tides by a narrow channel. *Journal of Fluid Mechanics* **46**(3): 501–511, doi:10.1017/S0022112071000661.

Buijsman, M.C. & Ridderinkhof, H. (2007) Long-term ferry-ADCP observations of tidal currents in the Marsdiep Inlet. *Journal of Sea Research* **57**(4): 237–256, doi:10.1016/j.seares.2006.11.004.

Cayocca, F. (2001) Long-term morphological modeling of a tidal inlet: the Arcachon Basin, France. *Coastal Engineering* **42**(2): 115–142, doi:10.1016/S0378-3839(00)00053-3.

Dastgheib, A., Roelvink, J.A., & Wang, Z.B. (2008) Long-term process-based morphological modeling of the Marsdiep Tidal Basin. *Marine Geology* **256**(1-4): 90–100, doi:10.1016/j.margeo.2008.10.003.

Davies, J.L. (1964) A morphogenic approach to world shore-lines. *Zeitschrift für Geomorphologie* **8**: 27–142.

Davis Jr., R.A. (1997) Regional coastal morphodynamics along the United States Gulf of Mexico. *Journal of Coastal Research* **13**: 594–604.

Davis Jr., R.A. & Hayes, M.O. (1984) What is a wave-dominated coast? *Marine Geology* **60**: 313–329, doi:10.1016/S0070-4571(08)70152-3.

Dhooge, A., Govaerts, W., & Kuznetsov, Y.A. (2003) MATCONT: A MATLAB package for numerical bifurcation analysis of ODE's. *ACM Transactions on Mathematical Software* **29**: 141–164, doi:10.1145/779359.779362.

Dias, J.M.A. & Sousa, M.C. (2009) Numerical modeling of Ría Formosa tidal dynamics. *Journal of Coastal Research* **SI 56**: 1345–1349.

Dias, J.M.A., Sousa, M.C., Bertin, X., Fortunato, A.B., & Oliveira, A. (2009) Numerical modeling of the impact of the Ancão Inlet relocation (Ría Formosa, Portugal). *Environmental Modelling & Software* **24**(6): 711–725, doi:10.1016/j.envsoft.2008.10.017.

DiLorenzo, J.L. (1988) The overtide and filtering response of small inlet/bay systems. In: Hydrodynamics and Sediment Dynamics of Tidal Inlets, edited by D.G. Aubrey & L. Weishar, vol. 29 of *Lecture Notes on Coastal and Estuarine Studies*, chap. 2, pp. 24–53, AGU, Washington, DC, doi:10.1029/LN029p0024.

Dronkers, J. (1986) Tidal asymmetry and estuarine morphology. *Netherlands Journal of Sea Research* **20**(2-3): 117–131, doi:10.1016/0077-7579(86)90036-0.

Ehlers, J. (1988) The morphodynamics of the Wadden Sea. Balkema, Rotterdam, viii+397 pp.

Elias, E.P.L. (2006) Morphodynamics of Texel Inlet. Ph.D. thesis, Delft University of Technology.

Elias, E.P.L., Stive, M.J.F., Bonekamp, H., & Cleveringa, J. (2003) Tidal inlet dynamics in response to human intervention. *Coastal Engineering Journal* **45**(04): 629–658, doi:10.1142/S0578563403000932.

Escoffier, F.F. (1940) The stability of tidal inlets. *Shore and Beach* **8**(4): 111–114.

Escoffier, F.F. (1977) Hydraulics and stability of tidal inlets. GITI Report 13, U.S. Army Coastal Engineering Research Center, Vicksburg, MS.

Eysink, W.D. (1990) Morphologic response of tidal basins to changes. In: Proceedings 22nd International Conference on Coastal Engineering, vol. 2, pp. 1948–1961.

Friedrichs, C.T., Armbrust, B.A., & de Swart, H.E. (1998) Hydrodynamic and equilibrium sediment dynamics of shallow, funnel-shaped tidal estuaries. In: Physics of Estuaries and Coastal Seas, edited by J. Dronkers & M. Scheffers, pp. 315–328, Balkema, Rotterdam.

Friedrichs, C.T. & Aubrey, D.G. (1988) Non-linear tidal distortion in shallow well-mixed estuaries: a synthesis. *Estuarine, Coastal and Shelf Science* **27**(5): 521–545, doi:10.1016/0272-7714(88)90082-0.

Garrett, C. (1975) Tides in gulfs. *Deep-Sea Research* **22**(1): 23–35, doi:10.1016/0011-7471(75)90015-7.

Glaeser, J.D. (1978) Global distribution of barrier islands in terms of tectonic setting. *Journal of Geology* **86**(3): 283–297.

Godin, G. (1965) The M2 tide in the Labrador Sea, Davis Strait and Baffin Bay. *Deep Sea Research and Oceanographic Abstracts* **12**(4): 469–477, doi:10.1016/0011-7471(65)90401-8.

Groen, P. (1967) On the residual transport of suspended matter by an alternating tidal current. *Netherlands Journal of Sea Research* **3**(4): 564–574, doi:10.1016/0077-7579(67)90004-X.

Grunnet, N.M. & Hoekstra, P. (2004) Alongshore variability of the multiple barred coast of Terschelling, The Netherlands. *Marine Geology* **203**(12): 23–41, doi:10.1016/S0025-3227(03)00336-0.

Hayes, M.O. (1975) Morphology of sand accumulations in estuaries. In: Estuarine Research, edited by L.E. Cronin, vol. 2, pp. 3–22, Academic Press, New York.

Hayes, M.O. (1979) Barrier island morphology as a function of tidal and wave regime. In: Barrier Islands, edited by S.P. Leatherman, chap. 1, Springer-Verlag, New York.

Heath, R.A. (1976) Broad classification of New Zealand inlets with emphasis on residence times. *New Zealand Journal of Marine and Freshwater Research* **10**(3): 429–444, doi:10.1080/00288330.1976.9515628.

Herman, A. (2007) Numerical modelling of water transport processes in partially-connected tidal basins. *Coastal Engineering* **54**(4): 297–320, doi:10.1016/j.coastaleng.2006.10.003.

Hibma, A., Schuttelaars, H.M., & Wang, Z.B. (2003) Comparison of longitudinal equilibrium profiles of estuaries in idealized and process-based models. *Ocean*

Dynamics **53**(3): 252–269, doi:10.1007/s10236-003-0046-7.

Hicks, M.D., Hume, T.M., Swales, A., & Green, M.O. (1999) Magnitudes, spacial extent, time scales and causes of shoreline change adjacent to an ebb tidal delta, Katikati Inlet, New Zealand. *Journal of Coastal Research* **15**(1): 220–240.

Hume, T.M. & Herdendorf, C.E. (1988) The "Furkert-Heath" relationship for tidal inlet stability reviewed. *New Zealand Journal of Marine and Freshwater Research* **22**(1): 129–134, doi:10.1080/00288330.1988.9516284.

Jain, M., Mehta, A.J., van de Kreeke, J., & Dombrowsky, M.R. (2004) Observations on the stability of St. Andrews Bay in Florida. *Journal of Coastal Research* **20**(3): 913–919.

Jarrett, J.T. (1976) Tidal prism-inlet area relationships. GITI Report 3, U.S. Army Coastal Engineering Research Center, Vicksburg, MS.

Keulegan, G.H. (1951) Third progress report on tidal flow in entrances: water level fluctuations of basins in communication with seas. Report no. 1146, National Bureau of Standards, Washington, D.C.

Kraus, N.C. (1998) Inlet cross-sectional area calculated by process-based model. In: International Conference on Coastal Engineering, vol. 3, pp. 3265–3278.

van de Kreeke, J. (1967) Water-level fluctuations and flow in tidal inlets. *Journal of the Waterways, Harbor and Coastal Engineering Division, ASCE* **93**(WW4): 97–106.

van de Kreeke, J. (1985) Stability of tidal inlets–Pass Cavallo, Texas. *Estuarine, Coastal and Shelf Science* **21**(1): 33–43, doi:10.1016/0272-7714(85)90004-6.

van de Kreeke, J. (1988) Hydrodynamics of tidal inlets. In: Hydrodynamics and Sediment Dynamics of Tidal Inlets, edited by D.G. Aubrey & L. Weishar, vol. 29 of *Lecture Notes on Coastal and Estuarine Studies*, chap. 1, pp. 1–23, AGU, Washington, DC, doi:10.1029/LN029p0001.

van de Kreeke, J. (1990a) Can multiple tidal inlets be stable? *Estuarine, Coastal and Shelf Science* **30**(3): 261–273, doi:10.1016/0272-7714(90)90051-R.

van de Kreeke, J. (1990b) Stability analysis of a two-inlet bay system. *Coastal Engineering* **14**(6): 481–497, doi:10.1016/0378-3839(90)90031-Q.

van de Kreeke, J. (1992) Stability of tidal inlets; Escoffier's analysis. *Shore and Beach* **60**(1): 9–12.

van de Kreeke, J. (1998) Adaptation of the Frisian Inlet to a reduction in basin area with special reference to the cross-sectional area. In: Physics of Estuarine and Coastal Seas: Proceedings of an international conference, The Hague, 9-12 September 1996, edited by J. Dronkers & M.B.A.M. Scheffers, pp. 355–362.

van de Kreeke, J. (2004) Equilibrium and cross-sectional stability of tidal inlets: application to the Frisian Inlet before and after basin reduction. *Coastal Engineering* **51**(5-6): 337–350, doi:10.1016/j.coastaleng.2004.05.002.

LeConte, L.J. (1905) Discussion of "Notes on the improvement of river and har-

bour outlets in the United States" by D.A. Watts. *Transactions of the American Society of Civil Engineers* **LV**(2): 306–308.

Lorentz, H.A. (1926) Verslag Staatscommissie Zuiderzee 1918-1926. Tech. rep., Den Haag.

Louters, T. & Gerritsen, F. (1994) The riddle of the sands; a tidal system's answer to a rising sea level. Report RIKZ-94.040 pp. 69, National Institute for Coastal and Marine Management.

Maas, L.R.M. (1997) On the nonlinear Helmholtz response of almost-enclosed tidal basins with sloping bottoms. *Journal of Fluid Mechanics* **349**: 361–380, doi: 10.1017/S0022112097006824.

Mehta, A.J. & Özsoy, E. (1978) Inlet hydraulics. In: Stability of Tidal Inlets: Theory and Engineering, edited by P. Bruun, pp. 83–161, Elsevier Scientific Publishing Co., Amsterdam, The Netherlands.

Miles, J.W. (1948) The coupling of a cylindrical tube to a half-infinite space. *The Journal of the Acoustical Society of America* **20**(5): 652–664, doi:10.1121/1.1906423.

Murray, A.B. (2003) Contrasting the goals, strategies, and predictions associated with simplified numerical models and detailed simulations. In: Prediction in Geomorphology, edited by P.R. Wilcock & R.M. Iverson, vol. 135 of *Geophysical Monograph Series*, pp. 151–165, AGU, Washington D.C., doi:10.1029/GM135.

Nahon, A., Bertin, X., Fortunato, A.B., & Oliveira, A. (2012) Process-based 2DH morphodynamic modeling of tidal inlets: A comparison with empirical classifications and theories. *Marine Geology* **291–294**: 1–11, doi:10.1016/j.margeo.2011.10.001.

National Park Service (2012) Post-Hurricane Sandy: Old Inlet breach on Fire Islands. URL `http://www.nps.gov/fiis/naturescience/post-hurricane-sandy-breaches.htm`.

O'Brien, M.P. (1931) Estuary tidal prism related to entrance areas. *Civil Engineering* **1**(8): 738–739.

O'Brien, M.P. (1969) Equilibrium flow areas of inlets on sandy coasts. *Journal of the Waterways and Harbors Division* **95**(WW1): 43–52.

O'Brien, M.P. & Clark, R.R. (1974) Hydraulic constants of tidal entrances. In: 14th Coastal Engineering Conference, vol. II, pp. 1546–1565, ASCE, Copenhagen, Denmark.

O'Brien, M.P. & Dean, R.G. (1972) Hydraulics and sedimentary stability of coastal inlets. In: 13th International Conference on Coastal Engineering, 10-14 July, Vancouver, Canada, pp. 761–780, ASCE.

Oost, A.P. (1995) Dynamics and sedimentary development of the Dutch Wadden Sea with emphasis on the Frisian inlets. Geologica Ultraiectina, Mededelingen van de Faculteit Aardwetenschappen no. 126, Utrecht University.

Oost, A.P. & de Boer, P.L. (1994) Sedimentology and development of barrier islands, ebb-tidal deltas, tidal inlets and backbarrier areas of the Dutch Wadden Sea. *Senckenbergiana Maritima* **24**(1/6): 65–115.

Pacheco, A., Ferreira, Ó., & Williams, J.J. (2011a) Long-term morphological impacts of the opening of a new inlet on a multiple inlet system. *Earth Surface Processes and Landforms* **36**(13): 1726–1735, doi:10.1002/esp.2193.

Pacheco, A., Ferreira, Ó., Williams, J.J., Garel, E., Vila-Concejo, A., & Dias, J. (2010) Hydrodynamics and equilibrium of a multiple-inlet system. *Marine Geology* **274**(1-4): 32–42, doi:10.1016/j.margeo.2010.03.003.

Pacheco, A., Williams, J.J., Ferreira, Ó., Garel, E., & Reynolds, S. (2011b) Applicability of sediment transport models to evaluate medium term evolution of tidal inlet systems. *Estuarine, Coastal and Shelf Science* **95**(1): 119–134, doi:10.1016/j.ecss.2011.08.027.

Pedlosky, J. (1987) Geophysical fluid dynamics. Springer-Verlag, New York, 728 pp.

Pingree, R.D. & Griffiths, D.K. (1979) Sand transport paths around the British Isles resulting from M2 and M4-tidal interactions. *Journal of the Marine Biological Association of the United Kingdom* **59**(02): 497–513, doi:10.1017/S0025315400042806.

Postma, H. (1954) Hydrography of the Dutch Wadden Sea. *Archives Neérlandaises de Zoologie* **10**: 405–511.

Pritchard, D. & Hogg, A.J. (2003) Cross-shore sediment transport and the equilibrium morphology of mudflats under tidal currents. *Journal of Geophysical Research* **108**: 15, doi:10.1029/2002JC001570.

Ridderinkhof, H. (1988) Tidal and residual flows in the western Dutch Wadden Sea II: An analytical model to study the constant flow between connected tidal basins. *Netherlands Journal of Sea Research* **22**(3): 185–198, doi:10.1016/0077-7579(88)90022-1.

van Rijn, L. (1993) Principles of sediment transport in rivers, estuaries and coastal seas. Aqua Publications.

Roos, P.C. & Schuttelaars, H.M. (2011) Influence of topography on tide propagation and amplification in semi-enclosed basins. *Ocean Dynamics* **61**(1): 21–38, doi:10.1007/s10236-010-0340-0.

Roos, P.C., Schuttelaars, H.M., & Brouwer, R.L. (2013) Observations on barrier island length explained using an exploratory morphodynamic model. *Geophysical Research Letters* (accepted manuscript).

Roos, P.C., Velema, J.J., Hulscher, S.J.M.H., & Stolk, A. (2011) An idealized model of tidal dynamics in the North Sea: resonance properties and response to large-scale changes. *Ocean Dynamics* **61**(12): 2019–2035, doi:10.1007/

s10236-011-0456-x.

Roskam, A.P. (1988) Golfklimaten voor de Nederlands kust (in Dutch). Tech. Rep. GWAO-88.046, Rijkswaterstaat RIKZ, The Hague.

Salles, P. (2001) Hydrodynamic controls on multiple tidal inlet persistence. Ph.D. thesis, Massachusetts Institute of Technology and Woods Hole Oceanographic Institution.

Salles, P., Voulgaris, G., & Aubrey, D.G. (2005) Contribution of nonlinear mechanisms in the persistence of multiple tidal inlet systems. *Estuarine, Coastal and Shelf Science* **65**(3): 475–491, doi:10.1016/j.ecss.2005.06.018.

Seabergh, W.C. (2002) Hydrodynamics of tidal inlets. In: Coastal Engineering Manual, 1110-2-1100, chap. II-6, U.S. Army Corps of Engineers, Washington, DC.

Sha, L.P. (1989) Variation in ebb-delta morphologies along the West and East Frisian Islands, The Netherlands and Germany. *Marine Geology* **89**(1-2): 11–28, doi:10.1016/0025-3227(89)90025-X.

Spanhoff, R., Biegel, E., van de Graaff, J., & Hoekstra, P. (1997) Shoreface nourishments at Terschelling, the Netherlands: Feeder berm or breaker berm? In: Proceedings of Coastal Dynamics '97, pp. 863–872, ASCE, New York.

van Straaten, L. & Kuenen, P. (1957) Accumulation of fine grained sediments in the Dutch Wadden Sea. *Netherlands Journal of Geosciences* **19**: 329–354.

Suprijo, T. & Mano, A. (2004) Dimensionless parameters to describe topographical equilibrium of coastal inlets. vol. 3, pp. 2531–2543.

de Swart, H.E. & Volp, N.D. (2012) Effects of hypsometry on the morphodynamic stability of single and multiple tidal inlet systems. *Journal of Sea Research* **74**: 35–44, doi:10.1016/j.seares.2012.05.008.

de Swart, H.E. & Zimmerman, J.T.F. (2009) Morphodynamics of tidal inlet systems. *Annual Review of Fluid Mechanics* **41**: 203–229, doi:10.1146/annurev.fluid.010908.165159.

Tambroni, N. & Seminara, G. (2006) Are inlets responsible for the morphological degradation of Venice Lagoon? *Journal of Geophysical Research* **111**(F03013): 1–19, doi:doi:10.1029/2005JF000334.

Tànczos, I.C., Aarninkhof, S.G.J., & van de Weck, A.W. (2001) Ruimte voor de zandrivier (in Dutch). Tech. Rep. Z3200, WL|Delft Hydraulics.

Taylor, G.I. (1920) Tidal oscillations in gulfs and rectangular basins. *Proceedings of the London Mathematical Society* **s2-20**(1): 148–181, doi:10.1112/plms/s2-20.1.148.

Tung, T.T., van de Kreeke, J., Stive, M.J.F., & Walstra, D.J.R. (2012) Cross-sectional stability of tidal inlets: A comparison between numerical and empirical approaches. *Coastal Engineering* **60**: 21–29, doi:10.1016/j.coastaleng.2011.08.005.

Vennell, R. (2006) ADCP measurements of momentum balance and dynamic topography in a constricted tidal channel. *Journal of Physical Oceanography* **36**(2): 177–188, doi:10.1175/JPO2836.1.

Vila-Concejo, A., Matias, A., Pacheco, A., Ferreira, Ó., & Dias, J.M.A. (2006) Quantification of inlet-related hazards in barrier island systems. An example from the Ría Formosa (Portugal). *Continental Shelf Research* **26**(9): 1045–1060, doi:10.1016/j.csr.2005.12.014.

Vos, P.C., Bazelmans, J., Weerts, H.J.T., & van der Meulen, M.J. (2011) Atlas van Nederland in het Holoceen (in Dutch). Uitgeverij Bert Bakker.

de Vriend, H.J. (1996) Mathematical modelling of meso-tidal barrier island coasts. Part I: Empirical and semi-empirical models. In: Advances in coastal and ocean engineering, edited by P.L.F. Liu, vol. 2, chap. 3, pp. 115–149, World Scientific Publishing Co., Singapore, doi:10.1142/9789812797575_0003.

de Vriend, H.J. & Ribberink, J.S. (1996) Mathematical modelling of meso-tidal barrier island coasts. Part II: Process-based simulation models. In: Advances in coastal and ocean engineering, edited by P.F. Liu, vol. 2, chap. 4, pp. 151–197, World Scientific Publishing Co., Singapore, doi:10.1142/9789812797575_0004.

Walton Jr., T.L. (2004) Escoffier Curves and inlet stability. *Journal of Waterway, Port, Coastal, and Ocean Engineering* **130**(1): 54–57, doi:10.1061/(ASCE)0733-950X(2004)130:1(54).

Walton Jr., T.L. & Escoffier, F.F. (1981) Linearized solution to inlet equation with inertia. *Journal of the Waterway, Port, Coastal and Ocean Division, ASCE* **107**(WW3): 191–195.

Wang, P. & Beck, T.M. (2012) Morphodynamics of an anthropogenically altered dual-inlet system: John's Pass and Blind Pass, west-central Florida, USA. *Marine Geology* **291–294**: 162–175, doi:10.1016/j.margeo.2011.06.001.

Wang, Z.B., Louters, T., & de Vriend, H.J. (1995) Morphodynamic modelling for a tidal inlet in the Wadden Sea. *Marine Geology* **126**(1–4): 189–300, doi:10.1016/0025-3227(95)00083-B.

Wang, Z.B., de Vriend, H.J., & Louters, T. (1991) A morphodynamic model for a tidal inlet. In: Computer Modelling in Ocean Engineering '91 - Proceedings of the second International Conference, edited by A.S. Arcilla, M. Pastor, O.C. Zienkiewicz, & B.A. Schrefler, pp. 235–245, Balkema, Rotterdam.

Wijnberg, K.M. (1995) Morphologic behaviour of a barred coast over a period of decades. Netherlands Geographical Studies 195, Utrecht University, Utrecht, The Netherlands.

Zimmerman, J.T.F. (1976) Mixing and flushing of tidal embayments in the western Dutch Wadden Sea part I: Distribution of salinity and calculation of mixing time scales. *Netherlands Journal of Sea Research* **10**(2): 149–191, doi:10.1016/0077-7579(76)90013-2.

Zimmerman, J.T.F. (1982) On the Lorentz linearization of a quadratically damped forced oscillator. *Physics Letters A* **89A**(3): 123–124, doi:10.1016/0375-9601(82)90871-4.

List of Symbols

Roman Symbols

A	cross-sectional area of an inlet	m^2	(Ch. 1-4)
A_{cr}	cross-sectional area where the closure curve has its maximum	m^2	(Ch. 1)
a	amplitude coefficients in collocation technique	-	(Ch. 4)
B	basin surface area	m^2	(Ch. 1-3)
C	empirical proportionality coefficient in AP-relationship	m^{-1}	(Ch. 1, 2)
C_{bf}	bottom friction bulk coefficient	m s	(Ch. 1)
C_{pg}	pressure gradient bulk coefficient	$s\ m^{-2}$	(Ch. 1)
c	bulk coefficient	$s^2\ m^{-1}$	(Ch. 3)
D	truncation number in collocation technique	-	(Ch. 4)
d	wave mode	-	(Ch. 4)
F	bottom friction factor	-	(Ch. 1-4)
F'	modified bottom friction factor	-	(Ch. 1)
f	Coriolis parameter	$rad^2\ s^{-1}$	(Ch. 4)
g	gravitational acceleration	$m\ s^{-2}$	(Ch. 1-4)
H	water depth	m	(Ch. 4)
j	number of lateral point in collocation technique	-	(Ch. 4)
K	reference wave number	m^{-1}	(Ch. 4)
k	wave number	m^{-1}	(Ch. 4)
L	inlet/compartment length	m	(Ch. 1-4)
L_R	Rossby radius of deformation	m	(Ch. 4)
M	average annual littoral drift imported into an inlet	$m^3\ yr^{-1}$	(Ch. 1-4)
m	entrance/exit loss coefficient	-	(Ch. 3)
n	power constant in sediment transport formulation	-	(Ch. 1-4)
P	tidal prism	m^3	(Ch. 2)
q	empirical proportionality power-coefficient in AP-relationship	-	(Ch. 1, 2)
R	hydraulic radius	m	(Ch. 1-3)
r	bottom friction coefficient in a compartment	$m\ s^{-1}$	(Ch. 4)

s	dimensional constant in equation for sand import into and export out of a tidal basin	m^2	(Ch. 2)
T	tidal period	s	(Ch. 1-4)
TR	sediment transport (export) out of an inlet	$m^3\ s^{-1}$	(Ch. 2)
t	time	s	(Ch. 1-4)
U	amplitude of tidal velocity in inlet/compartment	$m\ s^{-1}$	(Ch. 1-4)
U_{eq}	equilibrium velocity	$m\ s^{-1}$	(Ch. 1-4)
u	cross-sectional averaged inlet velocity	$m\ s^{-1}$	(Ch. 1-3)
$u(x,y)$	depth-averaged flow velocity component in positive x-direction	$m\ s^{-1}$	(Ch. 4)
$v(x,y)$	depth-averaged flow velocity component in positive y-direction	$m\ s^{-1}$	(Ch. 4)
W	compartment width	m	(Ch. 4)
W_{th}	cross-basin width of the topographic high	m	(Ch. 2)
Z	amplitude of the surface elevation in/off inlet or in compartment	m	(Ch. 1-4)
Z'	amplitude factor	m	(Ch. 4)
Z_{M2}	typical amplitude of incoming Kelvin wave	m	(Ch. 4)

Greek symbols

α	bulk parameter	m^{-1}	(Ch. 4)
β	bulk coefficient	$m\ s^{-1}$	(Ch. 2)
Γ	bulk coefficient	$m\ s^{-2}$	(Ch. 2)
γ	inlet shape factor	-	(Ch. 1-4)
$\Delta\theta$	phase difference between the forcing off both inlets	rad	(Ch. 2, 3)
ΔZ	amplitude difference between the forcing off both inlets	m	(Ch. 2, 3)
ϵ	under-relaxation factor	-	(Ch. 2)
ζ	surface elevation	m	(Ch. 1-4)
η	bulk coefficient	$m\ s^{-1}$	(Ch. 2)
θ	phase of the sea surface elevation off the inlet	rad	(Ch. 2,3)
ϑ	central latitude of double inlet system	°N	(Ch. 4)
κ	bulk coefficient eigenvalue problem	$m^{-4}\ s^{-1}$	(Ch. 3)
λ	eigenvalue	-	(Ch. 3)
μ	bulk coefficient	$m\ s^3$	(Ch. 3)
ξ	bulk coefficient eigenvalue problem	m^4	(Ch. 3)
ϱ	frictional correction factor	-	(Ch. 4)
σ	bulk coefficient eigenvalue problem	m^4	(Ch. 3)
τ	bulk coefficient	$m\ s^{-1}$	(Ch. 2)
Φ	symbolic representation of compartment's state w.r.t. u, v and ζ	-	(Ch. 4)
φ	phase of the basin surface elevation	rad	(Ch. 2, 3)
ψ	phase of the inlet velocity	rad	(Ch. 2, 3)
ω	radial frequency	s^{-1}	(Ch. 1-4)

ω_0	Helmholtz frequency	s^{-1}	(Ch. 1)
Ω	angular frequency of the Earth's rotation	rad s^{-1}	(Ch. 4)

General sub- and superscripts

x_k	value of x in/off Inlet k ($k = 1, 2$) or topographic high ($k = 3$)	(Ch. 2-4)
x_b	value of x in tidal basin	(Ch. 1-3)
x_{b_k}	value of x in sub-basin b_k	(Ch. 1-3)
x_0	value of x in the ocean	(Ch. 1-3)
x_p	value of x in Compartment p ($p = 0, \ldots, 3$)	(Ch. 4)
$x_{\min}$	minimum value of x	(Ch. 3)
$x_{\max}$	maximum value of x	(Ch. 1, 3)
x_{char}	characteristic value of x	(Ch. 4)
$x_{c,k}$	real part of x in Inlet k	(Ch. 2)
$x_{s,k}$	imaginary part of x in Inlet k	(Ch. 2)
x^{eq}	equilibrium value of x	(Ch. 2, 3)
$x^{\ominus}$	value of x in negative x-direction	(Ch. 4)
$x^{\oplus}$	value of x in positive x-direction	(Ch. 4)

Mathematics

$\lvert x \rvert$	absolute value of x	(Ch. 1-4)
Δx	small perturbation of x	(Ch. 2, 3)
$\hat{x}$	complex amplitude of x	(Ch. 1-4)
$\tilde{x}$	lateral structure of x in collocation technique	(Ch. 4)
$\underline{x}$	vector notation of $x_{1,\ldots,n}$	(Ch. 2)
$\vec{e}$	unit vector	(Ch. 3)
$\mathcal{B}$	closed boundary	(Ch. 4)
$\mathcal{L}$	differential operator	(Ch. 4)
$\mathcal{O}$	order of magnitude	(Ch. 3)
$\mathcal{T}$	boundary at topographic step	(Ch. 4)
$\Re$	real part	(Ch. 1-4)
$\Im$	imaginary part	(Ch. 2)
i	imaginary number	(Ch. 1-4)

Abbreviations

2D	two-dimensional	(Ch. 3)
2DH	two-dimensional, depth-averaged	(Ch. 1, 4)
AP-relationship	empirical relationship between inlet's cross-sectional area and tidal prism	(Ch. 1, 2)
LP	limit point	(Ch. 2, 3)
L-P	lumped-parameter	(Ch. 1-4)
MSL	mean sea level	(Ch. 1)

About the author

Ronald Brouwer was born in Hellevoetsluis, the Netherlands, April 27th 1979. He graduated from secondary school, Baudartius College in Zutphen, in 1997. Straight after graduation, he started studying Civil Engineering at Delft University of Technology. After receiving his B.Sc. degree in 2001, he continued his M.Sc. in the area of Hydraulic/Coastal Engineering, which resulted in his final M.Sc. thesis, entitled *"Equilibrium and stability of a double inlet system"*, and graduation in 2006.

In 2006, he acquired a Ph.D. position in the Section of Hydraulic Engineering at Delft University of Technology, extending his M.Sc. thesis on the long-term evolution and stability of double inlet systems as part of a barrier coast. This work resulted in the present thesis.

Since 1998, alongside his academic education and PhD position, Ronald played field hockey on the highest international level. He participated in, amongst others, two Olympic Games (silver in 2004, Athens and 4th place in 2008, Beijing) and three World Cups.

As of February 1st 2013, Ronald started as a scientific researcher in the project Nearshore Monitoring and Modelling: Inter-scale Coastal Behaviour (NEMO). This project uses innovative field campaigns to obtain unprecedented insights into the complex processes along the Dutch coast.